



ISSN 1605-2730

MATERIALS PHYSICS AND MECHANICS

Vol. 34, No. 1, 2017

MATERIALS PHYSICS AND MECHANICS

Principal Editors:

Dmitrii Indeitsev
*Institute of Problems of Mechanical Engineering
of the Russian Academy of Science (RAS), Russia*

Andrei Rudskoi
Peter the Great St.Petersburg Polytechnic University, Russia

Founder and Honorary Editor: Ilya Ovid'ko (1961-2017)

*Institute of Problems of Mechanical Engineering
of the Russian Academy of Sciences (RAS), Russia*

Staff Editors:

Anna Kolesnikova
*Institute of Problems of Mechanical Engineering
of the Russian Academy of Sciences (RAS), Russia*

Alexander Nemov
Peter the Great St.Petersburg Polytechnic University, Russia

Editorial Board:

E.C. Aifantis
Aristotle University of Thessaloniki, Greece

K.E. Aifantis
University of Florida, USA

U. Balachandran
Argonne National Laboratory, USA

A. Bellosi
Research Institute for Ceramics Technology, Italy

A.K. Belyaev
Institute of Problems of Mechanical Engineering (RAS), Russia

S.V. Bobylev
Institute of Problems of Mechanical Engineering (RAS), Russia

A.I. Borovkov
Peter the Great St.Petersburg Polytechnic University, Russia

G.-M. Chow
National University of Singapore, Singapore

Yu. Estrin
Monash University, Australia

A.B. Freidin
Institute of Problems of Mechanical Engineering (RAS), Russia

Y. Gogotsi
Drexel University, USA

I.G. Goryacheva
Institute of Problems of Mechanics (RAS), Russia

D. Hui
University of New Orleans, USA

G. Kiriakidis
IESL/FORTH, Greece

D.M. Klimov
Institute of Problems of Mechanics (RAS), Russia

G.E. Kodzhaspirov
Peter the Great St.Petersburg Polytechnic University, Russia

S.A. Kukushkin
Institute of Problems of Mechanical Engineering (RAS), Russia

T.G. Langdon
University of Southampton, U.K.

V.P. Matveenko
Institute of Continuous Media Mechanics (RAS), Russia

A.I. Melker
Peter the Great St.Petersburg Polytechnic University, Russia

Yu.I. Meshcheryakov
Institute of Problems of Mechanical Engineering (RAS), Russia

N.F. Morozov
St.Petersburg State University, Russia

R.R. Mulyukov
Institute for Metals Superplasticity Problems (RAS), Russia

Yu.V. Petrov
St.Petersburg State University, Russia

N.M. Pugno
Politecnico di Torino, Italy

B.B. Rath
Naval Research Laboratory, USA

A.E. Romanov
Ioffe Physico-Technical Institute (RAS), Russia

A.M. Sastry
University of Michigan, Ann Arbor, USA

B.A. Schrefler
University of Padua, Italy

N.V. Skiba
Institute of Problems of Mechanics (RAS), Russia

A.G. Sheinerman
Institute of Problems of Mechanics (RAS), Russia

R.Z. Valiev
Ufa State Aviation Technical University, Russia

K. Zhou
Nanyang Technological University, Singapore

“Materials Physics and Mechanics” Editorial Office:

Phone: +7(812)591 65 28 **E-mail:** mpnjournal@spbstu.ru **Web-site:** <http://www.mpm.spbstu.ru>

International scientific journal "Materials Physics and Mechanics" is published by Peter the Great St.Petersburg Polytechnic University in collaboration with Institute of Problems of Mechanical Engineering of the Russian Academy of Sciences in both hard copy and electronic versions.

The journal provides an international medium for the publication of reviews and original research papers written in English and focused on the following topics:

- Mechanics of nanostructured materials (such as nanocrystalline materials, nanocomposites, nanoporous materials, nanotubes, quantum dots, nanowires, nanostructured films and coatings).
- Physics of strength and plasticity of nanostructured materials, physics of defects in nanostructured materials.
- Mechanics of deformation and fracture processes in conventional materials (solids).
- Physics of strength and plasticity of conventional materials (solids).

Owner organizations: Peter the Great St. Petersburg Polytechnic University; Institute of Problems of Mechanical Engineering RAS.

Materials Physics and Mechanics is indexed in Chemical Abstracts, Cambridge Scientific Abstracts, Web of Science Emerging Sources Citation Index (ESCI) and Elsevier Bibliographic Databases (in particular, SCOPUS).



МЕХАНИКА И ФИЗИКА МАТЕРИАЛОВ

Materials Physics and Mechanics

Том 34, номер 1, 2017 год

**Proceedings of the Seventeenth International
Workshop on Nano–Design, Technology
and Computer Simulations
dedicated to V.A. Stepanov**

26-27 October, 2017, Minsk, Belarus

Organized by

**Belarusian State University of Informatics and Radioelectronics
(Belarus)**

**St. Petersburg Academy of Sciences on Strength Problems
(Russia)**

Edited by

Alexander I. Melker and Viktor R. Stempitsky

Учредители:

ФГАОУ ВО «Санкт-Петербургский политехнический университет Петра Великого»
ФГБУН «Институт проблем машиноведения Российской Академии Наук»

Редакционная коллегия журнала

Главные редакторы:

д.ф.-м.н., чл.-корр. РАН **Д.А. Индейцев**
Институт проблем машиноведения Российской Академии Наук
(РАН)

д.т.н., академик РАН **А.И. Рудской**
Санкт-Петербургский политехнический университет
Петра Великого

Основатель и почетный редактор: д.ф.-м.н. **И.А. Овидько (1961-2017)**
Институт проблем машиноведения Российской Академии Наук (РАН)

Ответственные редакторы

д.ф.-м.н. **А.Л. Колесникова**
Институт проблем машиноведения Российской Академии Наук
(РАН)

к.т.н. **А.С. Немов**
Санкт-Петербургский политехнический университет Петра
Великого

Международная редакционная коллегия:

д.ф.-м.н., проф. **А.К. Беляев**
Институт проблем машиноведения РАН, Россия
д.ф.-м.н. **С.В. Бобылев**
Институт проблем машиноведения РАН, Россия
к.т.н., проф. **А.И. Боровков**
Санкт-Петербургский политехнический у-т Петра Великого, Россия
д.ф.-м.н., проф. **Р.З. Валиев**
Уфимский государственный технический университет, Россия
д.ф.-м.н., академик РАН **И.Г. Горячева**
Институт проблем механики РАН, Россия
д.ф.-м.н., академик РАН **Д.М. Климов**
Институт проблем механики РАН, Россия
д.т.н., проф. **Г.Е. Коджаспиров**
Санкт-Петербургский политехнический у-т Петра Великого, Россия
д.ф.-м.н., проф. **С.А. Кукушкин**
Институт проблем машиноведения РАН, Россия
д.ф.-м.н., академик РАН **В.П. Матвеевко**
Институт механики сплошных сред РАН, Россия
д.ф.-м.н., проф. **А.И. Мелькер**
Санкт-Петербургский политехнический у-т Петра Великого, Россия
д.ф.-м.н., проф. **Ю.И. Мещеряков**
Институт проблем машиноведения РАН, Россия
д.ф.-м.н., академик РАН **Н.Ф. Морозов**
Санкт-Петербургский государственный университет, Россия
д.ф.-м.н., чл.-корр. РАН **Р.Р. Мудюков**
Институт проблем сверхпластичности металлов РАН, Россия
д.ф.-м.н., чл.-корр. РАН **Ю.В. Петров**
Санкт-Петербургский государственный университет, Россия
д.ф.-м.н., проф. **А.Е. Романов**
Физико-технический институт им. А.Ф. Иоффе РАН, Россия
д.ф.-м.н. **Н.В. Скиба**
Институт проблем машиноведения РАН, Россия
д.ф.-м.н., проф. **А.Б. Фрейлиш**
Институт проблем машиноведения РАН, Россия
д.ф.-м.н. **А.Г. Шейнман**
Институт проблем машиноведения РАН, Россия

Prof., Dr. **E.C. Aifantis**
Aristotle University of Thessaloniki, Greece
Dr. **K.E. Aifantis**
University of Florida, USA
Dr. **U. Balachandran**
Argonne National Laboratory, USA
Dr. **A. Bellosi**
Research Institute for Ceramics Technology, Italy
Prof., Dr. **G.-M. Chow**
National University of Singapore, Singapore
Prof. Dr. **Yu. Estrin**
Monash University, Australia
Prof., Dr. **Y. Gogotsi**
Drexel University, USA
Prof. Dr. **D. Hui**
University of New Orleans, USA
Prof., Dr. **G. Kiriakidis**
IESL/FORTH, Greece
Prof., Dr. **T.G. Langdon**
University of Southampton, UK
Prof., Dr. **N.M. Pugno**
Politecnico di Torino, Italy
Dr. **B.B. Rath**
Naval Research Laboratory, USA
Prof., Dr. **A.M. Sastry**
University of Michigan, Ann Arbor, USA
Prof., Dr. **B.A. Schrefler**
University of Padua, Italy
Prof. Dr. **K. Zhou**
Nanyang Technological University, Singapore

Тел.: +7(812)591 65 28 E-mail: mpmjournal@spbstu.ru Web-site: <http://www.mpm.spbstu.ru>

Тематика журнала

Международный научный журнал "Materials Physics and Mechanics" издается Санкт-Петербургским политехническим университетом Петра Великого в сотрудничестве с Институтом проблем машиноведения Российской Академии Наук в печатном виде и электронной форме. Журнал публикует обзорные и оригинальные научные статьи на английском языке по следующим тематикам:

- Механика наноструктурных материалов (таких как нанокристаллические материалы, нанокompозиты, нанопористые материалы, нанотрубки, наноструктурные пленки и покрытия, материалы с квантовыми точками и проволоками).
 - Физика прочности и пластичности наноструктурных материалов, физика дефектов в наноструктурных материалах.
 - Механика процессов деформирования и разрушения в традиционных материалах (твердых телах).
 - Физика прочности и пластичности традиционных материалов (твердых тел).
- Редколлегия принимает статьи, которые нигде ранее не опубликованы и не направлены для опубликования в другие научные издания. Все представляемые в редакцию журнала "Механика и физика материалов" статьи рецензируются. Статьи могут отправляться авторам на доработку. Не принятые к опубликованию статьи авторам не возвращаются.

Журнал "Механика и физика материалов" ("Materials Physics and Mechanics") включен в систему цитирования Web of Science Emerging Sources Citation Index (ESCI), SCOPUS и РИНЦ.

© 2017, Санкт-Петербургский политехнический университет Петра Великого
© 2017, Институт проблем машиноведения Российской Академии Наук

Contents

Unified approach to forming fullerenes and nanotubes	1-17
Alexander I. Melker and Maria A. Krupina	
Modeling growth of midi-fullerenes from C₂₀ to C₆₀	18-28
Alexander I. Melker and Maria A. Krupina	
Modeling growth of midi-fullerenes from C₄₈ to C₇₂	29-36
Alexander I. Melker and Maria A. Krupina	
Fullerenes of the $\Delta N=10$ series	37-45
Alexander I. Melker, Maria A. Krupina, Ruslan M. Zarafutdinov	
Fullerenes of the $\Delta N=12$ series	46-50
Alexander I. Melker, Maria A. Krupina, Ruslan M. Zarafutdinov	
Design and simulation of additive manufactured structures of three-component composite material	51-58
A.Yu. Zobacheva, A.S. Nemov, A.I. Borovkov, A.D. Novokshenov, M.V. Khovaiko, N.A. Ermolenko	
Validation of EuroNCAP frontal impact of frame off-road vehicle: road traffic accident simulation	59-69
S. Alekseev, A. Tarasov, A. Borovkov, M. Aleshin, O. Klyavin	
NVH analysis of offroad vehicle frame. Evaluation of mutual influence of body-frame system components	70-75
A. Patrikeev, A. Tarasov, A. Borovkov, M. Aleshin, O. Klyavin	
Integrated system as a tool for implementation of simulation- and optimization-based design methodology	76-81
Aleksei Novokshenov, Alexander Nemov, Dmitriy Mamchits, Aleksandra Zobacheva	
Vehicle dynamics prediction module	82-89
J. Leoro, S. Krutitskiy, A. Tarasov, A. Borovkov, M. Aleshin, O. Klyavin	
Applicability of polymer composite materials in the development of tractor falling-object protective structures (FOPS)	90-96
Dmitrii Lebedev, Alexey Okunev, Mikhail Aleshin, Kirill Ivanov, Oleg Klyavin, Svetlana Nikulina, Oleg Rozhdestvenskiy, Alexey Borovkov	
Variational problem for hydrogenerator thrust bearing	97-102
O.V. Antonova, A.I. Borovkov, Yu.Ya. Boldyrev, I.B. Voynov	

PREFACE

The Seventeenth International Workshop on Nano-Design, Technology and Computer Simulations (NDTCS-2017) took place on October 25-26, 2017 in Minsk, Belarus. The workshop NDTCS-2013 was organized jointly by Belarusian State University of Informatics and Radioelectronics and the St. Petersburg Academy of Sciences on Strength Problems (Russia). More than 149 participants including scientists, teachers, graduate students and undergraduates from Azerbaijan, Belarus, Germany, Kazakhstan, Lithuania, Poland, Russian Federation and Vietnam prepared and delivered more than 60 reports. The Fifteenth Workshop was focused on nanomaterials, computational methods in the field of micro- and nanoelectronics, and mechanics.

Joint Stock Company 'Integral', leading company in the design and manufacturing integrated circuits, acted as the partner and supporter of Workshop.

Workshop NDTCS-2017 is a continuation of the previous workshops, which were held in:

- 1997-2005, St. Petersburg (Russia)
- 2006, Olsztyn (Poland)
- 2007, Bayreuth (Germany)
- 2008, 2013, Minsk (Belarus)
- 2009, Vilnius (Lithuania)
- 2011, Espoo (Finland)
- 2015, Grodno (Belarus)

The first nine workshops, which took place in Russia, had the name "Nondestructive Testing and Computer Simulations in Science and Engineering." In due course, the focus of the meetings gradually moved towards Nanoscience and Nanotechnology, so the following workshops (2007-2015) had the new name "International Workshop on New Approaches to High-Tech: Nano-Design, Technology and Computer Simulations" what reflects better their profile.

All the contributions to the Workshops were published in English.

- Proceedings of St. Petersburg Academy of Sciences on Strength Problems (SPAS), vols. 2-11 (1998–2007);
- Proceedings of NDTCS, vols. 12, 13, 15, 16 (2008, 2009, 2013);
- Proceedings of the International Society for Optical Engineering (SPIE), vols. 3345, 3687, 4064, 4348, 4627, 5127, 5400, 5831, 6253, 6597, 7377 (1998–2008);
- Modelling and Computer Simulation in Materials Science and Engineering, 6 (4) (1998);
- Reviews on Advanced Materials Science, 20 (1, 2) (2009);
- Materials Physics and Mechanics, 9 (1, 2, 3) (2010); 13 (1, 2); (2012); 20 (1, 2) (2014);
- St. Petersburg State Polytechnical Journal. Physics and Mathematics, 2(242), 3(248), 4(253) (2016); 10 (1) (2017).

This issue of Materials Physics and Mechanics Journal contains the selected papers presented at the Workshop. All the papers have been peer-reviewed prior to publication. The issue will be of interest to researchers and graduate students in the field of nanotechnology, physics, chemistry, and mechanics.

Alexander I. Melker, Viktor R. Stempitsky



Vasily Andreevich STEPANOV
(1917-1985)

On 8 October, 2017, a hundred years have passed since the outstanding scientist in the field of studying physical-mechanical properties of materials, Doctor of Technical Sciences, Professor Stepanov V.A. was born in the Nemolovo village that was the part of Luga district (uezd) of Petrograd province (guberniya). After finishing a secondary school, he went to Leningrad Industrial Institute (now Peter the Great St. Petersburg Polytechnic University) in 1933 and graduated summa cum laude in 1939; his specialty having been Physical Metallurgy. From 1939 to 1946 V.A. Stepanov worked at the Industrial laboratory of Leningrad Metallic Plant, at first as an engineer and since 1944 as the Head of laboratory. In July, 1943 he was awarded the medal “For defense of Leningrad”.

In 1946 V.A. Stepanov was invited by Academician N.N. Davidenkov to A.F. Ioffe Physico-Technical Institute of the Academy of Sciences of the U.S.S.R. Here for more than 45 years V.A. Stepanov worked at the laboratory “Dynamics of Strength of Materials”, being in the last few decades the Laboratory Head. In addition to intensive research activity, teaching was an important part of Stepanov’s life. Almost 20 years he was in parallel simultaneously the Head of Department of Metal Physics at Leningrad Polytechnical Institute. He lectured original courses on physical strength of materials. As a result of his activity both in scientific and

educational field, a lot of his disciples have become PhD, Doctors of Sciences, Professors; now they are working with success in science, industry and education.

His great achievements refer to the area of exploration known as “High-Velocity Impact Phenomena”. This subject matter is of paramount importance for both fundamental science and technical, including military, applications.

In addition to those investigations, V.A. Stepanov made an important contribution to the new approach for a fundamental understanding of strength of materials. The approach which is known as “Kinetic Concept of Strength”, considers strength, time and temperature as inextricably connected values.

Of special note is his role in the development of computer simulations (and especially molecular dynamics) investigations in the Soviet Union. It should be remembered that molecular dynamics was born in 1956 in the U.S.A. In the middle of seventies the number of molecular-dynamics results became so large that the First International Conference on Computer Simulations Applied to Materials took place in the U.S.A. in 1976. At that time the number of molecular-dynamics researchers in the Soviet Union did not exceed two dozens. It was connected with the lack of computers as well as with the lack of understanding from the majority of old generation scientists. Fortunately, V.A. Stepanov belonged to the innovative minority which understood the importance of this new direction of science. With his help, in March, 1976, All-Union Seminar on Computer Simulations of Radiation and Other Defects was established on the basis of Department of Metal Physics (Leningrad Polytechnic Institute) and A.F. Ioffe Physico-Technical Institute of Academy of Sciences of the U.S.S.R.

It should be emphasized that the International Workshop on New Approaches to High-Tech: Nano-Design, Technology, Computer Simulations is a direct successor of the above mentioned Seminar. The articles on the properties of materials in this issue of Materials Physics and Mechanics Journal are dedicated to the memory of V.A. Stepanov.

He was a cheerful person. He played tennis, liked skiing. Once with his friends he went on a many-days bicycle tour from Leningrad to Crimea. There is no doubt that V.A. Stepanov was a splendid, sincere, decent, and noble person with a great sense of responsibility for any problem he dealt with. He was a very hard-working person with high standards for himself as well as for his colleagues. We will hold Vasiliy Andreevich Stepanov as an eminent person, scientist, and teacher in our hearts forever.



Colleagues and Disciples

UNIFIED APPROACH TO FORMING FULLERENES AND NANOTUBES

Alexander I. Melker^{1*} and Maria A. Krupina²

¹Department of Mechanics and Control Processes,

²Department of Experimental Physics,

Peter the Great St. Petersburg Polytechnic University, Polytekhnicheskaya 29

195251, St. Petersburg, Russia

*e-mail: newton@imop.spbstu.ru

Abstract. Reactions of elementary fullerenes (from C₄ to C₁₂) with each other as well as with their heirs are considered. Under the elementary fullerenes we understand a tetrahedron, a cube, and triangular, pentagonal and hexagonal prisms. The process is similar to fusion of bubbles in a soap solution. The graphs describing the process are suggested. The reaction zone is a vertex-connected subgraph that takes into account physical restrictions, namely that covalent bonds exist only between nearest-neighbor atoms. We supposed that during the reactions new covalent bonds are formed and old covalent bonds between the reacting atoms are destroyed. The clusters obtained resemble both fullerenes and nanotubes.

Keywords: fullerene, fusion, graph, growth, nanotube.

1. Introduction

Discoveries and consequences. Since the discovery of fullerenes [1, 2], carbon nanotubes [3], and graphene [4, 5] carbon occupies a strategic position in materials science and technology as one of the most versatile and far-reaching materials [6-17]. Two small fullerenes have been detected with the mass spectroscopic method, C₃₆ [18] and C₂₀ [19]. The synthesis and separation of molecules C₃₆ from arc derived carbon has attracted considerable attention, since fullerenes smaller than C₆₀ are highly strained due to the presence of fused five-membered rings. Caged molecules with low mass in the fullerene family are especially interesting because of their high curvature and increased strain energy that give rise to high reactivity.

Small fullerenes. Current studies on fullerenes and their compounds focus on large-size fullerenes mainly. Systematic studies on small (middle-size) fullerenes and non-isolated-pentagon-ring (IPR) fullerenes are less common. The structure and stability of fullerenes containing less than 60 carbon atoms have been studied experimentally and theoretically [17-70]. Experimental researches of such fullerenes are still limited by low yield and poor stability. As a result, theoretical methods prevail. Only works [18, 19, 21, 33, 56, 57, 60, 65, and 67] refer to experimental investigations. Endohedral metallofullerenes MC₂₈ were obtained in Ref. [57] where M=Ti, Zr, U. In Ref. [33] decachlorofullerene C₅₀Cl₁₀ was synthesized.

The most comprehensive experimental study [60] revealed the following. (We conserve here the terminology by the authors). In the mass spectra of products of benzene pyrolysis, the authors found out the ions of all kinds of carbon molecules including *a*) small carbon molecules (C₃-C₂₀); *b*) quasi-fullerenes C₂₁, C₂₃, C₃₃, C₄₈, C₅₂, C₅₄, C₅₆ and C₅₈; *c*) hydrides of small carbon molecules, C₅H₂, C₁₀H₄, C₁₄H₄, C₁₆H₈ and C₁₈H₂, *d*) hydrides of quasi-fullerenes: C₂₅H₂, C₂₇H₂, C₃₁H₄, C₃₇H₆, C₃₉H₆, C₄₃H₈, C₄₇H₁₀ and C₄₉H₁₀. In the authors' opinion [60] the absence of

appreciable progress in synthesis C_n ($n < 20$) and quasi-fullerenes is determined by the domination of hypothesis that carbon atoms are always necessary for growth of carbon molecules; their generating being possible only under carbon sublimation.

The theoretical methods are helpful in this field to discover some potential compounds with good properties. The most of them refer to searching criteria on the stability of fullerene molecules having different structures. This is an important task because the influence of fullerene structure on their stability and properties is crucial. We will not analyze the methods used by the authors since they have both advantages and drawbacks. "Carbon, however, appears able to break so many rules that one must continually reconsider them for this element. It is, after all, only after a great deal of study that the structures of even the smallest molecules such as C_2 and C_3 have been characterized and understood theoretically. Such studies urge caution in being too hasty with regards to assumptions about the electronic and geometric structure of carbon compounds in terms of conventional valence theory" wrote Harold W. Kroto who shared the 1996 Nobel Prize for chemistry for his co-discovery of fullerenes [2]. We consider the theoretical studies from the point of view of the aims that their authors set themselves. On this basis the theoretical investigations can be divided into several groups.

1) The authors studied well-established experimentally fullerenes; their properties, the stability of their isomers, and the interactions with other molecules [24, 25, 32, 46, 52, 54, 62].

2) The authors studied the stability of different isomers of one and the same fullerene. The isomer structures are chosen from a lot of postulated combinatorial ones [53, 68 and 70].

3) The authors tried to fulfill the gap between the fullerenes found experimentally and those that could be synthesized. The structure of theoretically possible fullerenes was also postulated [20, 22, 23, 28, 29, 31, 35-39, 43, 44, 47-51, 66, 69].

It must be emphasized that most investigations of small fullerenes have centered on either obtaining these materials experimentally or theoretical studying properties of these materials which structure was usually postulated. To our mind, the crucial questions for advanced applications of all the fullerenes are: how the materials are originated and what structure they obtain. Answer to these questions gives the possibility to develop nanotechnology on a scientific basis.

Nucleation and growth. Up to now mechanism of fullerene- and nanotube-formation is a controversial point. Many different models have been proposed to explain their formation [41, 56-59, 61, 63-67, 69, 72-92]. The known mechanisms can be categorized into two major groups: bottom-up and top-down models. In the first case, fullerene cages and nanotubes are considered to be formed from carbon atoms and small carbon clusters [41, 56, 57, 59, 64, 69, 72-76, 81, 82, 90-92]. To the first group one could also refer such mechanism as the growth of small endohedral metallofullerenes by 'eating' vaporized carbon [69]. In the second case, fullerenes and nanotubes are thought as direct transformation of graphene into fullerenes or nanotubes [27, 58, 61, 63, 77-79, 83, 85, 86].

There is also a group of researchers interested in cosmic studies [58, 65, 67]. Since a key component of the carbon dust inventory in planetary nebulae are polycyclic aromatic hydrocarbons and their species, the authors suggest various mechanisms of formation five-membered rings in these molecules under irradiation, the molecule dehydrogenation and fusion leading to fullerene formation. One of the recent experimental studies connected with radiation damage is electron-beam-induced transformation of sumanene crystals into carbon cages [89]. Sumanene molecule $C_{21}H_{12}$ with C_{3v} symmetry has three five-membered rings and is considered as a key fullerene fragment together with corannulene $C_{20}H_{10}$ with C_{5v} symmetry having one five-membered ring [93]. From the mechanism viewpoint, these investigations refer to the second group.

Dehydrogenated corannulene was used as a basic structural unit for nucleation of fullerenes and single-walled carbon nanotubes (SWNT) in Ref. [80]. The entities are considered

in the framework of elasticity theory. Existence of curved surfaces introduces forces that depend on the properties of the particular surfaces. The elasticity theory relates the surface tension to the tangential stresses. Any deviation from sphericity deals with stretching as the first-order effect and bending as the second-order one. On the other hand, the conversion of a graphene sheet into cylindrical tubule does not require stretching and bending becomes the first-order effect. Since the nucleation conditions could be different, the cluster of carbon atoms can form the cap of a nanotube or a fullerene. These conclusions received the experimental support in Ref. [86], where at small helium pressure, graphene layers and fullerene-like structures were observed. At high pressure, surface morphology of the anode was changed and evolution of carbon nanotubes was observed.

For completeness sake the studies connected with mathematical description of fullerene and nanotube growth should be mentioned. The typical examples are Refs. [74, 84]. One of them develops the probability-kinetic approach [74], the other uses the theory of diffusion [84]. Both approaches need input parameters that must be obtained from experiments or independent calculations.

Geodesy and topology. Any numerical calculations of fullerene energy and other properties need input data. For small fullerenes the number of possible configurations is not very large, but as one passes to middle-sized fullerenes one obtains a monstrous number of isomers. It is clear that there is no big sense in studying all of them, so it is desirable to restrict their number to the most stable ones. Now there are two restrictive analytical methods [94-98, 100 and references therein, 101]. The first is a combination of graph theory with group theory and could be named geometric modeling. It is based on the principle “the minimum surface at the maximum volume”. It means that a forming fullerene tends to take the form of a perfect spheroid with equal covalent bonds. The geometric modeling allows imagine from the very beginning a possible way of growing carbon clusters and thereby to decrease the number of configurations being worth for studying.

Another new analytical restriction method refers to persistent homology [99]. Homology is formalization of an intuitive idea on confining sets; in this context fullerene set. The authors connected some topological characteristics (barcodes) with the heat of formation and the total curvature energy of fullerene isomers. As any topological method, similar to the graph approach, it needs more precise formulation in order to become a really quantitative method. In the graph approach it was the requirement: symmetry of dimetric representation and graph must be uniform [95-98]. Nevertheless the method of persistent homology is rather interesting since the authors have considered fullerenes and nanotubes in the context of a single theory.

New approach to fullerenes. In Ref. [55] we have enlarged the term “fullerene” upon any convex shape inscribed into a spherical surface which can be composed of atoms, each atom having three nearest neighbors, as in usual fullerenes, whenever discussing hollow carbon clusters. This new approach allowed us to obtain possible forms of mini-fullerenes, from C_4 to C_{20} that, in its turn, allowed filling up a gap between classical fullerenes and small carbon cages including in the list of fullerenes such broad-sense fullerenes. The next step was done in Ref. [95], where the diagrams, showing the formation of mini-fullerenes from single carbon atoms and carbon dimers, were suggested. In addition to the diagrams, here the graph theory was used for analysis of the fullerene structures obtained. The graph analysis allows solving also an inverse problem, i.e. how to predict the ways of producing possible fullerenes, if one knows their graphs [96, 97]. We have designed the structure of some fullerenes from twenty to forty-eight starting at basic mini-fullerenes [91, 97, 98]. It is worth noting that in doing so we have obtained fullerene C_{36} with D_{6h} symmetry. It was synthesized and separated from arc derived carbon soot at UC, Berkeley [18].

Arrhenius' postulate. In 1889 Svante August Arrhenius postulated that a chemical reaction goes as follows [102] $A + B \leftrightarrow (AB) \rightarrow Y + Z$. It means that at first there forms some

intermediate compound and only afterwards a usual chemical reaction is going on. For fullerenes and nanotubes this postulate leading to fusion reactions can be written in the form $C_n + C_m \rightarrow (C_n C_m) \rightarrow C_{n+m}$. In Ref. [92] we have developed an algorithm that has proved itself in predicting the growth of perfect fullerenes conserving an initial symmetry, so called the fusion reaction algorithm which is based on this postulate. Following the postulate we considered recently some fullerene reactions and have obtained fullerenes of the $\Delta n=6$ periodicity C_{14} , C_{18} , C_{24} , C_{30} and C_{36} [103]; of $\Delta n=8$ periodicity C_{20} , C_{24} , C_{32} , C_{40} and C_{48} [92]; of $\Delta n=10$ periodicity C_{26} , C_{30} , C_{40} , C_{50} and C_{60} [104]; of $\Delta n=12$ periodicity C_{32} , C_{36} , C_{48} , C_{60} and C_{72} [105]; and of $\Delta n=14$ periodicity C_{38} , C_{42} , C_{56} , C_{70} and C_{84} [106].

Aim of study. In radiation solid state physics it is well known that one and the same small vacancy cluster (embryo) during its growth can transform either into a void (volume configuration) or into a dislocation loop (plane configuration) [107]. The question arises whether such situation is possible for elementary fullerenes. Under the elementary fullerenes we understand a tetrahedron, a cube, and triangular, pentagonal and hexagonal prisms which were analyzed carefully in Refs. [55, 95, 96]. Here we think over fullerenes as volume configurations and nanotubes as curved plane configurations. In this contribution we try to answer this question.

2. Reactions of tetrahedral fullerene C_4

Reaction between two tetrahedrons and explanation of some notions. Suppose that two tetrahedral carbon molecules react in the following manner $C_4 + C_4 \rightarrow (C_4 C_4) \rightarrow C_8$. In Figure 1 the atomic configurations corresponding to this reaction are shown. At first two molecules C_4 are moving towards each other (Fig. 1a). Then the atoms, marked with red, interact with each other and produce a compound (Fig. 1b). During this process new covalent bonds (red lines) are formed and old covalent bonds between the reacting atoms (blue dotted lines) are destroyed. As a result, a distorted hexahedron is formed (Fig. 1c) which relaxes into a cube (Fig. 1d).

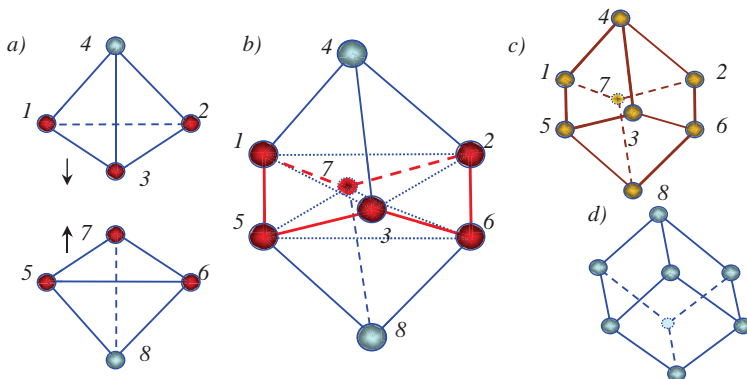


Fig. 1. Joining of two carbon tetrahedrons: *a)* separate tetrahedrons; covalent bonds (blue lines), reacting atoms (red spheres), neutral atoms (blue spheres); *b)* intermediate compound; new covalent bonds (red lines), old covalent bonds to be destroyed (blew dotted lines); *c)* distorted hexagon formed, *d)* hexagon (cube) after relaxation.

One can describe this process with the help of graph theory as it is done in Figure 2. Consider some notions of this theory [108]. Let we have two graphs G_1 and G_2 , each graph

having p_i vertices and q_i edges, $i = 1 \vee 2$. If one joins all the vertices of both graphs, one obtains a vertex-connected graph $G_1 + G_2$, where the number of vertices is $p_1 + p_2$, and the number of edges is $q_1 + q_2 + p_1 p_2$. If to remove vertex v_i from graph G_i , one obtains subgraph $G_i - v_i$. In our case we have graph G_1 with vertices 1, 2, 3, 4, and edges 12, 13, 23, 14, 24, 34; and graph G_2 having vertices 5, 6, 7, 8, and edges 56, 57, 67, 58, 68, 78 (Fig. 2a). Since not all the vertices take part in connecting two graphs, we need to exclude non-reactive vertices 4 and 8, as well as edges 14, 24, 34 and 58, 68, 78, connected with these vertices; therefore in reality we need to consider only subgraph $G_1 - v_4$ with vertices 1, 2, 3, and edges 12, 13, 23, and subgraph $G_2 - v_8$ with vertices 5, 6, 7, and edges 56, 57, 67. As a result, one obtains a vertex-connected subgraph $(G_1 - v_4) + (G_2 - v_8)$ with six vertices 1, 2, 3, 5, 6, 7, six old edges 12, 13, 23, 56, 57, 67, and nine new edges 15, 16, 17, 25, 26, 27, 35, 36, 37.

However, applying any mathematical model to physical problems, it is important to keep in mind that except of mathematical rules there are physical restrictions. In our case we must bear in mind that covalent bonds exist only between nearest-neighbor atoms. Therefore we must exclude also edges 16, 25, 37. As a result, we obtain a 'partially' vertex-connected subgraph having six vertices 1, 2, 3, 5, 6, 7, six old edges 12, 13, 23, 56, 57, 67, and six new edges 15, 17, 26, 27, 35, 36 (Fig. 2b). It is clear that analyzing this subgraph is a simpler task.

We supposed that during the reaction of two tetrahedrons new covalent bonds (red lines) are formed and old covalent bonds between the reacting atoms (blue lines) are destroyed. Both types of bonds are shown in the subgraph obtained as edges before destroying (Fig. 2b) and after (Fig. 2c). In the latter the broken bonds (edges) are shown by dotted lines. Here we added the fictitious vertex 7_f in order to show subgraph symmetry. Removing the broken bonds (edges) and adding the non-reactive vertices 4 and 8, as well as their edges 14, 24, 34 and 58, 68, 78, one obtains the graph corresponding to three-fold symmetry of the fullerene formed (Fig. 2d). To avoid the fictitious vertex 7_f , it is reasonable to pass on four-fold symmetry of the fullerene. In doing so one obtains the graph shown in Figure 2e.

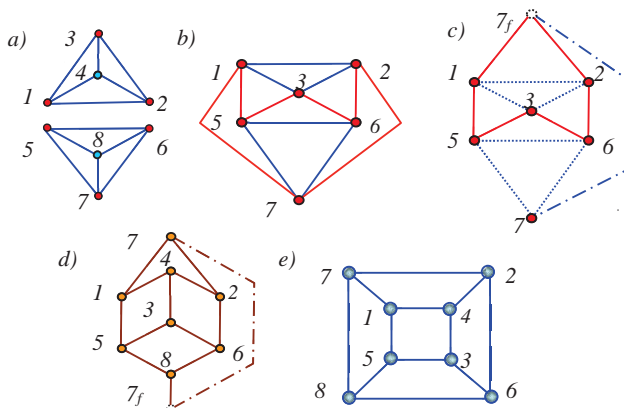


Fig. 2. Graphs: *a*) separate tetrahedrons; edges (blue lines), connectable vertices (red circles), neutral vertices (blue circles), *b*) partial vertex-connected subgraph; new connecting edges (red lines), *c*) removed edges (dotted blue lines), *d*) full graph reflecting three-fold symmetry of fullerene C_8 formed, *e*) full graph reflecting four-fold symmetry of fullerene C_8 formed.

Reactions of tetrahedron C_4 with triangular prism C_6 . In Figure 3 the atomic configurations corresponding to reaction $C_4 + C_6 \rightarrow (C_4C_6) \rightarrow C_{10}$ are shown. At first two molecules are moving towards each other (Fig. 3a). Then the atoms, marked with red, interact with each other to produce a compound (Fig. 3b). During this process new covalent bonds (red lines) are formed and old covalent bonds between the reacting atoms (blue dotted lines) are destroyed. As a result, fullerene C_{10} is formed (Fig. 3c). It is tri-(tetra-penta)₃ semiregular septahedron that resembles a lance-head.

Similar to the previous reasoning we can consider this reaction on the basis of graph theory. At first we have two independent graphs (Fig. 4a), then we obtain the partially vertex-connected graph having ten vertices, six stable and six unstable old edges, together with six new formed edges (Fig. 4b), and at last, the graph corresponding to three-fold symmetry of the fullerene formed is composed (Fig. 4c). We see again that analyzing the fullerene reaction in the frame of graph representation is a simpler task. Obviously that it is connected with the fact that the graph approach reduces a three-dimensional problem to a two-dimensional one.

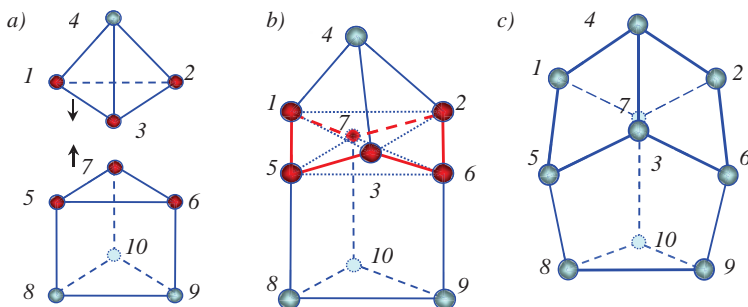


Fig. 3. Joining of a tetrahedron to a triangular-prism: a) separate tetrahedron and triangular prism; covalent bonds (blue lines), reacting atoms (red spheres), neutral atoms (blue spheres), b) intermediate compound; new covalent bonds (red lines), c) semiregular septahedron fullerene C_{10} .

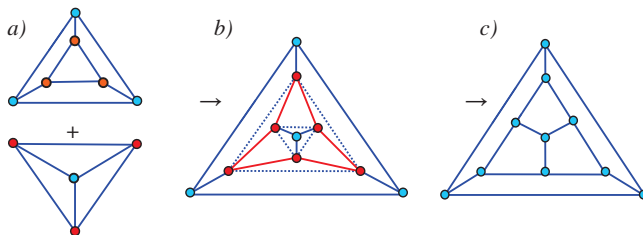


Fig. 4. Connection of graphs: a) separate graphs corresponding to a triangular prism (above) and a tetrahedron (below), b) connection with physical restrictions, c) graph of tri-(tetra-penta)₃ fullerene shown in Fig. 3c. All notations are the same as before.

Reaction $C_4 + C_{10} \rightarrow (C_4C_{10}) \rightarrow C_{14}$. Since the graph approach is simpler, we begin with it. At first we have two independent graphs (Fig. 5a), then we obtain the partially vertex-connected graph having fourteen vertices, twelve stable and six unstable old edges, together

with six new formed edges (Fig. 5b), and at last, the final graph is composed (Fig. 5c). This graph corresponds to three-fold symmetry of the fullerene formed (Fig. 5d) and could be named as a tetragonal trefoil-pair (or shamrock-pair) polyhedron. Its energy was calculated in Ref. [103]. In Figure 5e the isomorphic graph of the fullerene is also given. It shows better a structure and symmetry of this polyhedron.

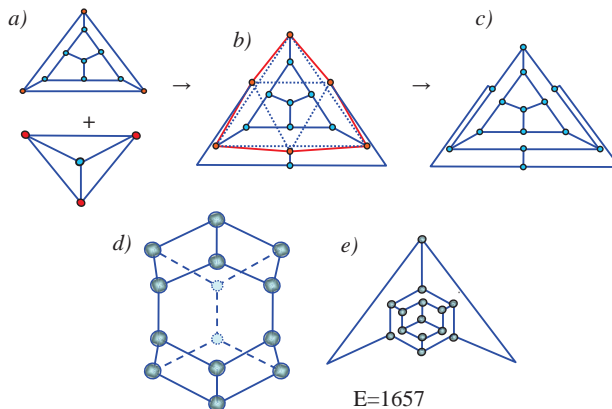


Fig. 5. Connection of graphs: *a)* separate graphs corresponding to a semiregular septahedron fullerene (above) and a tetrahedron (below), *b)* connection with physical restrictions, *c)* final graph, *c)* tetragonal trefoil polyhedron C_{14} obtained, *e)* isomorphic graph. All notations are the same as before.

Reactions of tetrahedron C_4 with triangular barrel C_{12} . This fullerene C_{12} was named in [96] as a triangular barrel-shaped fullerene or a rugby ball. In Ref. [55] possible ways of its formation, initiated both by a reaction-active single atom and by a reaction-active dimer, were considered. The ways resemble formation of a zigzag polymer during polymerization. In Ref. [96] it was suggested that the fullerene can be also originated from a three-atom cluster. Reaction $C_4 + C_{12} \rightarrow (C_4C_{12}) \rightarrow C_{16}$ is displayed in Figure 6 as a connection of graphs, together with a fullerene obtained.

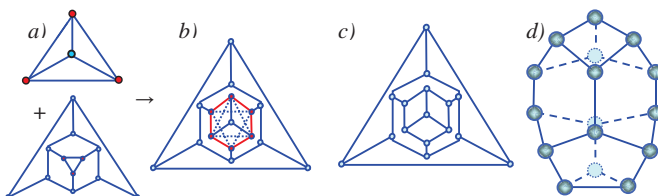


Fig. 6. Connection of graphs: *a)* separate graphs corresponding to a tetrahedron (above) and a triangular barrel-shape polyhedron (below), *b)* connection with physical restrictions, *c)* final graph of semiregular decahedron C_{14} (*d*). All notations are the same as before.

Reaction $C_4 + C_{16} \rightarrow (C_4C_{16}) \rightarrow C_{20}$ is shown in Figure 7 as a connection of graphs, together with a fullerene obtained. Contrary to the semiregular decahedron that can be inscribed in an ellipsoid and therefore can be identified as a fullerene, the irregular dodecahedron resembles more a two-closed-end mini-nanotube.

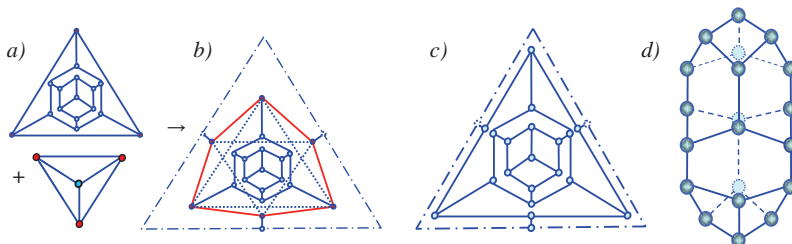


Fig. 7. Connection of graphs: *a)* separate graphs corresponding to a semiregular decahedron (above) and a tetrahedron (below), *b)* connection with physical restrictions, *c)* final graph of an irregular dodecahedron (*d)*). All notations are the same as before.

3. Reactions of triangular-prism fullerene C_6

Reaction between two triangular prisms can be written as $C_6 + C_6 \rightarrow (C_6C_6) \rightarrow C_{12}$ and is presented in Figure 8 as a connection of graphs, together with a fullerene obtained. As already noted the fullerene was named in [2, 3] as a triangular barrel-shaped fullerene or a rugby ball. In [2] a possible way of its formation, initiated by a reaction-active single atom as well as by a reaction-active dimer, was considered. The way resembles formation of a zigzag polymer during polymerization. In [3] it was suggested that the fullerene can be also originated from a three-atom cluster. Now we have the third way of this fullerene formation.

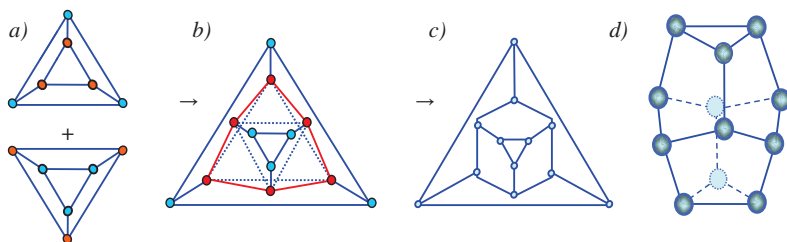


Fig. 8. Connection of graphs: *a)* separate graphs corresponding to triangular prisms; *b)* connection with physical restrictions; *c)* final graph of a triangular barrel-shaped fullerene (*d)*). All notations are the same as before.

Reaction of triangular prism C_6 and barrel C_{12} $C_6 + C_{12} \rightarrow (C_6C_{12}) \rightarrow C_{18}$ is exhibited in Figure 9 as connection of graphs, together with a fullerene obtained. The fullerene was named in Refs. [2, 3] as a truncated bi-shamrock. Some possible ways of forming this cluster initiated by a reaction-active single atom as well as by a reaction-active dimer, were suggested in [2]. Now they seem us too complex in comparison with that of considered here.

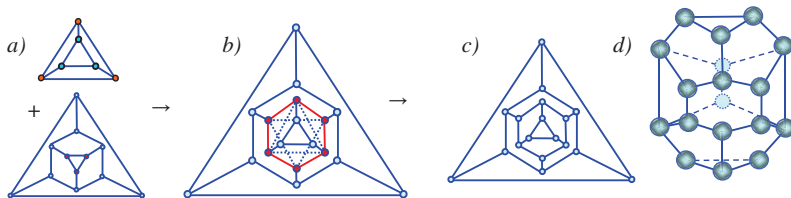


Fig. 9. Connection of graphs: *a*) separate graphs corresponding to a triangular prism (above) and a triangular barrel-shaped fullerene (below), *b*) connection that takes into account physical restrictions, *c*) final graph of truncated bi-shamrock fullerene C_{18} (*d*). All notations are the same as before.

Reaction $C_6 + C_{16} \rightarrow (C_6C_{16}) \rightarrow C_{22}$ is illustrated in Figure 10 as connection of graphs, together with a cluster obtained. The carbon cluster is a one closed-end mini-nanotube. Contrary to the irregular dodecahedron with closed ends (Fig. 7d), this nanotube is able to growing by adding triangular prisms as it shown in Figure 10e. The corresponding reactions can be written as follows

$$C_6 + C_{22} \rightarrow C_{28}, \quad C_6 + C_{28} \rightarrow C_{34}, \quad \dots \quad C_6 + C_N \rightarrow C_{N+6}, \quad N = 16 + 6n, \quad n = 1, 2, \dots$$

It is clear that the growth of the nanotube will be stopped if instead of adding triangular prisms, tetrahedrons are appended to the nanotube. In this case one obtains nanotubes according to the reactions

$$C_4 + C_{16} \rightarrow C_{20}, \quad C_4 + C_{22} \rightarrow C_{26}, \quad C_4 + C_{28} \rightarrow C_{32}, \quad \dots \quad C_4 + C_N \rightarrow C_{N+4}, \quad N = 16 + 6n, \quad n = 1, 2, \dots$$

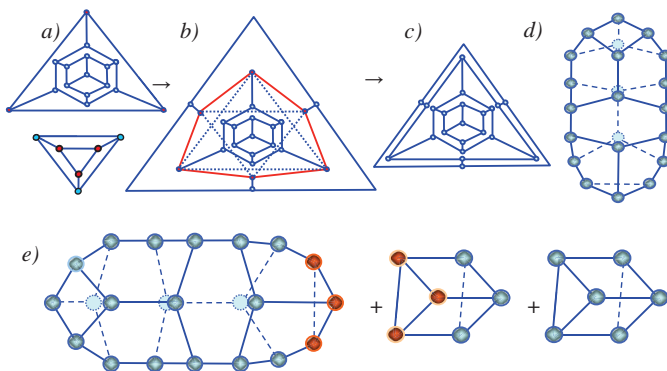


Fig. 10. Connection of graphs: *a*) separate graphs corresponding to an irregular dodecahedron (above) and a triangular prism (below), *b*) connection with physical restrictions, *c*) final graph of a nanotube (*d*); *e*) growth of the nanotube obtained.

Reaction $C_6 + C_{18} \rightarrow (C_6C_{18}) \rightarrow C_{24}$ is presented in Figure 11 as connection of graphs, together with a cluster obtained. The carbon cluster is an opened-end mini-nanotube. Contrary to the previous case, this nanotube is able to growing by adding triangular prisms to both ends. The corresponding reactions can be written as follows

$$C_6 + C_{24} \rightarrow C_{30}, \quad C_6 + C_{30} \rightarrow C_{36}, \quad \dots \quad C_6 + C_N \rightarrow C_{N+6}, \quad N = 18 + 6n, \quad n = 1, 2, \dots$$

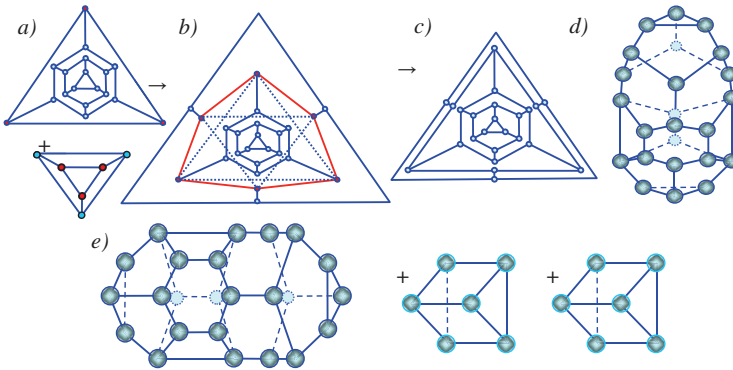


Fig. 11. Connection of graphs: *a)* separate graphs corresponding to a bi-shamrock (above) and a triangular prism (below), *b)* connection with physical restrictions, *c)* final graph of a nanotube (*d)*; *e)* growth of the nanotube obtained.

4. Reactions of cube fullerene C_8

Reaction between two cubes can be written as $C_8 + C_8 \rightarrow (C_8C_8) \rightarrow C_{16}$. Its graph representation is shown in Figure 12a. One of two initial cubes and a final geometric body are illustrated in Figure 12b.

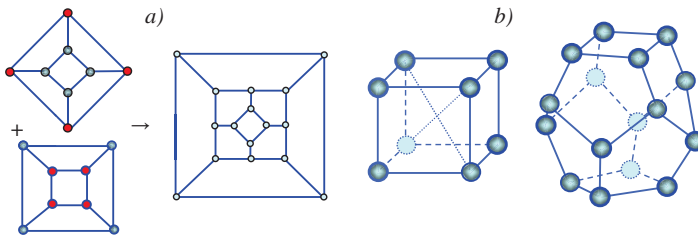


Fig. 12. Fusion of two cubes as connection of their graphs (*a)*; *b)* cube and square barrel-shape fullerene C_{16} .

Reactions of cube C_8 with square barrel C_{16} $C_8 + C_{16} \rightarrow (C_8C_{16}) \rightarrow C_{24}$ is presented in Figure 13 as connection of graphs, together with a fullerene formed. The final graph was designed earlier in Ref. [4] on different geometrical grounds, but the fullerene structure was not given. One can consider this carbon cluster not only as a fullerene, but an opened-end mininanotube as well. This nanotube is able to growing by adding carbon cubes to both ends. The corresponding reactions are

$$C_8 + C_{24} \rightarrow C_{32}, \quad C_8 + C_{32} \rightarrow C_{40}, \dots, C_8 + C_N \rightarrow C_{N+6}, \quad N = 16 + 8n, \quad n = 1, 2, \dots$$

It is worth noting that similar nanotube with $n=8$, $N=80$ was studied in Ref. [76].

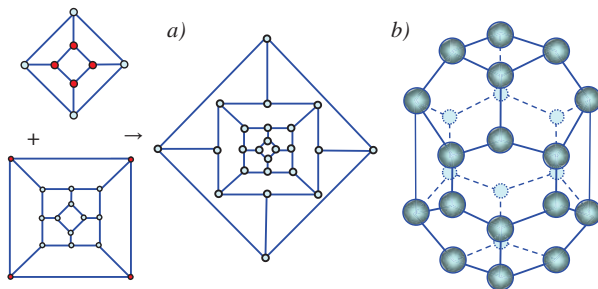


Fig. 13. Connection of graphs: *a)* separate graphs of a cube (above) and a square barrel-shape fullerene (below), as well as their connection; *b)* fullerene C_{24} obtained.

5. Reactions of pentagonal prism C_{10}

Reaction between two pentagonal prisms is written as $C_{10} + C_{10} \rightarrow (C_{10}C_{10}) \rightarrow C_{20}$. It is shown both as a graph connection and as an initial and a final geometric body in Figure 14.

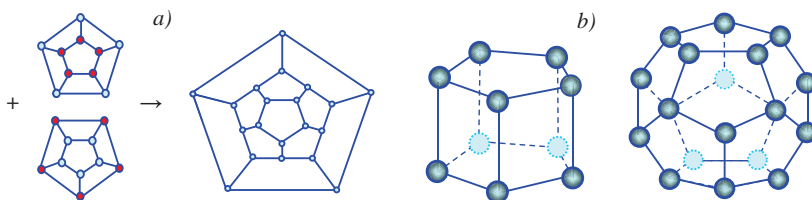


Fig. 14. Fusion of two pentagonal prisms as connection of their graphs (*a)*; *b)* pentagonal prism and five-cornered barrel-shape fullerene (dodecahedron).

Reactions of prism C_{10} with dodecahedron C_{20} $C_{10} + C_{20} \rightarrow (C_{10}C_{20}) \rightarrow C_{30}$ is exhibited in Figure 15 as connection of graphs, together with a fullerene formed. The final graph was designed earlier [4] on different geometrical grounds, but the fullerene structure was not given. Similar to the previous case, this carbon cluster is not only a fullerene, but an opened-end mini-nanotube as well. This nanotube is able to growing by adding carbon pentagonal prisms to both ends. The corresponding reactions can be written as follows

$$C_{10} + C_{30} \rightarrow C_{40}, \quad C_{10} + C_{40} \rightarrow C_{50}, \quad \dots, \quad C_{10} + C_N \rightarrow C_{N+10}, \quad N = 20 + 10n, \quad n = 1, 2, \dots$$

It is worth noting that such nanotube with $n=6$, $N=80$ was also studied in [76].

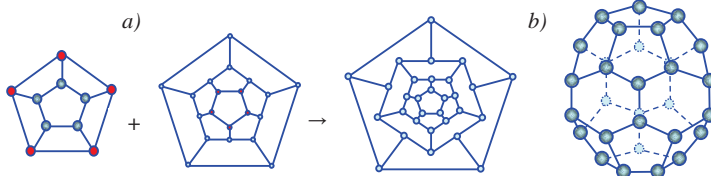


Fig. 15. Connection of graphs: *a)* separate graphs of a pentagonal prism and a five-cornered barrel-shape fullerene, as well as their connection; *b)* fullerene C_{30} obtained.

6. Reactions of hexagonal prism C_{12}

Reaction between two hexagonal prisms is written as $C_{12} + C_{12} \rightarrow (C_{12}C_{12}) \rightarrow C_{24}$ and is shown both as a graph connection and as an initial and a final geometric body in Figure 16.

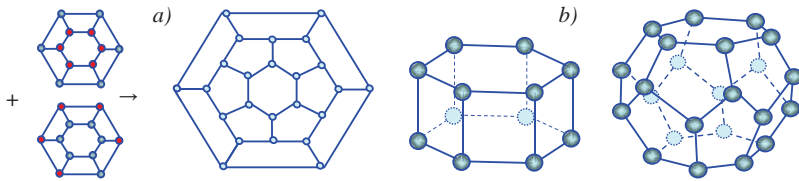


Fig. 16. Fusion of two hexagonal prisms as connection of their graphs (*a*); *b*) hexagonal prism and six-cornered barrel-shape fullerene C_{24} .

Reactions of prism C_{12} with barrel fullerene C_{24} $C_{12} + C_{24} \rightarrow (C_{12}C_{24}) \rightarrow C_{36}$ is presented in Figure 17 as connection of graphs, together with a fullerene formed. The final graph was designed earlier [4] on different geometrical grounds, but the fullerene structure was not given. Similar to the previous case one can consider this carbon cluster not only as a fullerene, but an opened-end mini-nanotube as well. This nanotube is able to growing by adding carbon cubes to both ends. The corresponding reactions are as follows

$$C_{12} + C_{36} \rightarrow C_{48}, \quad C_{12} + C_{48} \rightarrow C_{60}, \quad \dots, \quad C_{12} + C_N \rightarrow C_{N+12}, \quad N = 24 + 12n, \quad n = 1, 2, \dots$$

It is worth noting that such nanotube with $n=6$, $N=96$ was also studied in [76].

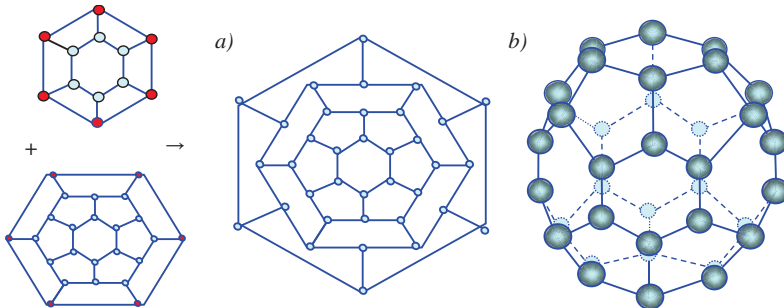


Fig. 17. Connection of graphs: *a*) separate graphs corresponding to a hexagonal prism (above) and a six-cornered barrel-shape fullerene (below), as well as their connection with physical restrictions; *b*) fullerene C_{36} obtained.

7. Conclusion

We have considered reactions of elementary fullerenes (from C_4 to C_{12}) with each other as well as with their heirs. Under the elementary fullerenes we understand a tetrahedron, a cube, and triangular, pentagonal and hexagonal prisms. The process is similar to fusion of bubbles in a soap solution. The graphs describing the process are suggested. The reaction zone is a vertex-connected subgraph that takes into account physical restrictions, namely that covalent bonds exist only between nearest-neighbor atoms. We supposed that during the reactions new covalent bonds are formed and old covalent bonds between the reacting atoms are destroyed. In doing

so we obtained the carbon clusters that refer to fullerenes and nanotubes. It was found that elementary fullerenes can transform either into larger fullerenes or into nanotubes reacting with similar fullerenes of the same symmetry and their successors.

References

- [1] H.W. Kroto, J.R. Heath, S.C. O'Brien, R.F. Curl, R.E. Smalley, C₆₀: Buckminsterfullerene // *Nature* **318** (1985) 162.
- [2] H.W. Kroto, The stability of the fullerenes C_n, with n=24, 28, 32, 36, 60, 60 and 70 // *Nature* **329** (1987) 529.
- [3] S. Iijima, Helical microtubules of graphitic carbon // *Nature* **354** (1991) 56.
- [4] K.S. Novoselov, A.K. Geim, S.V. Morozov, D. Jiang, Y. Zhang, S.V. Dubonos, I.V. Grigorieva, A.A. Firsov, Electrical field effect in atomically thin carbon films // *Science* **306** (2004) 666.
- [5] K.S. Novoselov, A.K. Geim, S.V. Morozov, D. Jiang, M.I. Katsnelson, I.V. Grigorieva, S.V. Dubonos, A.A. Firsov, Two-dimensional gas of massless Dirac fermions in graphene // *Nature* **438** (2005) 197.
- [6] *Nanostructured Carbon for Advanced Applications*, edited by G. Benedek, P. Milani and V.G. Ralchenko (Kluwer Academic Publishers, Dordrecht, 2001) NATO Science Series II. Mathematics, Physics and Chemistry. Vol. 24.
- [7] *Perspectives of Fullerene Nanotechnology*, edited by Eiji Ōsawa (Kluwer Academic Publishers, Dordrecht, 2002).
- [8] *Carbon Nanotubes*, edited by Valentin N. Popov and Philippe Lambin (Springer, Dordrecht, 2006) NATO Science Series II. Mathematics, Physics and Chemistry. Vol. 222.
- [9] *Contemporary Concepts of Condensed Matter Science*, Series Editors E. Burstein, M.L. Cohen, D.L. Mills and P.J. Stiles. *Carbon Nanotubes: Quantum Cylinders of Graphene*, Volume Editors S. Saito and A. Zettl (Elsevier, Amsterdam, 2008).
- [10] *Handbook of Nanophysics. Clusters and Fullerenes*, edited by Klaus D. Sattler (CRC Press, Taylor and Francis Group, LLC, 2010).
- [11] *Graphene. Synthesis and Applications*, edited by Wongbong Choi and Jo-won Lee (CRC Press, Taylor and Francis Group, LLC, 2012).
- [12] B.S. Murty, P. Shankar, Badlev Raj, B.B. Rath, James Murday, *Textbook of Nanoscience and Nanotechnology* (Springer University Press, India, 2013).
- [13] *Springer Handbook of Nanomaterials*, edited by Robert Vajtai (Springer-Verlag, Berlin, 2013).
- [14] *Carbon Nanomaterials*, Second Edition, edited by Yuri Gogotsi and Volker Presser (CRC Press, Taylor and Francis Group, LLC, 2014).
- [15] Debaprasad Das, Hafizu Rahaman, *Carbon Nanotubes and Graphene Nanoribbon Interconnects* (CRC Press, Taylor and Francis Group, LLC, 2015).
- [16] *Carbon Nanomaterials Sourcebook*, Vol. 1. *Graphene, Fullerenes, Nanotubes, and Nanodiamonds*, edited by Klaus D. Sattler (CRC Press, Taylor and Francis Group, LLC, 2016).
- [17] *Structure and Multiscale Mechanics of Carbon Nanomaterials*, edited by Oscar Paris, CISM International Centre for Mechanical Sciences 563 (Springer, Wien, CISM, Udine, 2016).
- [18] C. Piskoti, J. Yarger, A. Zettl, C₃₆, a new carbon solid // *Nature* **393** (1998) 771.
- [19] H. Prinzbach, A. Weiler, P. Landenberger, F. Wahl, J. Wörth, L.T. Scott, M. Gelmont, D. Olevano, B.V. Issendorf, Gas-phase production and photoelectron spectroscopy of the smallest fullerene C₂₀ // *Nature* **407** (2000).
- [20] D.E. Manolopoulos, J.C. May, and S.E. Down, Theoretical studies of the fullerenes: C₃₄ to C₇₀ // *Chem. Phys. Lett.* **181** (1991) 105.

- [21] T. Guo, M.D. Diener, Y. Chai, A.J. Alford, R.E. Haufler, S.M. McClure, T. Ohno, J.H. Weaver, G.E. Scuseria, R.E. Smalley, Uranium stabilization of C₂₈ – a tetravalent fullerene // *Science* **257** (1992) 1661.
- [22] B.L. Zhang, C.Z. Wang, K.M. Ho, C.H. Xu, and C.T. Chan, The geometry of small fullerene cages: C₂₀ to C₇₀ // *J. Chem. Phys.* **97** (1992) 5007.
- [23] B.L. Zhang, C.H. Xu, C.Z. Wang, C.T. Chan, and K.M. Ho, Systematic study of structures and stabilities of fullerenes // *Phys. Rev. B* **46** (1992) 11.
- [24] J.C. Grossman, M. Cote, S.G. Louie, M.L. Cohen, Electronic and structural properties of molecular C₃₆ // *Chem. Phys. Lett.* **284** (1998) 344.
- [25] M.N. Jagadeesh, J. Chandrasekhar, Computational studies on C₃₆ and its dimer // *Chem. Phys. Lett.* **305** (1999) 298.
- [26] A. Ito, T. Monobe, T. Yoshii, K. Tanaka, Electronic structures of C₃₆ fulleride anions: C₃₆⁻ and C₃₆²⁻ // *Chem. Phys. Lett.* **315** (1999) 348.
- [27] A.I. Melker, S.N. Romanov, D.A. Kornilov, Computer simulation of formation of carbon fullerenes // *Materials Phys. Mech.* **2** (2000) 42.
- [28] N. Breda, R.A. Broglia, G. Colo, G. Onida, D. Provasi, E. Vigezzi, C₂₈: a possible room temperature organic superconductor // *Phys. Rev. B* **62** (2000) 130.
- [29] Z. Chen, H. Jiao, M. Bühl, A. Hirsch, W. Thiel, Theoretical investigation into structures and magnetic properties of smaller fullerenes and their heteroanalogues // *Theor. Chem. Acc.* **106** (2001) 352.
- [30] D.A. Kornilov, A.I. Melker, S.N. Romanov, New molecular dynamics predicts fullerene formation // *Proc. SPIE* **4348** (2001) 146.
- [31] B. Paulus, Electronic and structural properties of the cage-like molecules C₂₀ to C₃₆ // *Phys. Chem. Chem. Phys.* **5** (2003) 3364.
- [32] Z.X. Zhang, Z.Y. Pan, Y.X. Li, Q. Wei, Simulations of the nanomechanical properties of compressed small fullerenes // *Modern Phys. Lett. B.* **17** (2003) 877.
- [33] S.Y. Xie, F. Gao, X. Lu, R.B. Huang, C.R. Wang, X. Zhang, M.L. Liu, S.L. Deng, L.S. Zheng, Capturing the labile fullerene C₅₀ as C₅₀Cl₁₀ // *Science* **304** (2004) 699.
- [34] A.I. Melker, Fullerenes and nanotubes: molecular dynamics study // *Proc. SPIE* **5400** (2004) 54.
- [35] J. Pattanayak, T. Kar, S. Scheiner, Substitution patterns in mono BN-fullerenes: C_n (n = 20, 24, 28, 32, 36 and 40) // *J. Phys. Chem. A* **108** (2004) 7681.
- [36] G. Sun, M.C. Nicklaus, R. Xie, Structure, stability, and NMR properties of lower fullerenes C₃₈-C₅₀ and azafullerene C₄₄N₆ // *J. Phys. Chem. A* **109** (2005) 4617.
- [37] X. Lu, Z. Chen, Curved pi-conjugation, aromaticity, and the related chemistry of small fullerenes (<C₆₀) and single-walled carbon nanotubes // *Chem. Rev.* **105** (2005) 3643.
- [38] J. Song, M. Vaziri, A study on electronic and structural properties of C₂₈ and C₁₆N₁₂ // *Mol. Phys.* **104** (2006) 319.
- [40] H.S. Kang, A theoretical study of fullerene-ferrocene hybrids // *J. Phys. Chem. A* **110** (2006) 4780.
- [41] S.D. Khan, S. Ahmad, Modelling of C₂ addition route to the formation of C₆₀ // *Nanotechnology* **17** (2006) 18.
- [42] A.I. Melker, Fifth anniversary of molecular dynamics // *Proc. SPAS jointly with UWM* **10** (2006) 56.
- [43] E. Malolepsza, H.A. Witek, S. Irlé, Comparison of geometric, electronic, and vibrational fullerenes C₂₀-C₃₆ // *J. Phys. Chem. A* **111** (2007) 6649.
- [44] N. Shao, Y. Gao, X.C. Zeng, Search for lowest-energy fullerenes 2: C₃₈ to C₈₀ and C₁₁₂ to C₁₂₀ // *J. Phys. Chem. C* **111** (2007) 17671.
- [45] A.I. Melker, Fifth anniversary of molecular dynamics // *Proc. SPIE* **6597** (2007) 659702-1.

- [46] A.J.C. Varandas, An ab initial study of the interaction between He and C₃₆ with extrapolation to the one electron basis set limit // *Chem. Phys. Lett.* **463** (2008) 225.
- [47] L. Shi, B. Chen, J. Zhou, T. Zhang, Q. Kang, M. Chen, Structure and relative stability of drum-like C_{4n}N_{2n} (n = 3-8) cages and their hydrogenated product C_{4n}H_{4n}N_{2n} (n = 3-8) cage // *Phys. Chem. A* **112** (2008) 11724.
- [48] E. Malolepsza, Y. Lee, H.A. Wittek, S. Irle, C. Lin, H. Hsieh, Comparison of geometric, electronic, and vibrational properties for all pentagon/hexagon-bearing isomers of fullerenes C₃₈, C₄₀, and C₄₂ // *Int. J. Quantum Chem.* **109** (2009) 1999.
- [49] L.-H. Gan, J. Liu, Q. Hui, S.-Q. Shao, Z.-H. Liu, General geometrical rule for stability of carbon polyhedral // *Chem. Phys. Lett.* **472** (2009) 224.
- [50] Y.-M. Chen, J. Shi, L. Rui, Q.-X. Guo, Theoretical study on C₃₂ fullerenes and their endohedral complexes with noble gas atoms // *J. Mol. Struct. THEOCHEM* **907** (2009) 104.
- [51] D. Holec, M.A. Hartmann, F.D. Fischer, F.G. Rammerstorfer, P.H. Mayrhofer, O. Paris, Curvature-induced excess surface energy of fullerenes: density functional theory and Monte Carlo simulations // *Phys. Rev. B* **81** (2010) 235403.
- [52] F. Lin, E.S. Sørensen, C. Kallin, A.J. Berlinsky, C₂₀, the smallest fullerene. In: *Handbook of Nanophysics. Clusters and Fullerenes*, edited by Klaus D. Sattler, (CRC Press, Taylor and Francis Group, LLC, 2010) p. 29-1.
- [53] J. An, L.-H. Gan, J.-Q. Zhao, A global search for the lowest energy isomer of C₂₆ // *J. Chem. Phys.* **132** (2010) 154304.
- [54] F. Naderi, S. Rostamian, B. Naderi, A study on the electronic and structural properties of fullerene C₃₆ and its interaction with amino acid // *Int. J. Phys. Sci.* **7** (2012) 2006.
- [55] A.I. Melker, V. Lonch, Atomic and electronic structure of mini-fullerenes: from four to twenty // *Materials Phys. Mech.* **13** (2012) 22.
- [56] P.W. Dunk, N.K. Kaiser, C.L. Hendrickson, J.P. Quin, S.P. Ewels, Y. Nakanishi, S. Sasaki, H. Shinohara, A.G. Marshall, H.W. Kroto, Bottom-up formation of endohedral monometallofullerenes // *Nature Comm.* **352** (2012) 139.
- [57] P.W. Dunk, N.K. Kaiser, M. Mulet-Gas, A. Rodríguez-Fortea, J.M. Poblet, H. Shinohara, C.L. Hendrickson, A.G. Marshall, H.W. Kroto, The smallest stable fullerene, M@C₂₈ (M=Ti, Zr, U): stabilization and growth from carbon vapor // *J. Am. Chem. Soc.* **134** (2012) 9380.
- [58] E.L. Micelotta, A.P. Jones, J. Cami, E. Peeters, The formation of cosmic fullerenes from arophanic clusters // *Astrophys. J.* **761** (2012) 35.
- [59] S.-L. Deng, S.-Y. Xie, R.-B. Huang, L.-S. Zheng, The formation mechanism of fullerene // *Sci. Sinica Chim.* **42** (2012) 1587.
- [60] A. Kharlamov, G. Kharlamova, M. Bondarenko, V. Fomenko, Joint synthesis of small carbon molecules (C₃-C₁₁), quasi-fullerenes (C₄₀, C₄₈, C₅₂) and their hydrides // *Chem. Engng. Sci.* **1** (2013) 32.
- [61] J. Zhang, F.L. Bowels, D.W. Bearden, W.K. Ray, T. Fuhrer, Y. Ye, C. Dixon, K. Harich, R.F. Helm, M.M. Olmstead, A.L. Balch, H.C. Dorn, A missing link in the transformation from asymmetric to symmetric metallofullerene cages implies a top-down fullerene formation mechanism // *Nature Chem.* **5** (2013) 880.
- [62] F. Naderi, A computational study on the smallest exohedrally functionalized fullerenes, C₂₀X₈ (X=H, F, Cl, Br, NH₂, OH and CN) // *Bulgarian Chem. Comm.* **4** (2014) 680.
- [63] F. Pietrucci, W. Andreoni, Fate of a graphene flake; a new rout toward fullerenes disclosed with ab initio simulations // *J. Chem. Theory Comput.* **10** (2014) 913.
- [64] P.W. Dunk, M. Mulet-Gas, Y. Nakanishi, N.K. Kaiser, A. Rodríguez-Fortea, H. Shinohara, J.P. Poblet, A.G. Marshall, H.W. Kroto, Botom-up formation of endohedral metallofullerenes is directed by charge transfer // *Nature Comm.* **5** (2014) 5844.

- [65] J. Zhen, P. Castellanos, D.M. Paardekooper, Laboratory formation of fullerenes from PAHs: top-down interstellar chemistry // *Astrophys. J. Lett.* **797** (2014) L30.
- [66] R. Sure, R. Tonner, P. Schwerdtfeger, A systematic study of rare gas atoms encapsulated in small fullerenes using dispersion corrected density functional theory // *J. Comp. Chem.* **36** (2015) 88.
- [67] P.W. Dunk, H. Niwa, H. Shinohara, A.G. Marshall, H.W. Kroto, Large fullerenes in mass spectra // *Mol. Phys.* **113** (2015) 2359.
- [68] Y. Jin, A. Perera, V.F. Lotrich, R.J. Bartlett, Couple cluster geometries and energies of C₂₀ carbon cluster isomers // *Chem. Phys. Lett.* **629** (2015) 76.
- [69] M. Mulet-Gas, L. Abella, P.W. Dunk, A. Rodrigues-Forteza, H.W. Kroto, J.P. Poblet, Small endohedral metallofullerenes: exploration of the structure and growth mechanism in Ti@C_{2n} (n=26-50) family // *Chem. Sci.* **6** (2015) 675.
- [70] S.D. Bolboacă, L. Jäntschi, Nanoquantitative structure-property relationship modeling on C₄₂ fullerene isomers // *J. Chem.* **2016** (2016) ID 1791756.
- [71] H.W. Kroto, The stability of the fullerenes C_n, with n = 24, 28, 32, 36, 50, 60 and 70 // *Nature* **329** (1987) 529.
- [72] M. Endo, H.W. Kroto, Formation of carbon nanofibers // *J. Phys. Chem.* **96** (1992) 6941.
- [73] R. Kerner, Nucleation and growth of fullerenes // *Comp. Mater. Sci.* **2** (1994) 500.
- [74] R. Kerner, R.H. Bennemann, Theory for the growth of fullerenes // *Fullerene Sci. Tech.* **4** (1996) 1279.
- [75] N.S. Goroff, Mechanism of fullerene formation // *Acc. Chem. Res.* **29** (1996) 77.
- [76] Z. Slanina, X. Zhao, F. Uhlik, Model narrow nanotubes related to C₃₆, C₃₂ and C₂₀: initial computational structural sampling // *Mater. Sci. Engng B* **96** (2002) 164.
- [77] A.I. Melker, D.A. Kornilov, S.N. Romanov, N.A. Izotova, Carbon nanotubes: formation and computer simulations // *Proc. SPIE* **5127** (2003) 76.
- [78] D.A. Kornilov, A.I. Melker, S.N. Romanov, Conformation transitions in fullerenes at non-zero temperatures // *Proc. SPIE* **5127** (2003) 81.
- [79] A.I. Melker, Fullerenes and nanotubes. Molecular dynamics study // *Proc. SPIE* **5400** (2004) 54.
- [80] S. Ahmad, Criteria for the growth of fullerenes and single-walled carbon nanotubes in sooting environments // *Nanotech.* **16** (2005) 1739.
- [81] G. Brinkmann, D. Franceus, P.W. Fowler, J. Graver, Growing fullerenes from seed: growth transformations of fullerene polyhedral // *Chem. Phys. Lett.* **428** (2006) 386.
- [82] Y. Yamaguchi, L. Colombo, Growth of sp-sp² nanostructures in a carbon plasma // *Phys. Rev. B.* **76** (2007) 134119.
- [83] A.I. Melker, Fiftieth anniversary of molecular dynamics // *Proc. SPIE* **6597** (2007) 02.
- [84] J.E. Bunder, J.M. Hill, Diffusive growth of fullerenes and carbon nanotubes // *J. Chem. Phys.* **131** (2009) 244703.
- [85] A. Chuvilin, U. Kaiser, E. Bichoutskaia, N.A. Besley, A.N. Khlobystov. Direct transformation of grapheme to fullerene // *Nature Chem.* **2** (2010) 450.
- [86] V. Gupta, Graphene as intermediate phase in fullerene and carbon nanotube growth: a Young-Laplace surface-tension model // *Appl. Phys. Lett.* **97** (2010) 181910.
- [87] S. Irle, A. J. Page, B. Saha, Y. Wang, K.R.S. Chandrakumar, Y. Nishimoto, H-J. Qian, K. Morokuma, Atomistic mechanisms of carbon nanostructure self-assembly as predicted by nonequilibrium QM/MD simulations. In: *Practical Aspects of Computational Chemistry II: An Overview of the Last Two Decades and Current Trends*, eds. J. Leszczynski and M.K. Shukla (Springer-European Academy of Sciences, 2012).
- [88] P.W. Dunk, N.K. Kaiser, C.L. Hendrickson, J.P. Quinn, C.P. Eweis, Y. Nakanishi, H. Shinohara, A.G. Marshall, H.W. Kroto, Closed network growth of fullerenes // *Nature Com.* **3** (2012). doi: 10.1038/ncomms1853.

- [89] J. Fujita, M. Tachi, K. Murakami, H. Sakurai, Y. Morita, S. Higashibayashi, M. Takeguchi, Beam-induced graphitic carbon cage transformation from sumanene aggregates // *Appl. Phys. Lett.* **104** (2014) 043107.
- [90] N.A. Poklonski, S.V. Ratkevich, S.A. Vyrko, Quantum-chemical calculation of carbidodecahedron formation in carbon plasma // *J. Phys. Chem. A* **119** (2015) 9133.
- [91] A.I. Melker, M.A. Krupina, Geometric modeling of midi-fullerenes growth from C_{24} to C_{48} // *St. Petersburg State Polytechnical University Journal. Physics and Mathematics* **3(248)** (2016) 52.
- [92] A.I. Melker, T.V. Vorobyeva, Fusion reactions of cupola half-fullerenes // *St. Petersburg State Polytechnical University Journal. Physics and Mathematics* **3(248)** (2016) 59.
- [93] T. Hiraro, H. Sakurai, First and practical synthesis of sumanene, a C_{3v} symmetric partial structure of fullerene // *Ann. Report Osaka Univ.* **5** (2004) 27.
- [94] J.E. Graver, Y.A. Monachino, Highly symmetric fullerenes and nanotubes. In: *Symmetry: Culture and Science. Special issue: Symmetry in Nanostructure*, edited by Mircea Duidea (2008) Vol. 19, pp.317-340.
- [95] A.I. Melker, Possible ways of forming mini-fullerenes and their graphs // *Materials Phys. Mech.* **20** (2014) 1.
- [96] A.I. Melker, S.A. Starovoitov, T.V. Vorobyeva, Classification of mini-fullerenes on graph basis // *Materials Phys. Mech.* **20** (2014) 12.
- [97] A.I. Melker, M.A. Krupina, Designing mini-fullerenes and their relatives on graph basis // *Materials Phys. Mech.* **20** (2014) 18.
- [98] M.A. Krupina, A.I. Melker, S.A. Starovoitov, T.V. Vorobyeva, Structure and graphs of midi-fullerenes // *Proceedings of NDTCS' 2015* **16** (2015) 23.
- [99] K. Xia, X. Feng, Y. Tong, G.W. Wei, Persistent homology for the quantitative prediction of fullerene stability // *J. Comput. Chem.* **36** (2015) 408.
- [100] P. Schwerdtfeger, L. N. Wirz, J. Avery, The topology of fullerenes // *WIREs Comput. Mol. Sci.* **5** (2015) 96. doi: 10.1002/wcms.1207
- [101] D. Nicodemos, M. Stehlik, Fullerene graphs of small diameter, *arXiv:1604.01934v1 [math.CO]* 7 Apr 2016.
- [102] A.I. Melker, *Dynamics of Condensed Matter, Vol. 1, Vibrations and Waves* (St. Petersburg Academy of Sciences on Strength Problems, 2013)
- [103] A.I. Melker, T.V. Vorobyeva, R.M. Zarafutdinov, Structure and energy of $\Delta n=6$ series fullerenes // *Proceedings of NDTCS- 2017* **17** (2017) 75.
- [104] A.I. Melker, M.A. Krupina, R.M. Zarafutdinov, Structure of $\Delta n=10$ series fullerenes // *Proceedings of NDTCS-2017* **17** (2017) 68.
- [105] A.I. Melker, M.A. Krupina, R.M. Zarafutdinov, Periodic system for perfect fullerenes obtained by fusion reactions // *Proceedings of NDTCS-2017* **17** (2017) 72.
- [106] A.I. Melker, T.V. Vorobyeva, R.M. Zarafutdinov, Structure and energy of $\Delta n=14$ series fullerenes // *Proceedings of NDTCS- 2017* **17** (2017) 79.
- [107] A.I. Melker, On the nature of void swelling // *Proc. SPIE* **7377** (2008) 737710-1.
- [108] F. Harary, *Graph Theory* (Addison-Wesley Publishing Co. Reading, 1969)

MODELING GROWTH OF MIDI-FULLERENES FROM C₂₀ TO C₆₀

Alexander I. Melker^{1*} and Maria A. Krupina²

¹Department of Mechanics and Control Processes,

²Department of Experimental Physics,

Peter the Great St. Petersburg Polytechnic University, Polytekhnicheskaya 29,

195251, St. Petersburg, Russia

*e-mail: newton@imop.spbstu.ru

Abstract. Axonometric projections together with corresponding graphs for the first branch of the family of tetra-hexa-cell equator fullerenes including some isomers are constructed in the range from 20 to 60. Some of graphs were obtained earlier but the majority is given for the first time. A unified approach for drawing axonometric projections of these fullerenes is used; namely, it is the dimetric representation which symmetry coincides with that of a corresponding graph. The growth of fullerenes is studied on the basis of two mechanisms, according to which a carbon dimer embeds either in a hexagon or a pentagon of an initial fullerene. This leads to stretching and breaking the covalent bonds which are parallel to arising tensile forces. In both cases there arises a new atomic configuration and there is mass increase of two carbon atoms. We considered direct descendants of the first branch of the tetra-hexa-cell equator family beginning with C₂₀; namely C₂₂, C₂₄, C₂₆, C₂₈, C₃₀, C₃₂, C₃₄, C₃₆, C₃₈, C₄₀, C₄₂, C₄₄, C₄₆, C₄₈, C₅₀, C₅₂, C₅₄, C₅₆, C₅₈, and C₆₀.

Keywords: carbon dimer, fullerene, graph, structure.

1. Introduction

In Ref. [1] we considered the following problem; namely; how to design new fullerenes and their graphs, if one knows a basic elementary graph of a mini-fullerene playing the role of progenitor. We have developed a way of designing different families of fullerenes using this approach. As a result, we have found the family of cupola half-fullerenes: C₁₀, C₁₂, C₁₆, C₂₀, C₂₄; the family of bi-polyfoils: C₁₄, C₁₈, C₂₄, C₃₀, C₃₆; the family of truncated bipyramids: C₁₄, C₁₈, C₂₄, C₃₀, C₃₆; and the family of tetra-hexa-cell equator fullerenes: C₂₀, C₂₄, C₃₂, C₄₀, and C₄₈. All the families contain five members and have a layer structure. Our classification gives not only fullerene symmetry, and so determines the fullerene uniquely, but also connects it with its relatives.

In addition to the graphs, we have given axonometric views of the first members of each family. Similar to many researchers, at that time we used different axonometric projections for presenting fullerene structure. It is justified for small fullerenes, which structure is rather simple, but if one tries to find common structural elements of large fullerenes, one needs use a unified approach. Drawing an axonometric view of any fullerene is a rather tedious procedure, and at that moment the story was not complete.

In Ref. [2] we have suggested a unified approach for drawing axonometric projections of both small and large fullerenes, and we have constructed the axonometric projections and corresponding graphs for the fullerenes in the range from 20 to 36 together with some their isomers. In the long run we came to conclusion that the best way is dimetric axonometry, more properly the dimetric representation which symmetry coincides with that of a

corresponding graph. It should be emphasized that the axonometric projections and graphs were constructed not only for the members of the families of bi-polyfoils and truncated bipyramids mentioned above, but also for ‘intermediate’ members, namely for C₂₂, C₂₆, C₂₈, C₃₂, C₃₄. In doing so, we have exhaustively investigated a dimer mechanism of growing fullerenes. According to it, a carbon dimer embeds either into a hexagon or a pentagon of an initial fullerene. This leads to stretching and breaking the covalent bonds which are parallel to arising tensile forces. In the first case instead of the hexagon adjoining two pentagons, when the dimer embeds in this hexagon, one obtains two adjacent pentagons adjoining two hexagons. In the second case, when the dimer embeds in the pentagon, one obtains two pentagons separated by a rectangle. In both cases there arises a new atomic configuration and there is mass increase of two carbon atoms. This process can continue until a new stable configuration is reached.

In this contribution we consider direct descendents of the first branch of the family of tetra-hexa-cell equator fullerenes beginning with C₂₀; namely C₂₂, C₂₄, C₂₆, C₂₈, C₃₀, C₃₂, C₃₄, C₃₆, C₃₈, C₄₀, C₄₂, C₄₄, C₄₆, C₄₈, C₅₀, C₅₂, C₅₄, C₅₆, C₅₈, and C₆₀. Our aim is to model their growth obtaining at first their graphs, what is simpler, and then constructing their structure on the basis of the graphs obtained.

2. (Tetra-hexa)₃-penta₆ polyhedral fullerene C₂₀

Its atomic configuration consists of three squares, three hexagons and six pentagons (Fig. 1) so it was named a (tetra-hexa)₃-penta₆ polyhedron [3]. This structure together with its consistent electronic structure was obtained in Ref. [3] on the basis of a new mathematic concept of fullerenes. According to the concept a fullerene is any shape composed of atoms, each atom having three nearest neighbors, which can be inscribed into a spherical, ellipsoidal, or similar surface. But what is more important, it was supposed that not only atoms but also shared electron pairs, forming covalent bonds, were located on one and the same sphere, ellipsoid or similar surface. Thereafter we used two rules formulated by Sidgwick and Powell [4] for simple molecules:

- all the electron pairs of a molecule arrange themselves into a such configuration which ensures their maximal removing from each other;
- geometry of a molecule is dictated by the arrangement of the electron pairs.

Incorporating these rules into our concept, we have developed method for calculating electronic and atomic structure of fullerenes of a broad sense [3]. The most interesting result obtained is discovering structural isomers of some fullerenes.

(Tetra-hexa)₃-penta₆ polyhedral fullerene being a structural isomer of a widely known dodecahedral fullerene is the progenitor of the of tetra-hexa-cell equator family of fullerenes. A possible way of generating this fullerene is suggested in Ref. [5].

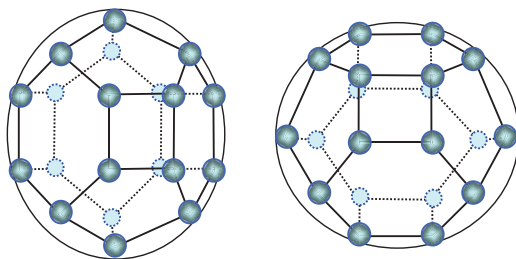


Fig. 1. Atomic structure of a (tetra-hexa)₃-penta₆ polyhedron fullerene, D_{3h} symmetry.

3. Branch of (tetra-hexa)₃-penta₆ polyhedral fullerene C₂₀

First stage. Starting with this fullerene, one can obtain its direct descendants with the help of mechanism of dimer embedding into a hexagon. Drawing the axonometric projections of the fullerenes C₂₂, C₂₄ and C₂₆ is a rather tedious procedure, but it allows avoiding many mistakes in subsequent reasoning. Constructing the graphs of these fullerenes is easier than drawing the axonometric projections. Taking as a basis the structure and graph of fullerene C₂₀, we have obtained the following pictures (Fig. 2). Here fullerenes C₂₀ and C₂₆ are perfect (D_{3h} symmetry), and fullerenes C₂₂ and C₂₄ are imperfect (C_1 symmetry). To gain a better understanding of the mechanism of dimer embedding, its main features are given in the form of schematic representation (Fig. 3).

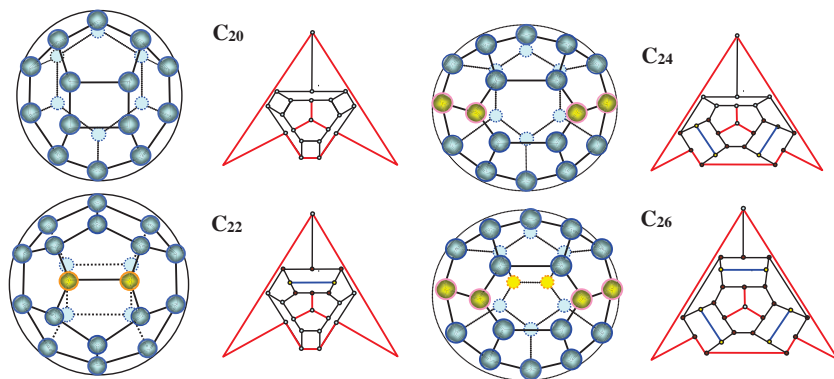


Fig. 2. Atomic structure and graphs of fullerenes C₂₀, C₂₂, C₂₄ and C₂₆.

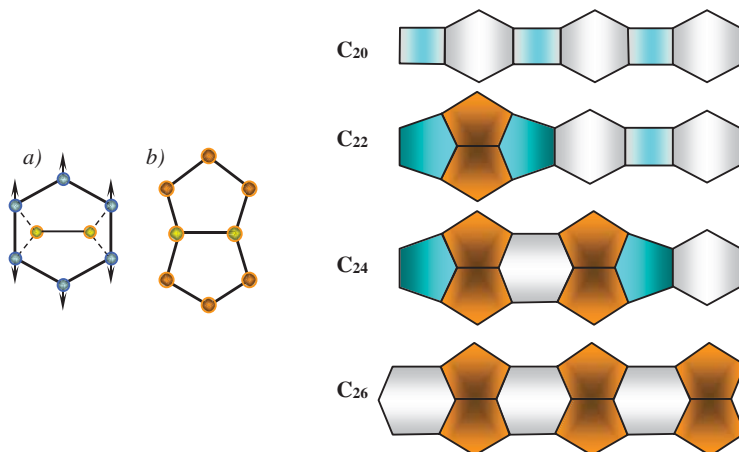


Fig. 3. Scheme reflecting the main local changes during the growth of fullerene C₂₀. Embedding dimer into a hexagon (a) and its transform into two adjacent pentagons (b).

Let us analyze this figure. From the configurations shown it follows that the first embedding which transforms fullerene C₂₀ into fullerene C₂₂, influences deeply only on one of hexagons and two its square neighbors. The hexagon transforms into two adjacent pentagons and its square neighbors become pentagons. As a result, one obtains a cluster which contains four pentagons. The fullerene C₂₂ as a whole is identical to the fullerene obtained from a dodecahedron by imbedding a dimer into a pentagon (Fig. 11 in Ref. [2]). The second imbedding transforms fullerene C₂₂ into fullerene C₂₄. Similar to the previous case, one of two remaining hexagons transforms into two adjacent pentagons, its square neighbor into a pentagon, and its pentagon neighbor into a hexagon. As a result, one obtains one more isomer in addition to four considered in Ref. [2]. At last, the third embedding which leads from fullerene C₂₄ to fullerene C₂₆, eliminates a last remaining hexagon and two its neighboring pentagons, but in return creates two adjacent pentagons and two hexagons of another local orientation. The fullerene obtained is an isomer of the fullerene considered in Ref. [2]. It is named a hexa-octa-cell equator fullerene where every two adjacent pentagons have the form of a bow tie.

Second stage. It should be emphasized that fullerene C₂₄ can grow not only by the way shown in Figures 2 and 3. If a carbon dimer embeds into the newly formed hexagon instead of the remaining one, one obtains a new isomer of fullerene C₂₆ presented in Figure 4. Thereafter both isomers grow in an equal way. As before, to gain a better understanding of the mechanism of dimer embedding, its main features are given in the form of schematic representation (Fig. 5). During the further growth each hexagon transforms into a bow tie, so the hexa-octa-cell equator fullerene finally becomes a bow-tie-cell equator fullerene C₃₂ (Fig. 4), each bow tie having two bow-tie neighbors normal to it.

At the same time, in the pole areas there appear clusters composed of three adjacent hexagons, each hexagon having two adjacent pentagons. To gain a better understanding of this structure, coloring of the fullerene structure is changed in such a way that the pole areas atoms are specially marked in Figure 4. At first glance it might appear that such structure can grow as before embedding carbon dimmers. However the first embedding into one of three adjacent hexagons in any pole area does two residuary adjacent hexagons impotent, so there is the possibility of embedding only one dimmer into each pole area. As a result, one obtains four imperfect fullerenes C₂₈, C₃₀, C₃₄ and C₃₆ having C₁ symmetry, and one perfect C₃₂ with D_{3h} symmetry (Fig. 4).

One can consider fullerenes C₂₀, C₂₆ (the isomer shown in Fig. 2), and C₃₂ as perfect fullerenes having a threefold axis of symmetry. The symmetry can be easily discovered looking at their graphs. Other fullerenes, C₂₂, C₂₄, C₂₆ (the isomer shown in Fig. 3), C₂₈, C₃₀, and C₃₄, are imperfect. By analogy with crystal physics it can be said that the reason of imperfection is connected with the fact that the fullerenes have extra 'interstitial' dimmers or 'vacant' dimmers.

At first glance fullerene C₃₆ having two extra interstitial dimmers is imperfect in comparison with fullerene C₃₂. It would be expected also from its graph (Fig. 4). However it must be emphasized that applying graph approach for analysis of fullerene structure, it is necessary not only to use plane graphs but do such plane graphs which show the best correlation with the symmetry of a corresponding polyhedron [6]. Any fullerene atomic structure given in Figures 1–4 is in essence a modified cartographic projection which in addition to a front projection shows also a back projection of the fullerene ellipsoid. Here the main symmetry axis of a fullerene must be in the center of the corresponding fullerene graph normal to its plane. The graph of fullerene C₃₆ shown in Figure 4 was constructed as a simple geometrical continuation of the graph of fullerene C₃₂. From Figure 4, it also follows that in contrast to fullerene C₃₂, fullerene C₃₆ lost rotation symmetry having a three-fold axis, and it made its graph clumsy.

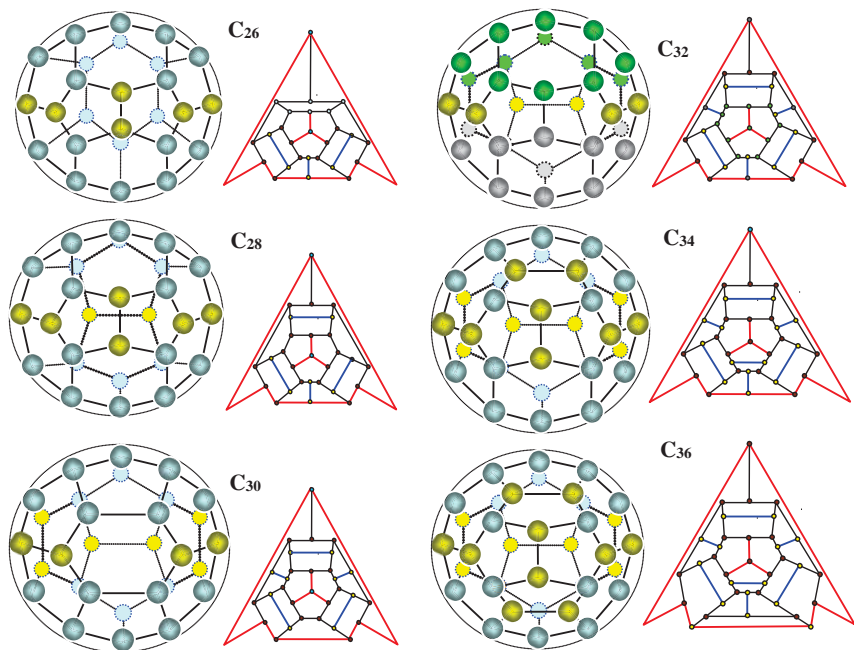


Fig. 4. Atomic structure and graphs of fullerenes C_{26} , C_{28} , C_{30} , C_{32} , C_{34} , and C_{36} .

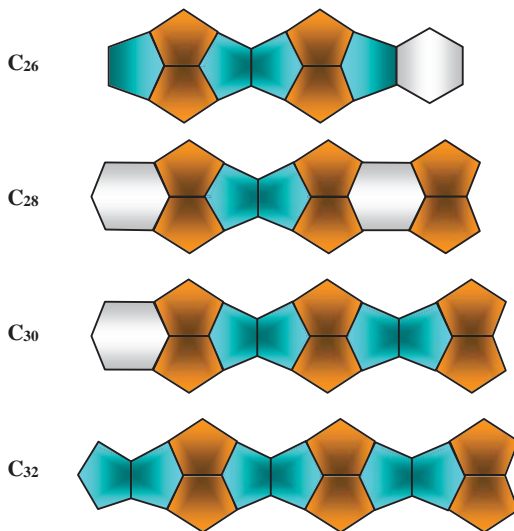


Fig. 5. Scheme reflecting the main structural changes during the growth of fullerene C_{24} .

4. Changing symmetry

The structure of fullerene C₃₆ is rather interesting. It is a dodecahedron which is formed of twelve pentagons and eight hexagons. For study of this fullerene it is convenient to use a new system of coordinates where the axis z , or the main axis of symmetry, passes through the centers of two clusters formed of four pentagons; here nearest three of which being adjacent. In doing so, we have the polar-axis change of 90 degrees conserving the symmetry. The clusters are separated by a zigzag ring of twelve atoms. To gain a better understanding of this structure, the clusters are specially marked in Figure 6. Here one confronts with a quite unexpected phenomenon; the fullerene is changing its symmetry during growth. The graph taking into account a new symmetry of fullerene C₃₆ looks nice (Fig. 6). From this figure it follows that the new symmetry is rotation-reflection symmetry D_{4d} having a fourfold axis. The fullerene is perfect, and we have the group of perfect fullerenes including C₂₀, C₂₆, C₃₂, and C₃₆.

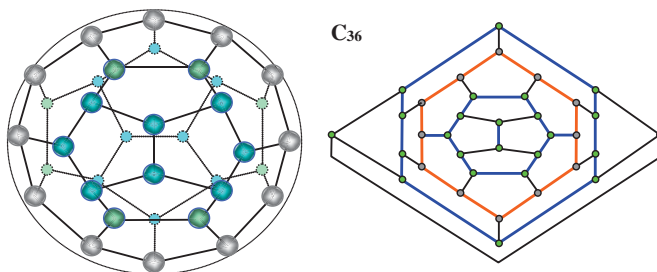


Fig. 6. Two clusters of twelve atoms in fullerene C₃₆; each cluster containing four pentagons, and symmetric graph of its fullerene.

5. Growth in new symmetry

The obtained fullerene C₃₆ is able to grow further. It is felt that the process is going conserving the new symmetry. Moreover, we believe that the dimer embedding takes place in regions of the largest curvature attempting to do the fullerene surface looking like a sphere. The two cells of twelve atoms, each cell having four pentagons, the nearest three of which being adjacent, have the largest curvature. Therefore it is reasonable to suggest that dimer embedding will occur inside these cells. The mechanism of carbon dimer embedding into a pentagon was suggested in Ref. [2]. In our case it looks like it is shown in Figure 7. As a consequence one obtains fullerene C₃₈ which receives the possibility for growing further with the help of Endo-Kroto mechanism, i.e. by embedding carbon dimers in hexagons having two adjacent pentagons or, as in our case, two adjacent polygons, one of which is a pentagon and the other is a rectangle. The process creates fullerenes C₄₀, C₄₂, C₄₄, C₄₆, and C₄₈. (Fig. 8).

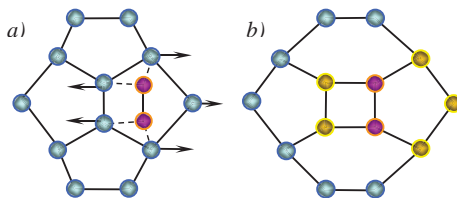


Fig. 7. Carbon dimer embedding into a pentagon (a) and local structural changing (b).

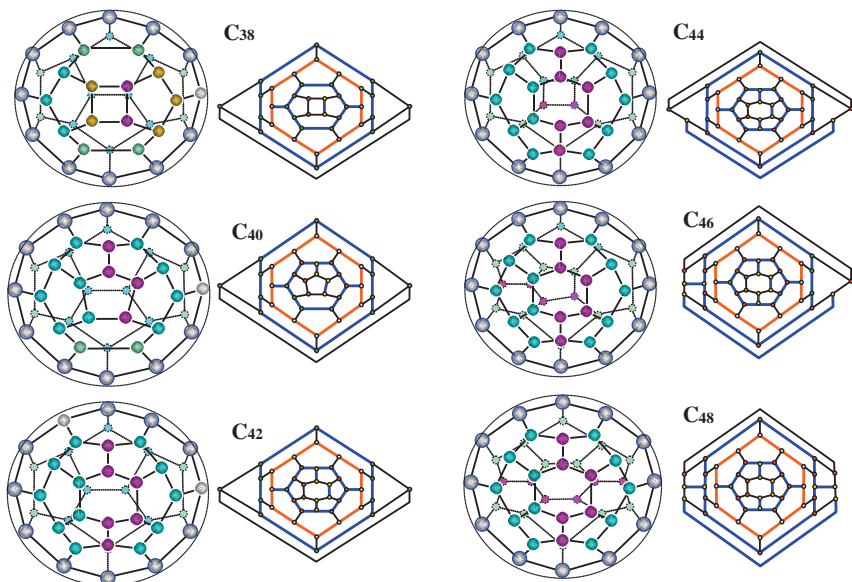


Fig. 8. Atomic structure and graphs of fullerenes C_{38} , C_{40} , C_{42} , C_{44} , C_{46} , and C_{48} .

6. Second changing symmetry and growth in the second new symmetry

Similar to fullerene C_{36} the structure of fullerene C_{48} is also rather interesting. The fullerene contains two clusters of eighteen atoms, each cluster having six pentagons forming a ring around a hexagon in the center. The clusters are separated by a zigzag ring of twelve atoms. To gain a better understanding of this structure, the clusters are specially marked in Figure 9. Here one confronts again with a quite unexpected phenomenon; the fullerene has changed its symmetry again during the growth. From Figure 9 it follows that the new symmetry is rotation-reflection symmetry D_{6d} having a sixfold axis. The fullerene is perfect, and one has the group of perfect fullerenes including C_{20} , C_{26} , C_{32} , C_{36} , and C_{48} , each fullerene having its own symmetry.

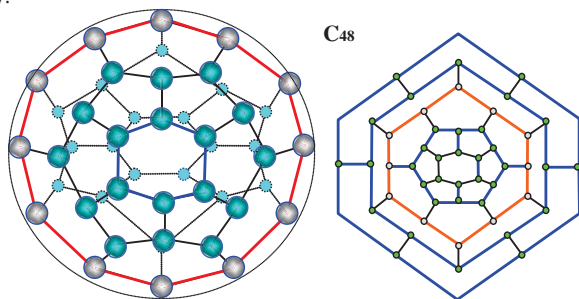


Fig. 9. Two clusters of eighteen atoms in fullerene C_{48} ; each cluster containing six pentagons, and symmetric graph of its fullerene.

Embedding a dimer into a hexagon of any polar area of fullerene C_{48} gives fullerene C_{50} which is a bifurcation point. Thereafter fullerene C_{50} can grow, following various paths. They are shown in Figure 10. In the first case one obtains asymmetric fullerene C_{52} and symmetric fullerene C_{54} ; in the second case symmetric fullerene C_{52} and asymmetric fullerene C_{54} . We suppose that symmetric fullerenes are more stable than asymmetric ones because the latter have a larger curvature. Fullerene C_{56} can be obtained either from symmetric or from asymmetric fullerene C_{54} . In both case the structure is just the same. Further growing creates fullerenes C_{58} and C_{60} (Fig. 11).

It is interesting to compare the structures of fullerenes C_{36} and C_{60} (Fig. 12). Both fullerenes have similar polar areas formed of four pentagons, nearest three of which being adjacent. These clusters are separated by one zigzag ring of twelve atoms in the case of fullerene C_{36} . For fullerene C_{60} there are two such rings; in addition between these rings there is one more zigzag ring of twelve atoms. By analogy with geography we can say that for fullerene C_{36} one has two frigid zones formed of four pentagons and two temperate zones formed of two pentagons and four hexagons. For fullerene C_{60} in addition to those zones there appear two torrid zones formed of six hexagons.

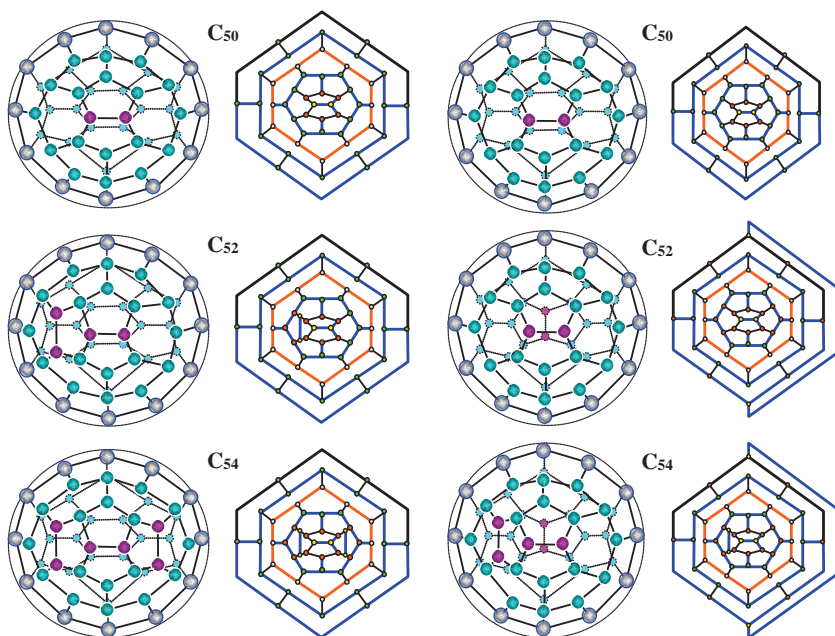


Fig. 10. Atomic structure and graphs of fullerenes C_{50} , C_{52} , and C_{54} ; the first way of growing is on the left, the second way is on the right.

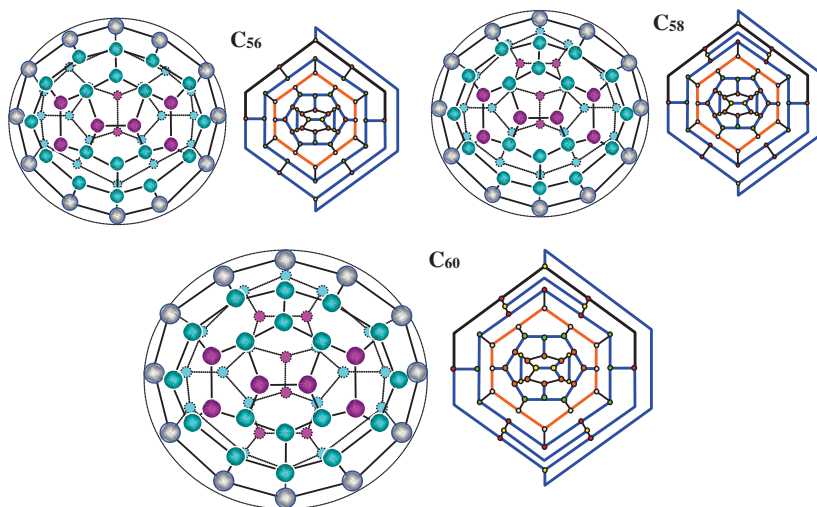


Fig. 11. Atomic structure and graphs of fullerenes C_{56} , C_{58} , and C_{60} .

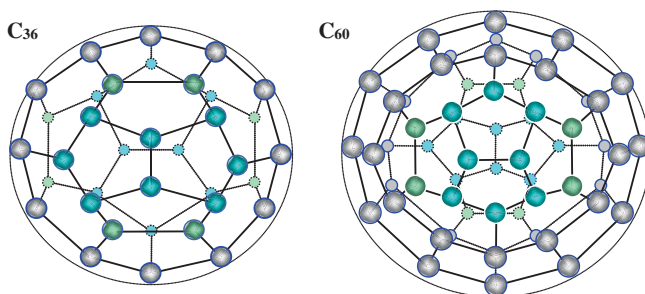


Fig. 12. Collation of atomic structure of fullerenes C_{36} and C_{60} .

7. Conclusion and discussion

Axonometric projections together with corresponding graphs for the first branch of the family of tetra-hexa-cell equator fullerenes including some isomers are constructed in the range from 20 to 60. A unified approach for drawing axonometric projections of these fullerenes is suggested; namely, it is the dimetric representation which symmetry coincides with that of a corresponding graph. The growth of fullerenes is studied on the basis of two mechanisms, according to which a carbon dimer embeds either in a hexagon or a pentagon of an initial fullerene. This leads to stretching and breaking the covalent bonds which are parallel to arising tensile forces. In both cases there arises a new atomic configuration and there is mass increase of two carbon atoms. We considered direct descendents of the first branch of tetra-hexa-cell equator family beginning with C_{20} ; namely C_{22} , C_{24} , C_{26} , C_{28} , C_{30} , C_{32} , C_{34} , C_{36} , C_{38} , C_{40} , C_{42} , C_{44} , C_{46} , C_{48} , C_{50} , C_{52} , C_{54} , C_{56} , C_{58} , and C_{60} .

Fullerenes C₂₀, C₂₆ (the isomer shown in Fig. 2), C₃₂, and C₃₆ are perfect fullerenes having threefold symmetry. The symmetry can be easily discovered looking at their graphs. Fullerenes, C₂₂, C₂₄, C₂₆ (the isomer shown in Fig. 4), C₂₈, C₃₀, and C₃₄ are imperfect. By analogy with crystal physics it can be said that the reason of imperfection is connected with the fact that the fullerenes have extra 'interstitial' dimmers or 'vacant' dimmers. The structure of fullerene C₃₆ is rather interesting. It is a dodecahedron which is formed of twelve pentagons and eight hexagons. For study of this fullerene it is convenient to use the system of coordinates where the axis z , or the main axis of symmetry, passes through the centers of two clusters formed of four pentagons, where nearest three of which being adjacent. In doing so, the polar-axis change is of 90 degrees conserving the symmetry. The clusters are separated by a zigzag ring of twelve atoms (Fig. 6). It must be emphasized that applying graph approach for analysis of fullerene structure, it is necessary not only to use plane graphs but do such plane graphs which show the best correlation with the symmetry of a corresponding polyhedron. A quite unexpected phenomenon was discovered; the fullerene is changing its symmetry during growth. From Figure 6 it follows that the new symmetry is rotation-reflection symmetry having a fourfold axis. The fullerene is perfect, and it must be included in the group of perfect fullerenes. It is notable that among the perfect fullerenes there is one which has a "magic" number 32 [7]. Stability of the magic fullerene C₃₂ can be understood by reference to Figure 6 where its structure is shown.

Similar to fullerene C₃₆ the structure of fullerene C₄₈ is also rather interesting. The fullerene contains two clusters of eighteen atoms, each cluster having six pentagons forming a ring and one hexagon in the center. The clusters are separated by a zigzag ring of twelve atoms. Here one confronts again with a quite unexpected phenomenon; the fullerene is changing its symmetry again during the growth. From Figure 9 it follows that the new symmetry is rotation-reflection symmetry having a sixfold axis. The fullerene is perfect, and therefore the group of perfect fullerenes increases having C₂₀, C₂₆, C₃₂, C₃₆, and C₄₈, each fullerene with its own symmetry. Embedding a dimer into a hexagon of any polar area of fullerene C₅₀ gives fullerene C₅₀ which is a bifurcation point. Thereafter fullerene C₅₀ can grow, following various paths (Fig. 10). In the first case one obtains symmetric fullerene C₅₂ and asymmetric fullerene C₅₄, in the second case asymmetric fullerene C₅₂ and symmetric fullerene C₅₄. We suppose that symmetric fullerenes are more stable than asymmetric ones because the latter have a larger curvature. Fullerene C₅₆ can be obtained either from symmetric or from asymmetric fullerene C₅₄. In both cases the structure is just the same. Further growing creates fullerenes C₅₈ and C₆₀ (Fig. 11).

The structure of fullerenes C₃₆ and C₆₀ has much in common (Fig. 12). Both fullerenes have similar polar areas formed of four pentagons, nearest three of which being adjacent. These clusters are separated by one zigzag ring of twelve atoms in the case of fullerene C₃₆. For fullerene C₆₀ there are two such rings; besides between these rings there is one more zigzag ring of twelve atoms. By analogy with geography one can say that fullerene C₃₆ has two frigid zones formed of four pentagons and two temperate zones formed of two pentagons and four hexagons. For fullerene C₆₀ in addition to those zones there appear two torrid zones formed of six hexagons.

Hidden symmetry and periodicity. We have collated fullerenes C₃₆ and C₆₀ (Fig. 12) and have found that they have similar frigid zones formed of four pentagons. Besides these fullerenes belong to the same symmetry which is rotation-reflection symmetry D_{4d} having a four-fold axis. It was not difficult because the fullerenes were presented in the form of identical axonometric projections. However in many cases fullerenes are shown in different forms. In such a situation, graph analysis is useful. In Ref. [6] it is emphasized that on the basis of graph analysis one can distinguish different families of fullerenes and therefore one

can do some classification of these unusual carbon structures. However graph analysis is able not only to divide but also to unite.

Consider the structure of fullerene C_{48} obtained in this study and fullerene C_{36} designed through the use of fusion algorithm in Refs. [8, 9]. At first glance they have nothing in common (Fig.13). However, comparing their graphs shows that both fullerenes have the six-fold symmetry. It is worth noting that the mass difference between these fullerenes is $\Delta m=12$ being equal to a double degree is suggested [11].

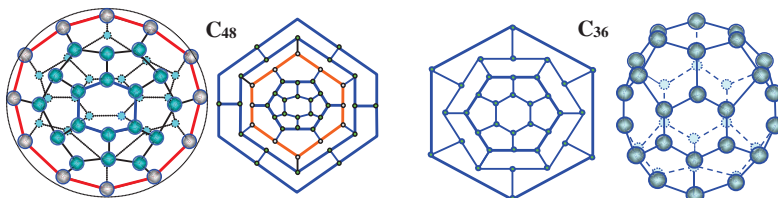


Fig. 13. Collation of atomic structure of fullerenes C_{36} and C_{48} .

References

- [1] A.I. Melker, M.A. Krupina, Designing mini-fullerenes and their relatives on graph basis // *Materials Physics and Mechanics* **20** (2014) 18-24.
- [2] M.A. Krupina, A.I. Melker, S.A. Starovoitov, T.V. Vorobyeva, Structure and graphs of midi-fullerenes // *Proceedings of NDTCS' 2015* **16** (2015) 23-26.
- [3] A.I. Melker, V. Lonch, Atomic and electronic structure of mini-fullerenes: from four to twenty // *Materials Physics and Mechanics* **13** (2012) 22-26.
- [4] N.V. Sidgwick, H.M. Powell, Bakerian Lecture, Stereochemical types and valency groups // *Proc. Roy. Soc. Series A* **176** (1940) 153-180.
- [5] A.I. Melker, Possible ways of forming mini-fullerenes and their graphs // *Materials Physics and Mechanics* **20** (2014) 1-11.
- [6] A.I. Melker, S.A. Starovoitov, T.V. Vorobyeva, Classification of mini-fullerenes on graph basis // *Materials Physics and Mechanics* **20** (2014) 12-17.
- [7] S.V. Kozyrev, V.V. Rotkin, Structure, dynamics of crystalline lattice, electronic structure and properties // *Physics of Solid State* **27** (1993) 1409-1434.
- [8] A.I. Melker, T.V. Vorobyeva, R.M. Zarafutdinov, Structure and energy of $\Delta n=6$ series fullerenes // *Proceedings of NDTCS- 2017* **17** (2017) 75-78.
- [9] A.I. Melker, M.A. Krupina, Unified approach to forming fullerenes and nanotubes // *Materials Physics and Mechanics* (2017). (in print).
- [10] A.I. Melker, M.A. Krupina, Geometric modeling of midi-fullerenes growth from C_{32} to C_{60} // *St. Petersburg State Polytechnical University Journal. Physics and Mathematics* **10(1)** (2017) 47-54.
- [11] A.I. Melker, M.A. Krupina, Geometric modeling of midi-fullerenes growth from C_{40} to C_{68} // *Proceedings of NDTCS- 2017* **17** (2017) 64-68.

MODELING GROWTH OF MIDI-FULLERENES FROM C₄₈ TO C₇₂

Alexander I. Melker^{1*} and Maria A. Krupina²

¹Department of Mechanics and Control Processes,

²Department of Experimental Physics,

Peter the Great St. Petersburg Polytechnic University, Polytekhnicheskaya 29,

195251, St. Petersburg, Russia

*e-mail: newton@imop.spbstu.ru

Abstract. Axonometric projections together with corresponding graphs for tetra-hexa-cell-equator fullerenes are constructed in the range from 48 to 72. A unified approach for drawing axonometric projections of the fullerenes was used. The process of growth of fullerenes is studied on the basis of the mechanism, according to which a carbon dimer embeds in a hexagon of an initial fullerene. As a result, there arises a new atomic configuration and there is mass increase of two carbon atoms. We obtained direct descendents of the fifth branch of tetra-hexa-cell-equator family which begins with C₄₈; namely C₅₀, C₅₂, C₅₄, C₅₆, C₅₈, C₆₀, C₆₂, C₆₄, C₆₆, C₆₈, C₇₀, and C₇₂. Among them only three fullerenes, C₄₈, C₆₀ and C₇₂ are highly symmetric. The symmetry can be easily discovered looking at their graphs. On the basis of this study, as well as previous investigations the periodic system of fullerenes is suggested.

Keywords: carbon dimer, fullerene, graph, modeling, structure.

1. Introduction

Most investigations of fullerenes and nanotubes have centered on either obtaining these materials experimentally or studying properties of the materials which structure was usually postulated. To our mind, the crucial questions for advanced applications of these materials are: how the materials are originated and what structure they obtain.

Up to now mechanism of fullerene- and nanotube-formation is a controversial point. Many different models have been proposed to explain their formation. The known mechanisms can be categorized into two major groups: bottom-up and top-down models. In the first case, fullerene cages and nanotubes are considered to be formed from carbon atoms and small carbon clusters [1-10]. In the second case, fullerenes and nanotubes are thought as direct transformation of graphene into fullerenes or nanotubes [11-17].

We will follow to one of the first-group mechanisms suggested for the first time in [1] because it has better justification [4]. Besides, it allows classify fullerene structures [8]. Briefly, it consists in the following. A carbon dimer embeds into a hexagon of an initial fullerene. As a result, instead of the hexagon adjoining two pentagons, when the dimer embeds into this hexagon, one obtains two adjacent pentagons adjoining two hexagons; there arises a new atomic configuration and there is mass increase of two carbon atoms

In doing so, we geometrically modeled growth of the second branch of the family of tetra-hexa-cell equator fullerenes beginning with C₂₄ [8] in the range from 24 to 48. We have constructed the axonometric projections and the corresponding graphs for these fullerenes.

In this contribution we consider direct descendents of the tetra-hexa-cell-equator family of fullerenes from C₄₈ to C₇₂. Our aim is at first to obtain their graphs, what is simpler, and then to construct the structure of fullerenes on the basis of the graphs obtained.

2. Growth of tetra₆-hexa₂₀ polyhedral fullerene C₄₈

The atomic configuration of this fullerene consists of six squares and twenty hexagons, so it was named a tetra₆-hexa₂₀ polyhedron. Its structure can be composed of two cupola half-fullerenes C₂₄; each of them has in its center a hexagon being surrounded with six hexagons. The cupolas can react with each other [11] creating two isomers of fullerene C₄₈, one of which having D_{6h} symmetry is shown in Figure 1.

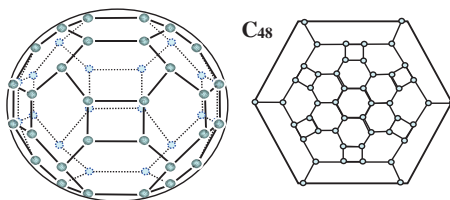


Fig. 1. Atomic structure and graph of a tetra₆-hexa₂₀ polyhedron C₄₈.

First stage. Starting with this fullerene, one can obtain its direct descendants through the use of dimer embedding into a hexagon. We have emphasized in our previous papers that drawing the axonometric projections of fullerenes is a rather tedious procedure, but it allows avoiding many mistakes in subsequent reasoning. Constructing the fullerene graphs is easier than drawing the axonometric projections. Taking as a basis the structure and graph of fullerene C₄₈, we have obtained the fullerenes from C₄₈ to C₆₀ (Fig. 2). To gain a better understanding of the mechanism of dimer embedding, its main features are given in the form of scheme (Fig. 3).

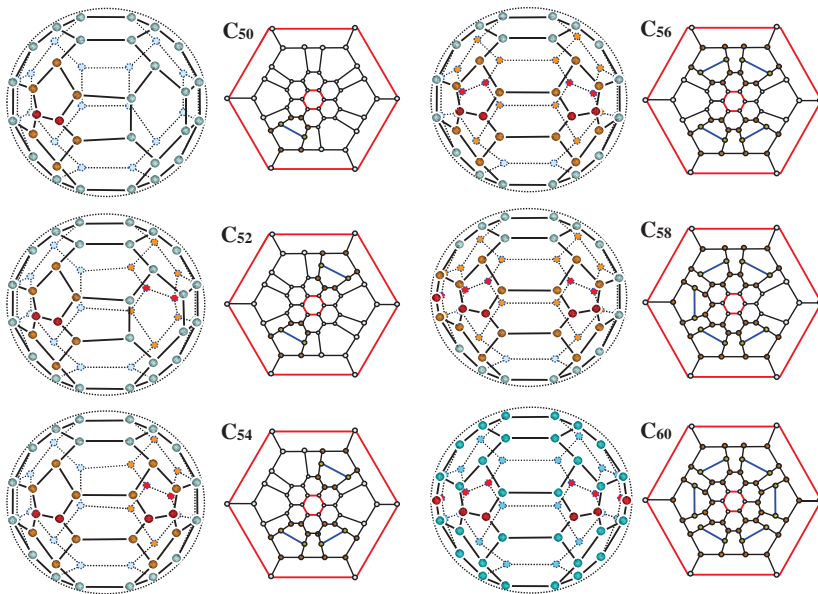


Fig. 2. Atomic structure and graphs of some fullerenes C₅₀, C₅₂, C₅₄, C₅₆, C₅₈, and C₆₀.

Let us analyze these figures. From the configurations shown it follows that the first embedding transforms fullerene C₄₈ into fullerene C₅₀. It influences deeply only on one of hexagons and two its square neighbors. The hexagon transforms into two adjacent pentagons and its square neighbors become pentagons; the whole fullerene losing six-fold symmetry. As a consequence, there arises a cell which contains four pentagons.

The second imbedding transforms fullerene C₅₀ into fullerene C₅₂. It can be done by two ways. As a result one obtains two isomers having different symmetry. Similar to the previous case, in the fullerene having D_{1h} symmetry one of nearest to the cell hexagons transforms into two adjacent pentagons, its square neighbor into a pentagon, and its pentagon neighbor into a hexagon (growth from one nucleus). Other isomer contains two isolated cells of four pentagons (growth from two nuclei).

The third embedding leads to transition from fullerene C₅₂ to fullerene C₅₄. In the case of one-nucleus growth it eliminates one more hexagon and two its neighbors, a pentagon and a square, but in return creates an adjacent hexagon of another local orientation and a new pentagon. It is possible also to obtain several different isomers; one of them having D_{3h} symmetry is shown in Figure 3.

The fourth imbedding transforms fullerene C₅₄ into fullerene C₅₆; two isomers are presented in Figure 3. The fifth embedding changes fullerene C₅₆ into fullerene C₅₈. At last the sixth embedding which leads to fullerene C₆₀ restores the six-fold symmetry. The fullerene C₆₀ obtained could be named hexa-octa-cell-equator fullerene where every two adjacent pentagons have the form of a bow tie (see the scheme at the bottom of Figure 3).

Second stage. Now the fullerene C₆₀ is up against the problem; it can grow only at an angle to its axes of symmetry. It is connected with the fact that embedding can be realized only normal to a direction along which a hexagon has two neighboring mutually antithetic pentagons. During the further growth by dimer embedding, one obtains fullerenes C₆₂, C₆₄, C₆₆, C₆₈, C₇₀, and C₇₂ (Fig. 4). The structure of fullerene C₇₂ is rather interesting. It is formed from six pairs of two adjacent pentagons along the equator separated with six pairs of two adjacent hexagons. To gain a better understanding of this structure, the pentagon pairs are specially marked in Figure 5. The main features of dimer embedding are given in the form of schematic representation in Figure 6. We consider here only the growth from one nucleus. However, similarly to the first stage one can obtain many intermediate fullerenes having different symmetry.

3. Conclusion

Axonometric projections together with corresponding graphs for tetra-hexa-cell-equator fullerenes are constructed in the range from 48 to 72. A unified approach for drawing axonometric projections of the fullerenes was used. It consists in the following; one should use the dimetric representation which symmetry coincides with that of a corresponding graph. The growth of fullerenes is studied on the basis of the mechanism, according to which a carbon dimer embeds in a hexagon of an initial fullerene. This leads to stretching and breaking the covalent bonds which are parallel to arising tensile forces. In this case, instead of the hexagon adjoining two pentagons, one obtains two adjacent pentagons adjoining two hexagons. As a result, there arises a new atomic configuration and there is mass increase of two carbon atoms. We obtained direct descendents of the fifth branch of the tetra-hexa-cell-equator family 6 which begins with C₄₈; namely C₅₀, C₅₂, C₅₄, C₅₆, C₅₈, C₆₀, C₆₂, C₆₄, C₆₆, C₆₈, C₇₀, and C₇₂. Among them only three fullerenes, C₄₈, C₆₀ and C₇₂ are highly symmetric. The symmetry can be easily discovered looking at their graphs.

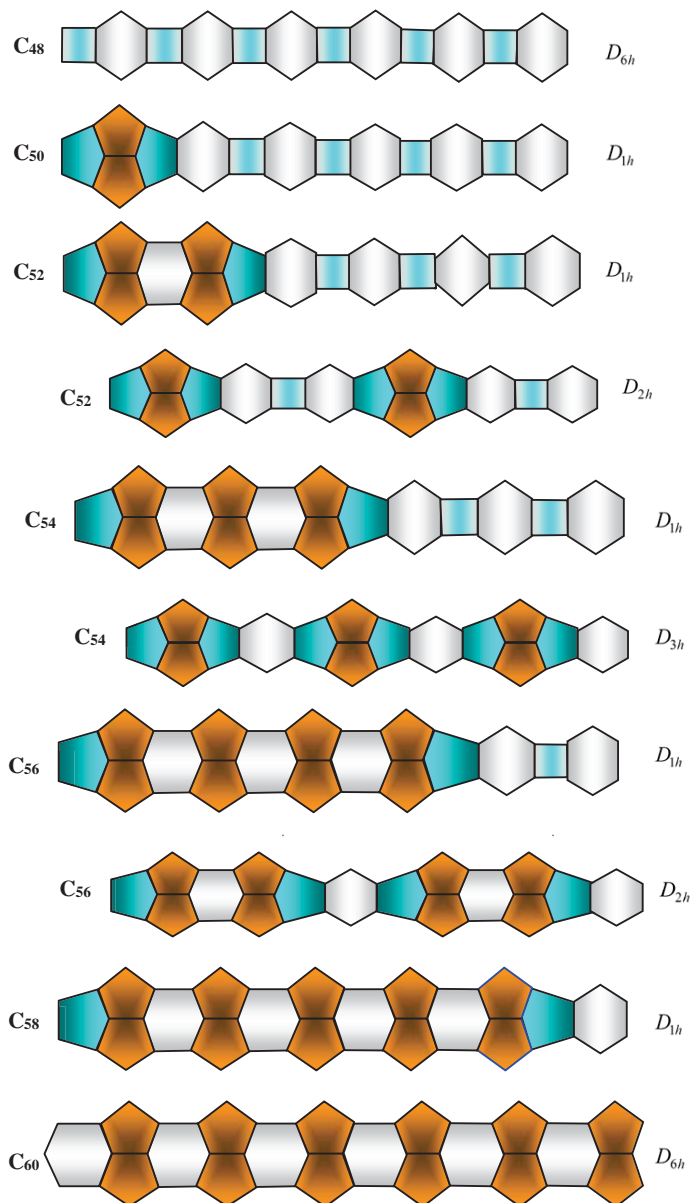


Fig. 3. Scheme reflecting the main structural changes during the growth of fullerene C_{50} .

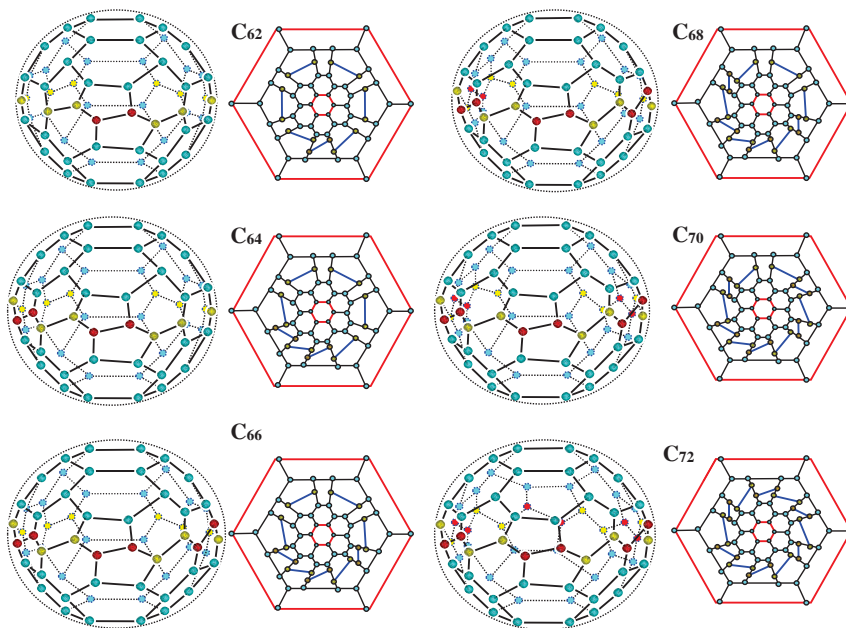


Fig. 4 Atomic structure and graphs of some fullerenes C₆₂, C₆₄, C₆₆, C₆₈, C₇₀, and C₇₂.

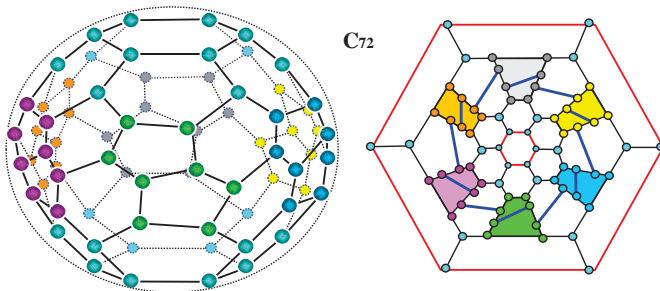


Fig. 5. Six in-pairs-adjacent pentagons in fullerene C₇₂.

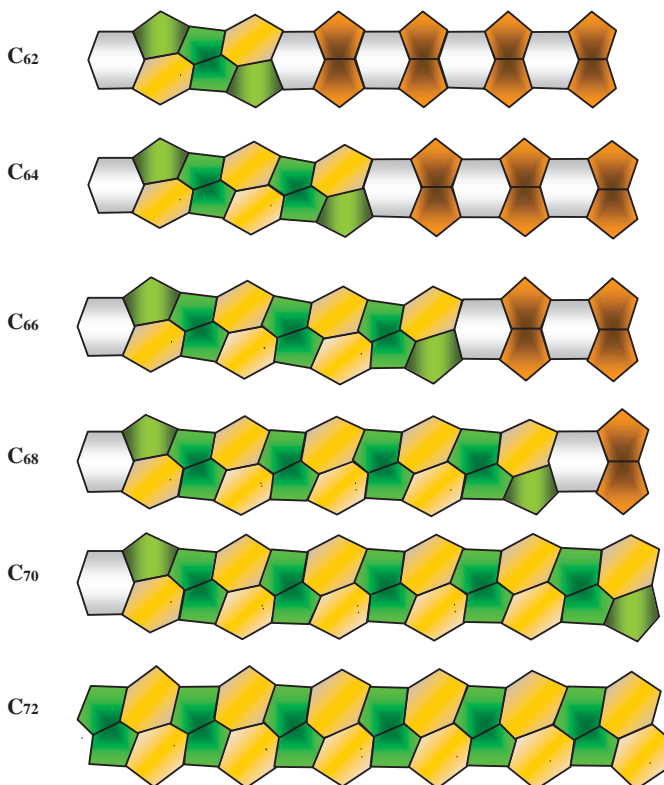


Fig. 6. Scheme reflecting the main structural changes during the growth of fullerene C_{62} .

4. Discussion

In the Introduction, we have set off for fullerenes the crucial questions from the rest ones; namely, how the fullerenes are originated and what structure they obtain naturally. However, the most important and most difficult question for any science is classification [18]. Let us consider what can be done in this regard for fullerenes.

Modeling the growth of fullerenes from C_{24} (D_{3h} symmetry) to C_{48} , we have obtained the perfect fullerenes C_{30} and C_{36} conserving three-fold symmetry [8]. Modeling the growth of fullerenes from C_{32} (D_{4h} symmetry) to C_{60} , we found perfect fullerenes C_{40} and C_{48} conserving four-fold symmetry [9]. Modeling the growth of fullerenes from C_{40} (D_{5h} symmetry) to C_{68} , we found perfect fullerenes C_{50} and C_{60} conserving five-fold symmetry [10]. In this study, starting from fullerene C_{48} (D_{6h} symmetry), we have obtained perfect fullerenes C_{60} and C_{72} . The mass difference between successive fullerenes in the first case is $\Delta m=6$, in the second case $\Delta m=8$, in the third case $\Delta m=10$ and in the fourth case $\Delta m=12$. It should be emphasized that in all the cases the mass difference is equal to a double degree of symmetry. On the basis of these investigations, as well as others, we can submit the following periodic system for embedded fullerenes. It should be mentioned that preliminary sketches of the periodic system are given in Refs. [10, 19].

Periodic System of Fullerenes

Symmetry of Fullerenes				
3-fold S $\Delta m=6$	3-fold T $\Delta m=6$	4-fold $\Delta m=8$	5-fold $\Delta m=10$	6-fold $\Delta m=12$
C₁₄ C ₁₆ C ₂₈	C₁₈ C ₂₀ C ₂₂	C₂₄ C ₂₆ C ₂₈ C ₃₀	C₃₀ C ₃₂ C ₃₄ C ₃₆ C ₃₈	C₃₆ C ₃₈ C ₄₀ C ₄₂ C ₄₄ C ₄₆
C₂₀ C ₂₂ C ₂₄	C₂₄ C ₂₆ C ₂₈	C₃₂ C ₃₄ C ₃₆ C ₃₈	C₄₀ C ₄₂ C ₄₄ C ₄₆ C ₄₈	C₄₈ C ₅₀ C ₅₂ C ₅₄ C ₅₆ C ₅₈
C₂₆ C ₂₈ C ₃₀	C₃₀ C ₃₂ C ₃₄	C₄₀ C ₄₂ C ₄₄ C ₄₆	C₅₀ C ₅₂ C ₅₄ C ₅₆ C ₅₈	C₆₀ C ₆₂ C ₆₄ C ₆₆ C ₆₈ C ₇₀
C₃₂ C ₃₄ C ₃₆	C₃₆ C ₃₈ C ₄₀	C₄₈ C ₅₀ C ₅₂ C ₅₄	C₆₀ C ₆₂ C ₆₄ C ₆₆ C ₆₈	C₇₂ C ₇₄ C ₇₆ C ₇₈ C ₈₀ C ₈₂
C₃₈ C ₄₀ C ₄₂	C₄₂ C ₄₄ C ₄₆	C₅₆ C ₅₈ C ₆₀ C ₆₂	C₇₀ C ₇₂ C ₇₄ C ₇₆ C ₇₈	C₈₄ C ₈₆ C ₈₈ C ₉₀ C ₉₂ C ₉₄
C₄₄ C ₄₆ C ₄₈	C₄₈ C ₅₀ C ₅₂	C₆₄ C ₆₆ C ₆₈ C ₇₀	C₈₀ C ₈₂ C ₈₄ C ₈₆ C ₈₈	C₉₆ C ₉₈ C ₁₀₀ C ₁₀₂ C ₁₀₄ C ₁₀₆
C₅₀	C₅₄	C₇₂	C₉₀	C₁₀₈

All the fullerenes form five vertical columns (groups), having different symmetry. Two groups of three-fold symmetry differ by the structure of their apices. The 3-fold-symmetry group S has two sharp apices, the third-order axis going through them. The 3-fold-symmetry group T has two truncated apices, the third-order axis going through the centers of triangles. We suppose that the fullerenes of one and the same group have similar physical and chemical properties.

Strictly speaking, only the fullerenes denoted by bold symbols have the symmetry of a corresponding column. They are ideal (perfect) fullerenes. The others are imperfect or semi-perfect. As noted in Ref. [8] by analogy with crystal physics, the imperfection is connected with extra ‘interstitial’ dimers, playing the role of defects. Let us continue this analogy. In real crystals a long-range order is impossible in strict sense of the word, because of such defects as dislocations which violate translational symmetry. Nevertheless, the long-range order is observed experimentally, but this order is defined otherwise and is referred to as *topological long-range order* [19]. Following this example, we define the imperfect fullerenes conserving the main symmetry axis as having *topological symmetry*.

References

- [1] M. Endo, H.W. Kroto, Formation of carbon nanofibers // *J. Phys. Chem.* **96** (1992) 6941-6944.
- [2] N.S. Goroff, Mechanism of fullerene formation // *Acc. Chem. Res.* **29** (1996) 77-83.
- [3] Z. Slanina, X. Zhao, F. Uhlik, Model narrow nanotubes related to C₃₆, C₃₂ and C₂₀: initial computational structural sampling // *Mater. Sci. Engng B* **96** (2002) 164-168.
- [4] S.D. Khan, S. Ahmad, Modelling of C₂ addition rout to the formation of C₆₀ // *Nanotechnology* **17** (2006) 18-24.
- [5] Y. Yamaguchi, L. Colombo, Growth of sp-sp² nanostructures in a carbon plasma // *Phys. Rev.* **B76** (2007) 134119-1-7
- [6] S. Irle S, A.J. Page, B. Saha, Y. Wang, K.R.S. Chandrakumar, Y. Nishimoto, H-J. Qian, K. Morokuma, Atomistic mechanisms of carbon nanostructure self-assembly as predicted by nonequilibrium QM/MD simulations. In: *Practical Aspects of Computational Chemistry II: An Overview of the Last Two Decades and Current Trends*, ed. by J. Leszczynski and M. K. Shukla (Springer-European Academy of Sciences, 2012) pp.1-47.

- [7] N.A. Poklonski, S.V. Ratkevich, S.A. Vyrko, Quantum-chemical calculation of carbododecahedron formation in carbon plasma // *J. Phys. Chem.* **A119** (2015) 9133-9139.
- [8] A.I. Melker, M.A. Krupina, Geometric modeling of midi-fullerene growth from C_{24} to C_{48} // *St. Petersburg State Polytechnical University Journal. Physics and Mathematics* **3(248)** (2016) 52-58.
- [9] A.I. Melker, M.A. Krupina, Geometric modeling of midi-fullerenes growth from C_{32} to C_{60} // *St. Petersburg State Polytechnical University Journal. Physics and Mathematics* **10(1)** (2017) 47-54.
- [10] A.I. Melker, M.A. Krupina, Geometric modeling of midi-fullerenes growth from C_{40} to C_{68} // *Proceedings of NDTCS- 2017* **17** (2017) 64-68.
- [11] A.I. Melker, T.V. Vorobyeva, Fusion reactions of cupola half-fullerenes // *St. Petersburg State Polytechnical University Journal. Physics and Mathematics* **3(248)** (2016) 59-67.
- [12] A.I. Melker, S.N. Romanov, D.A. Kornilov, Computer simulation of formation of carbon fullerenes // *Materials Phys. Mech.* **2** (2000) 42-50.
- [13] A.I. Melker, D.A. Kornilov, S.N. Romanov, N.A. Izotova, Carbon nanotubes: formation and computer simulations // *Proc. SPIE* **5127** (2003) 76-80.
- [14] D.A. Kornilov, A.I. Melker, S.N. Romanov, Conformation transitions in fullerenes at non-zero temperatures // *Proc. SPIE* **5127** (2003) 81-85.
- [15] A. Chuvilin, U. Kaiser, E. Bichoutskaia, N.A. Besley, A.N. Khlobystov. Direct transformation of graphene to fullerene // *Nature Chem.* **2** (2010) 450-453.
- [16] E.L. Micelotta, A.P. Jones, J. Cami, E. Peeters, The formation of cosmic fullerenes from arographic clusters // *Astrophys. J.* **761(35)** (2012) 1-8.
- [17] F. Pietrucci, W. Andreoni, Fate of a graphene flake; a new rout toward fullerenes disclosed with ab initio simulations // *J. Chem. Theory Comput.* **10** (2014) 913-917.
- [18] A.I. Melker, *Dynamics of Condensed Matter, Vol. 3, Noophysics (Science and Scientists)* (St. Petersburg Academy of Sciences on Strength Problems, 2016) 151 p.
- [19] A.I. Melker, M.A. Krupina, R.M. Zarafutdinov, Periodic system for basic fullerenes obtained by fusion reactions // *Proceedings of NDTCS- 2017* **17** (2017) 72-75.
- [20] A.M. Kosevich, *Physical Mechanics of Real Crystals* (Kiev, Naukova Dumka, 1981) 328 p.

FULLERENES OF THE $\Delta n=10$ SERIES

Alexander I. Melker^{1*}, Maria A. Krupina², Ruslan M. Zarafutdinov¹

¹Department of Mechanics and Control Processes, ²Department of Experimental Physics,

Peter the Great St. Petersburg State Polytechnic University, Polytekhnicheskaya 29

195251, St. Petersburg, Russian Federation

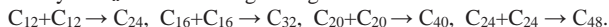
*e-mail: newton@imop.spbstu.ru

Abstract. Fusion reactions of cupola half-fullerenes C_{10} , C_{12} , C_{16} , C_{18} , C_{20} , C_{24} , C_{30} and C_{36} with each other are considered on the basis of Arrhenius's postulate. It means that at first there forms an intermediate compound and only afterwards a usual chemical reaction is going on. The final structure of fullerenes is obtained with the help of geometric modeling and is optimized through the use of Avogadro package. In general, the fullerenes which tend to take the appearance of a perfect spheroid have lesser formation energy. However, in some case self-organization of unshared electron pairs prevails. The energy of fullerenes C_{26} , C_{30} , C_{40} , C_{50} and C_{60} obtained is calculated and is explained in the context of strain-related stability as well as in the framework of interaction of electron valence pairs.

Keywords: cluster, cupola, energy, fullerene, fusion, modeling.

1. Introduction

The formation mechanism of fullerenes is still disputable and unresolved question. Many different models have been proposed to explain their arising. The known mechanisms can be categorized into two major groups: bottom-up and top-down models [1]. In the first case, fullerene cages and nanotubes are considered to be formed from carbon atoms and small carbon clusters. In the second case, fullerenes and nanotubes are thought as direct transformation of graphene into fullerenes and nanotubes. However the fullerenes can be also imagined to grow by reacting with each other, similar to bubbles in a soap solution. In Ref. [2] we considered this possibility using geometrical modeling. As a result, we have found the $\Delta n=8$ periodicity for the family of C_n fullerenes originating from the reactions:



The structures obtained have threefold, fourfold, fivefold and sixfold symmetry. Earlier we obtained the $\Delta n=4$ periodicity for the family of barrel-shaped mini-fullerenes C_{12} , C_{16} , C_{20} , C_{24} [3] and the $\Delta n=6$ periodicity for both the family of truncated bipyramids and the family beginning with a bi-shamrock (bi-trefoil); both families consisting of fullerenes C_{14} , C_{18} , C_{24} , C_{30} , C_{36} [4]. All these periodicities have one and the same main characteristic feature; the fullerene structure changes from threefold symmetry to sixfold through four and fivefold ones. For this reason, it seems reasonable to take this feature as a basis for fullerene classification. The question arises of whether there are other periodicities having the same symmetry character.

To answer this question, in this contribution we consider the growth of fullerenes through a series of joining reactions of cupola half-fullerenes C_{10} , C_{12} , C_{16} , C_{18} , C_{20} , C_{24} , C_{30} , and C_{36} . It will be shown that there appears the $\Delta n=10$ periodicity that allows extend the range of Δn periodicities.

2. Fusion reactions of cupola half fullerenes

In 1889 Svante August Arrhenius postulated that a chemical reaction goes in the following way. At first there forms some intermediate compound and only afterwards a usual chemical reaction is going on. For fullerenes this postulate can be written as follows $A + B \rightarrow (AB) \rightarrow C$. In Ref. [2] we have developed an algorithm that has proved itself in predicting the growth of perfect fullerenes conserving an initial symmetry, so called the fusion reaction algorithm. Consider now the reaction for fullerenes of the $\Delta n=10$ series.

Reaction between two cupolas C_{10} and C_{16} . In Figure 1 the atomic configurations corresponding to reaction $C_{10} + C_{16} \rightarrow (C_{10}C_{16}) \rightarrow C_{26}$ between two cupola-half-fullerenes are shown. At first two molecules are moving towards each other (Fig. 1, *a*). Then the boundary atoms, marked in dark-red, interact with each other producing a compound (Fig. 1, *b*). During this process new covalent bonds (heavy red lines) are generated. As a result, a distorted polyhedron is created which relaxes into a perfect polyhedron (Fig. 1, *c*). Its atomic configuration consists of three hexagons and twelve pentagons, so it can be named a hexa₃-penta₁₂ polyhedron. It is worth noting that the structure of this fullerene was also obtained by embedding dimer C_2 into fullerene C_{24} [5]; the dimer-embedding model being suggested by Endo and Kroto for the first time in 1992 [6].

Reaction between two cupolas C_{12} and C_{18} . Similar to the previous reasoning, let us consider the atomic configurations corresponding to reaction $C_{12} + C_{18} \rightarrow (C_{12}C_{18}) \rightarrow C_{30}$. As before, at first two molecules are moving towards each other (Fig. 1, *d*). Then the boundary atoms interact with each other producing a distorted polyhedron with the new covalent bonds (Fig. 1, *e*; heavy red lines) which relaxes into a perfect polyhedron (Fig. 1, *f*). It is worth noting that the structure and graph of this fullerene were also obtained by embedding three dimers into a tri₂-tetra₃-hexa₉ fullerene C_{24} [7]. Since its atomic configuration consists of two triangles, three set of adjacent pentagons and nine hexagons; it was named a tri₂-penta₆hexa₉- polyhedron.

Reaction between two cupolas C_{16} and C_{24} . The procedure for visualization of reaction $C_{16} + C_{24} \rightarrow (C_{16}C_{24}) \rightarrow C_{40}$ is the same as before. The atomic configuration corresponding to a perfect polyhedron consists of two squares, eight pentagons and twelve hexagons (Fig. 1, *i*), so it can be named a tetra₂-penta₈-hexa₁₂ polyhedron. It is worth noting that the structure and graph of this fullerene can be obtained by embedding four dimers into a tetra₆-hexa₁₂ polyhedron C_{32} .

Reaction between two cupolas C_{20} and C_{30} can be written as $C_{20} + C_{30} \rightarrow (C_{20}C_{30}) \rightarrow C_{50}$. The atomic structure corresponding to a perfect polyhedron (Fig. 1, *i*) consists of two isolated pentagons, five sets of adjacent pentagons and fifteen hexagons, so it can be named a penta₁₂-hexa₁₅ polyhedron. It is worth noting that the structure and graph of this fullerene can be also obtained by embedding five carbon dimers into a tetra₅-penta₂-hexa₁₅ polyhedron C_{40} .

Reaction between two graphene fragment C_{24} and cupola C_{36} . The procedure for visualization of reaction $C_{24} + C_{36} \rightarrow (C_{24}C_{36}) \rightarrow C_{60}$ is the same as before. The atomic structure corresponding to a perfect polyhedron (Fig. 1, *o*) consists of six sets of adjacent pentagons and twenty hexagons, so it can be named a penta₁₂-hexa₂₀ polyhedron. It is worth noting that the similar structure and graph of this fullerene can be also obtained using Endo-Kroto model by embedding six carbon dimers into a tetra₆-hexa₂₀ polyhedron C_{48} .

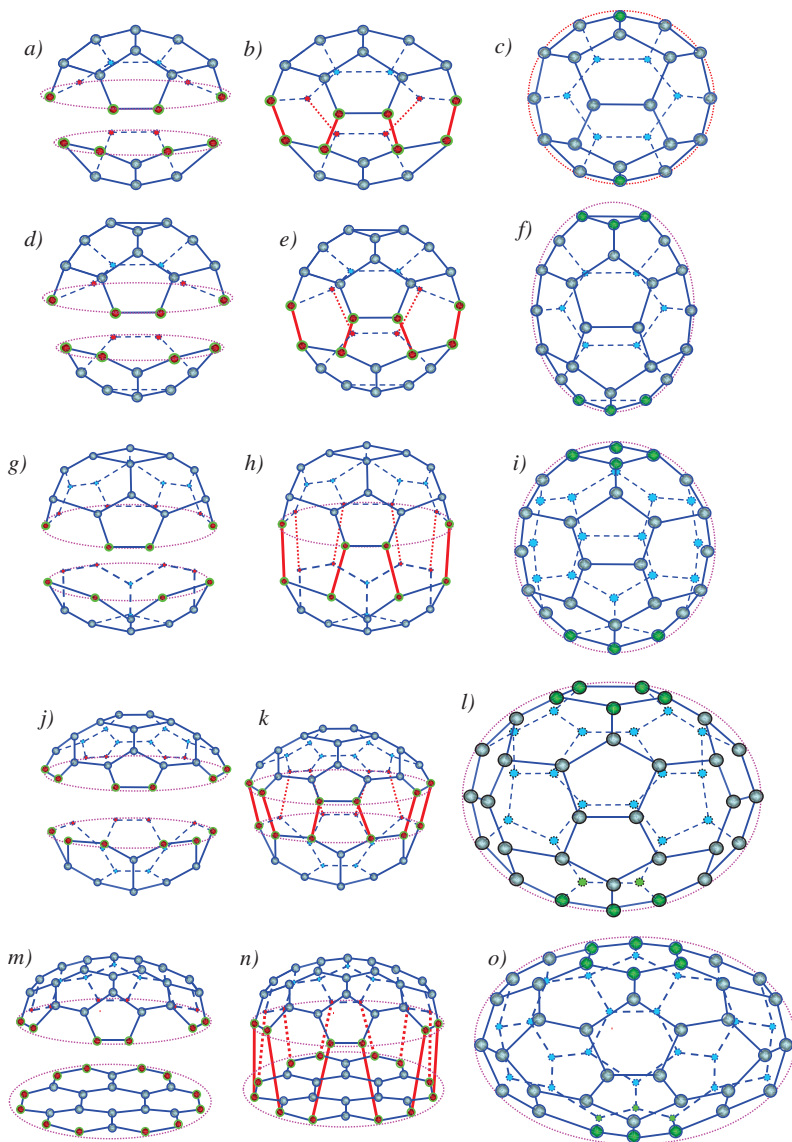


Fig. 1. Joining of cupolas C₁₀, C₁₂, C₁₆, C₁₈, C₂₀, graphene fragment C₂₄, cupola C₃₀, and cupola C₃₆; separate carbon cupolas (a, d, g, j, m); intermediate compounds (b, e, h, k, m); polyhedrons after relaxation (c, f, i, l, o, m). Dark-red and light-blue balls are reacting and neutral atoms, respectively; thin light-blue solid and dashed lines are covalent bonds; heavy dark-red solid and dashed lines are new covalent bonds.

3. Single and double bonds, energy

Atomic force microscopy clearly showed [8] the two different types of bonds for symmetry equivalent hexagons in fullerene C_{60} . The measured bond lengths are $r_{hh}=1.38(2)$ Å and $r_{hp}=1.454(12)$ Å. The short bonds are attributed to double bonds. Knowing this fact, it is not difficult to incorporate the double bonds into the structure of fullerene C_{60} [9, 10]. But how it can be done in the case of other fullerenes and cupolas?

We assume that the symmetry of double bonds location about the major axis of cupolas and fullerenes coincides with that of fullerene C_{60} . Using this postulate, we have all the necessary input data for the optimization of the fullerene and cupola structures designed by means of geometric modeling and for subsequent calculation of their properties. As it was described above, the cupolas having one and the symmetry can react with each other producing fullerenes C_{30} , C_{40} , C_{50} , and C_{60} with single and double covalent bonds and, in the case of fullerene C_{26} , with partially delocalized bonds too. The optimized structures of these fullerenes obtained through the use of Avogadro package [11] are shown in Figure 2. It should be emphasized that we developed a modified geometric graphics because the package graphics is incomprehensible.

We have calculated formation energies of the fullerenes (Fig. 2). The energy change for fullerenes C_{30} , C_{40} , C_{50} and C_{60} can be easily explained in the context of the second from “five basic empirical arguments” formulated by Harold Kroto who shared the 1996 Nobel Prize for chemistry for his co-discovery of fullerenes [12].

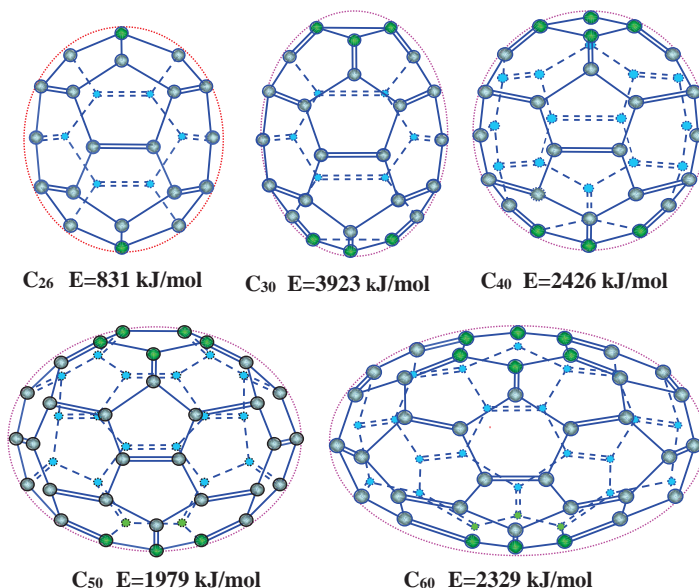


Fig. 2. Structure and energy of the $\Delta n=10$ series fullerenes with single and double bonds.

Polyaromatic hydrocarbons with five- and six-membered rings are abundant, but three- and four-membered rings are very unstable and seven-membered ones are rare. This suggests that only 5/6-ring networks are likely to occur readily. The cages must contain 12 pentagonal rings, but the number of hexagonal ones is not directly restricted.

Really, this is reflected in the structure and energy of fullerenes mentioned above, but this argument cannot explain why fullerene C_{26} has the least energy which drastically differs from that of fullerene C_{50} ; both fullerenes have a similar structure formed from pentagons and hexagons only. We assume that the reason of discrepancy lies in ignoring an electron structure of fullerenes.

4. Graph representation and electronic structure

Today there is no clear and unique theory of fullerene growth. "The problem is not the lack of imagination, because quite numerous models have been proposed. What is rather lacking is a model using quantities that might be evaluated and measured. Moreover, a theoretical model, in order to deserve its name, should lead to numerical predictions. In order to represent something more than a set of circular arguments, a model should predict more numerical values, parameters or functional relations than the number of input parameters" [13].

At this time there are a lot of papers on fullerene properties [14, and 277 references therein]. Using different computational methods (there are also a lot of programs), the authors calculate the properties of the most popular fullerenes which structure is known. As a result, the numbers obtained contradict to each other and only increase disordered information. To our mind, the absence of appreciable progress in understanding fullerene nature is determined by the domination of numerical calculations on the known structures. However, such numerical calculations are unable to predict new structures, so the 'numerical progress' results mainly in increasing numerical entropy. It should be emphasized that numerical calculations are not a theory, but a kind of numerical experiment [15].

The theoretical approach to fullerenes is based on the topological and graph treatment [10, and 350 references therein]. "The fullerene graphs contain all the information we need, and we able to sort through the millions of isomers, finding a few candidates for the most stable, by way of simple easily computed topological indices for pentagons or hexagons" [10]. At that, the authors define (classical) fullerenes as "cage-like, hollow molecules of pseudospherical symmetry consisting of pentagons and hexagons only, resulting in a trivalent (and in the most ideal case) convex polyhedron with exactly three edges (bonds) joining every vertex occupied by carbon, idealized as sp^2 hybridized atoms".

Earlier we have used the term "fullerene" in a broad sense as any convex shape inscribed into a spherical surface which can be composed of atoms, each atom having three nearest neighbors, as in usual fullerenes, whenever discussing hollow carbon clusters [16]. Such geometrical approach allowed obtaining possible forms of mini-fullerenes from C_4 and C_{20} . At that, we have constructed graphs for all these mini-fullerenes [3, 17]. The graph analysis simplifies an understanding of both the ways of fullerene growth and their structures obtained.

Consider the graphs which characterize the formation of the fullerenes of the $\Delta n=10$ series (Fig. 3). From the graph representation it follows that the main difference of fullerene C_{26} from others is the absence of double bonds in the graph center. Therefore the electronic structure in this area of fullerene C_{26} differs from that of other fullerenes. In other words, fullerene C_{26} does not refer to classical fullerenes defined in Ref. [10]. Let us take up the situation in more detail.

In 1940 Sidgwick and Powell supposed that the geometry of a forming molecule is dictated by repulsion of valence electron pairs [18, 19]. They formulated the following rule: electron pairs arrange themselves inside the valence shell of an atom into such configuration which ensures their maximal removing from each other. In other words, the electrons pairs behave themselves as if were repelling each other similar to point charges. The assumption is in a good agreement with experimental data for more than 1500 molecules.

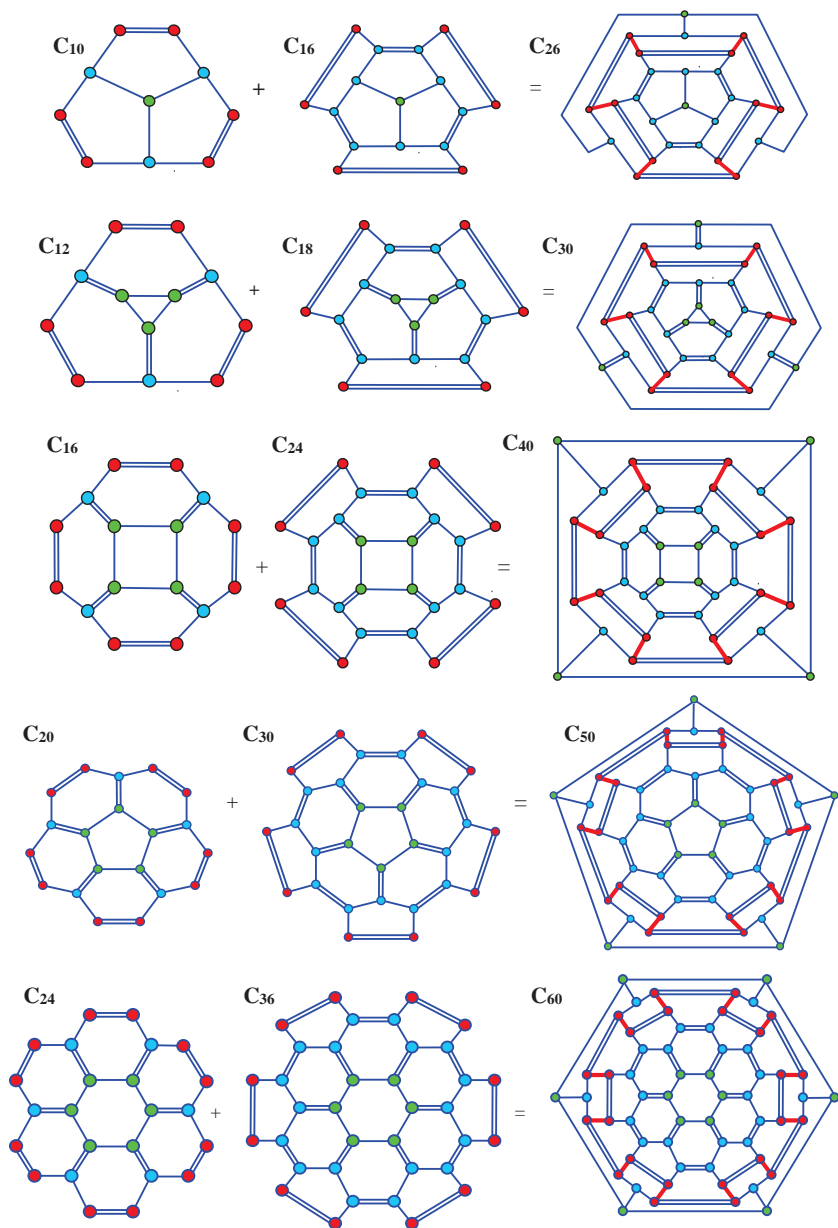


Fig. 3. Fusion reactions of cupolas as connection of two graphs; all notations are the same as before.

If each electron pair present as a point and to connect the points by direct lines, one obtains the electronic configuration of chemical bonds [19, 20]. Each configuration at a given number of electron pairs can create several space molecular structures. It depends on the number of binding and unshared pairs.

Denote a central atom of a molecule by letter A and a noncentral atom by B . Let a molecule AB_4 has no multiple bonds. For four binding electron pairs, the configuration is a tetrahedron, and we have a tetrahedral molecule, for example, methane (Fig. 4). Here the atomic configuration repeats the electronic. For a molecule AB_3 the valence shell of which contains three binding pairs and one unshared, the situation is radically different. Here the unshared electron pair is on a line which connects the central atom with one of tetrahedron apices. As a result, the molecule has the form of pyramid, for example, a molecule of ammonia (Fig. 4). In this case the electronic and atomic configurations do not coincide and we have so called *hidden symmetry* [21].

We studied the growth of fullerene C_{26} from methane through isobutene and carbon hydrides, conserving three-fold symmetry, to its final form and have come to conclusion that C_{26} has the electronic structure shown in Figure 4.

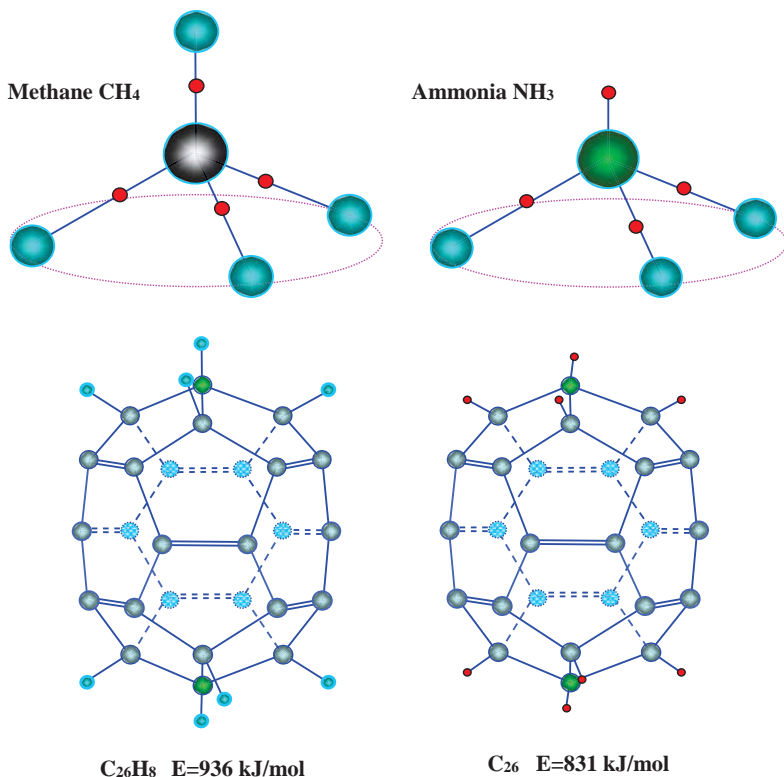


Fig. 4. Methane, ammonia, fullerene hydride $C_{26}H_8$ and fullerene C_{26} having three-fold symmetry; red dots denote electron pairs.

Therefore fullerene C₂₆ does not represent a classical fullerene which is defined as “a convex polyhedron with exactly three edges (bonds) joining every vertex occupied by carbon, idealized as sp² hybridized atoms”. To our mind, fullerene C₂₆ consists only of sixteen sp² hybridized atoms (as in a classical fullerene) and eight sp³ hybridized carbon atoms having unshared electron pairs much as nitrogen atom in ammonia.

5. Conclusion

In this contribution fusion reactions of cupola half-fullerenes C₁₀, C₁₂, C₁₆, C₁₈, C₂₀, C₂₄, C₃₀ and C₃₆ with each other are considered on the basis of Arrhenius's postulate. It means that at first there forms an intermediate compound and only afterwards a usual chemical reaction is going on. The final structure of fullerenes is obtained with the help of geometric modeling and is optimized through the use of Avogadro package. In general, the fullerenes which tend to take the appearance of a perfect spheroid have lesser formation energy. However, in some case self-organization of unshared electron pairs prevails. The energy of fullerenes C₂₆, C₃₀, C₄₀, C₅₀ and C₆₀ obtained is calculated and is explained in the context of strain-related stability as well as in the framework of interaction of electron valence pairs.

References

- [1] A.I. Melker, M.A. Krupina, Geometric modeling of midi-fullerenes growth from C₃₂ to C₆₀ // *St. Petersburg State Polytechnical University Journal. Physics and Mathematics* **10(1)** (2017) 47-54.
- [2] A.I. Melker, T.V. Vorobyeva, Fusion reactions of cupola half-fullerenes // *St. Petersburg State Polytechnical University Journal. Physics and Mathematics* **3(248)** (2016) 59-67.
- [3] A.I. Melker, S.A. Starovoitov, T.V. Vorobyeva, Classification of mini-fullerenes on graph basis // *Materials Physics and Mechanics* **20(1)** (2014) 12-17.
- [4] A.I. Melker, M.A. Krupina, Designing mini-fullerenes and their relatives on graph basis // *Materials Physics and Mechanics* **20(1)** (2014) 18-24.
- [5] M.A. Krupina, A.I. Melker, S.A. Starovoitov, T.V. Vorobyeva, Structure and graphs of midi-fullerenes // *Proceedings of NDTCS' 2015* **16** (2015) 23-26.
- [6] M. Endo, H.W. Kroto, Formation of carbon nanofibers // *J. Phys. Chem.* **96** (1992) 6941-6944.
- [7] A.I. Melker, M.A. Krupina, Geometric modeling of midi-fullerenes growth from C₂₄ to C₄₈ // *St. Petersburg State Polytechnical University Journal. Physics and Mathematics* **3(248)** (2016) 52-58.
- [8] L. Gross, F. Mohn, N. Moll, B. Schuler, A. Criado, E. Guitián, D. Peña, A. Gourdon, G. Meyer, Bond-order discrimination by atomic force microscopy // *Science* **337** (2012) 1326-1329.
- [9] S.V. Kozyrev, V.V. Rotkin, Fullerene. Composition, dynamics of crystal lattice, electronic structure and properties // *Fiz. Tverd. Tela* **27(9)** (1993) 1409-1434.
- [10] P. Schwerdtfeger, L.N. Wirz, J. Avery, The topology of fullerenes // *WIREs Comput. Mol. Sci.* **5** (2015) 96-145.
- [11] M.D. Hanwell, D.E. Curtis, D.C. Lonie, T. Vandermeersch, E. Zurek, G.R. Hutchison, Avogadro: an advanced semantic chemical editor, visualization, and analysis platform // *Journal of Cheminformatics* **4(17)** (2012); Avogadro: an open-source molecular builder and visualization tool. Version 1.XX. <http://avogadro.cc/>
- [12] H.W. Kroto, The stability of the fullerenes C_n, with n= 24, 32, 36, 50, 60 and 70 // *Nature* **329** (1987) 529-531.
- [13] R. Kerner, Nucleation and growth of fullerenes // *Computational Materials Science* **2** (1994) 500-508.

- [14] S. Irle, A.J. Page, B. Saha, Y. Wang, K.R.S. Chandrakumar, Y. Nishimoto, H-J. Qian, K. Morokuma, Atomistic mechanisms of carbon nanostructure self-assembly as predicted by nonequilibrium QM/MD simulations. In: *Practical Aspects of Computational Chemistry II: An Overview of the Last Two Decades and Current Trends*, ed. by J. Leszczynski and M. K. Shukla (Springer-European Academy of Sciences, 2012) 59 p.
- [15] A.I. Melker, *Modeling Experiment* (Znanie, Moscow 1991) 64 p.
- [16] A.I. Melker, V. Lonch, Atomic and electronic structure of mini-fullerenes from four to twenty // *Materials Physics and Mechanics* **13(1)** (2012) 22-36.
- [17] A.I. Melker, Possible ways of forming mini-fullerenes and their graphs // *Materials Physics and Mechanics* **20(1)** (2014) 1-11.
- [18] N.V. Sidgwick, H.M. Powell, Stereochemical types and valency groups // *Proc. Roy. Soc. Series A* **176(965)** (1940) 153-180.
- [19] R.J. Gillespie, *Molecular Geometry* (Van Nostrand Reinhol Co., London, 1972).
- [20] A.I. Melker, M.A. Vorobyeva (now Krupina), Electronic theory of molecule vibrations // *Proceeding of SPIE* **6253** (2006) 625305-1-15.
- [21] A.I. Melker, M.A. Krupina, Hidden symmetry or why cyclic molecules have so strange forms // *Materials Physics and Mechanics* **9(1)** (2010) 11-19.

FULLERENES OF THE $\Delta n=12$ SERIES

Alexander I. Melker^{1*}, Maria A. Krupina², Ruslan M. Zarafutdinov¹

¹Department of Mechanics and Control Processes, ²Department of Experimental Physics,

Peter the Great St. Petersburg State Polytechnic University, Polytekhnicheskaya 29

195251, St. Petersburg, Russian Federation

*e-mail: newton@imop.spbstu.ru

Abstract. Fusion reactions of cupola half-fullerenes C_{16} , C_{18} , C_{24} , C_{30} and C_{36} with each other are considered on the basis of Arrhenius's postulate. It means that at first there forms an intermediate compound and only afterwards a usual chemical reaction is going on. The final structure of fullerenes is obtained with the help of geometric modeling and is optimized through the use of Avogadro package. In general, the fullerenes which tend to take the appearance of a perfect spheroid have lesser formation energy. The energy of fullerenes C_{32} , C_{36} , C_{48} , C_{60} and C_{72} obtained is calculated. The periodic system of basic perfect fullerenes is suggested.

Keywords: cluster, cupola, energy, fullerene, fusion, modeling.

1. Introduction

Fullerenes can grow by reacting with each other, similar to bubbles in a soap solution. This possibility was demonstrated by the example of such reaction as $C_{24}+C_4 \rightarrow C_{28}$, $C_{30}+C_30 \rightarrow C_{60}$ through the use of a new molecular dynamics that takes into account simultaneously both atomic and electronic degrees of freedom [1, 2]. In spite of these encouraging results we came to conclusion that the problem of fullerene growth must be split into two: geometry and calculations. The reasons are as follows.

In 1984 it has been found that the time-of-flight mass spectrometry (TOF-MS) distribution of laser-evaporated graphite soot had a bimodal character [3], the low-mass distribution having peaks for C_{11} , C_{15} , C_{19} and C_{23} species with $\Delta n = 4$ periodicity. Little later fullerenes C_{60} and C_{70} were synthesized and a set of simple, empirical chemical and geodesic rules was presented by H.W. Kroto to explain the remarkable stability observed for the C_{60} molecule [4]. The rules yield cluster magic numbers consistent with observation. The authors of the large review having 277 references [5] state: "Today we interpret the TOF-MS distribution as linear carbon chains in the region $1 < n < 10$, macrocyclic rings $10 < n < 30$, and fullerenes $n > 36$ with a forbidden zone between $n=30$ and 36 ".

We can't agree with this interpretation for many reasons, two of the most serious are:

- The interpretation does not explain $\Delta n = 4$ periodicity.
- It was shown through the use of molecular dynamics [6] as well as analytically [7] that linear chains with free ends and with periodic boundary conditions (rings) are unstable with respect to vibrations; they transform at first into zigzag chains, helices, and then folds into compact structures. The reason is that small longitudinal vibrations transfer their energy to large transversal vibrations. This phenomenon was named as parametric resonance.

In Ref. [8, 9] using the analogy with polymer physics and radiation solid state physics we unexpectedly obtained the $\Delta n = 4$ periodicity for caged carbon molecules C_{12} , C_{16} , C_{20} , C_{24} . The structures have threefold, fourfold, fivefold and sixfold symmetry. Clearly the following reasoning was: if there exists the $\Delta n = 4$ periodicity, provably there are other periodicities.

Really, we have found the $\Delta n=8$ periodicity [10] for the family of C_n fullerenes originating from the reactions of cupolas $C_{10}+C_{10} \rightarrow C_{20}$, $C_{12}+C_{12} \rightarrow C_{24}$, $C_{16}+C_{16} \rightarrow C_{32}$, $C_{20}+C_{20} \rightarrow C_{40}$, $C_{24}+C_{24} \rightarrow C_{48}$, where the structures had also the same symmetry. Since all these periodicities have one and the same main feature, namely, the transition from threefold symmetry to sixfold, it seems reasonable, to take this feature as a basis for fullerene classification and to search other periodicities. It should be noted that calculations performed for small fullerenes are unable to be such a basis on default of any other adequate explanation. For example, for C_{20} the most stable isomer can have a ring, a bowl or a fullerene structure, depending on the computational method employed [11].

In this contribution we consider the growth of fullerenes through a series of joining reactions of cupola half-fullerenes C_{16} , C_{18} , C_{24} , C_{30} , and C_{36} . It will be shown that there appears the $\Delta n=12$ periodicity having the same symmetry transition.

2. Fusion reactions of cupola half fullerenes

In 1889 Svante August Arrhenius postulated that a chemical reaction goes in the following way. At first there forms some intermediate compound and only afterwards a usual chemical reaction is going on. For fullerenes this postulate can be written as follows $A + B \rightarrow (AB) \rightarrow C$. In Ref. [10] we have developed an algorithm that has proved itself in predicting the growth of perfect fullerenes conserving an initial symmetry, so called the fusion reaction algorithm.

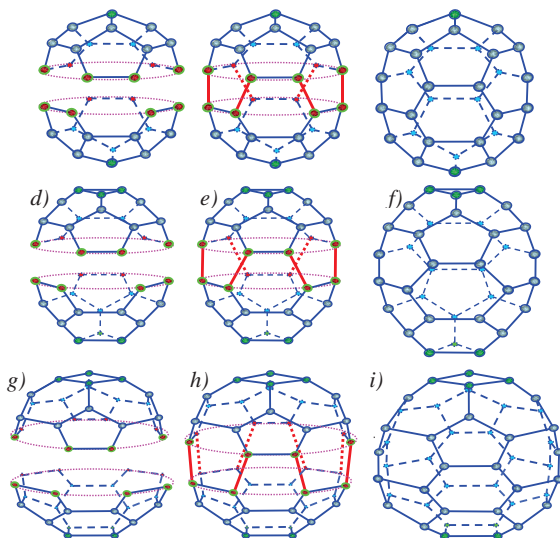
Reaction between two cupolas $C_{16} + C_{16} \rightarrow (C_{16}C_{16}) \rightarrow C_{32}$ is shown in Figure 1 *a, b, c*.

Reaction between two cupolas $C_{18} + C_{18} \rightarrow (C_{18}C_{18}) \rightarrow C_{36}$ is presented in Figure 1 *d, e, f*.

Reaction between two cupolas $C_{24} + C_{24} \rightarrow (C_{24}C_{24}) \rightarrow C_{48}$ is displayed in Figure 1 *g, h, i*.

Reaction between two cupolas $C_{30} + C_{30} \rightarrow (C_{30}C_{30}) \rightarrow C_{60}$ is exhibited in Figure 1 *j, k, l*.

Reaction between two cupolas $C_{36} + C_{36} \rightarrow (C_{36}C_{36}) \rightarrow C_{72}$ is shown in Figure 1 *m, n, o*.



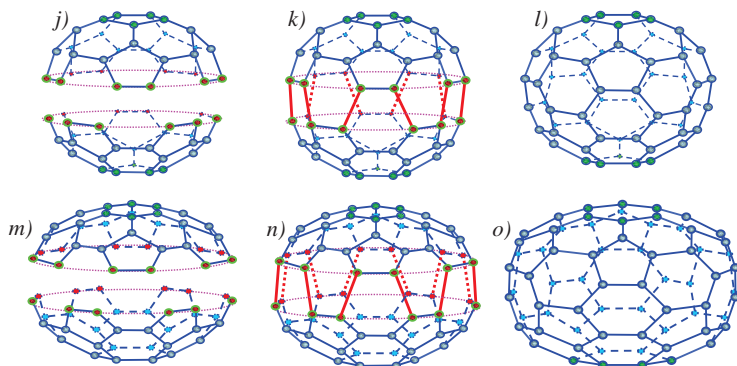


Fig. 1. Joining of two half-fullerenes C_{16} , C_{18} , C_{24} , C_{30} and C_{36} ; separate carbon cupolas (*a*, *d*, *g*, *j*, *m*); intermediate compounds (*b*, *e*, *h*, *k*, *m*); polyhedrons after relaxation (*c*, *f*, *i*, *l*, *o*, *m*). Dark-red and light-blue balls are reacting and neutral atoms, respectively; light-blue solid and dashed lines are covalent bonds; dark-red solid and dashed lines are new covalent bonds.

3. Single and double bonds

We assume that the symmetry of double bonds location about the major axis of cupolas and other fullerenes coincides with that of fullerene C_{60} . Using this postulate, we have all the necessary input data for the optimization of the fullerene and cupola structures designed by means of geometric modeling and for subsequent calculation of their properties. As it was described above, the cupolas having one and the symmetry can react with each other producing fullerenes C_{36} , C_{48} , C_{60} , and C_{72} with single and double covalent bonds and, in the case of fullerene C_{32} , with partially delocalized bonds too. The optimized structures of the fullerenes obtained through the use of Avogadro package [12] are shown in Figure 2.

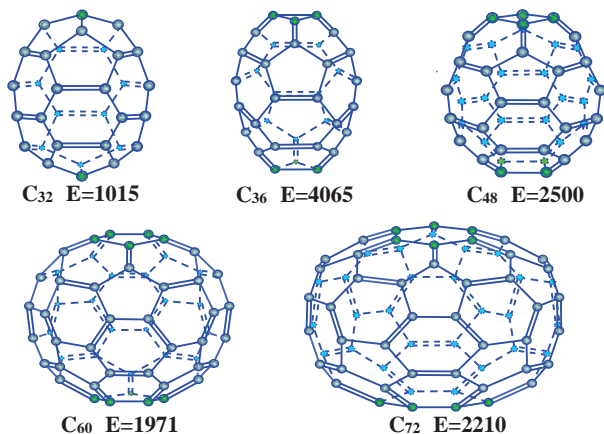


Fig. 2. Structure and energy (in kJ/mol) of the $\Delta n=12$ series fullerenes.

4. Symmetry and energy of perfect fullerenes

Modeling the growth of fullerenes from C_{24} (D_{3h} symmetry) to C_{48} , we have obtained the perfect fullerenes C_{30} and C_{36} conserving three-fold symmetry [13]. Modeling the growth of fullerenes from C_{32} (D_{4h} symmetry) to C_{60} , we found perfect fullerenes C_{40} and C_{48} conserving four-fold symmetry [14]. The mass difference between successive fullerenes in the first case is $\Delta m=6$, in the second case $\Delta m=8$. It should be emphasized that in both cases the mass difference is equal to a double degree of symmetry.

It is intriguing to combine periodicities, Δm and Δn , in order to gain a better understanding of the energy results obtained. With this in mind, we designed the fullerenes of the neighbor periodicities $\Delta n=6, 8, 10, 14$ and 16 using geometrical modeling, optimized their structures through the use of Avogadro package, and calculated their energies (in kJ/mol). The results are given in the Table where all the fullerenes form five vertical columns (groups), having different symmetry. Two groups of three-fold symmetry differ by the structure of their apices. The 3-fold-symmetry group S has two sharp apices, the third-order axis going through them. The 3-fold-symmetry group T has two truncated apices, the third-order axis going through the centers of triangles. For the $\Delta n=6$ series fullerenes, there are two energy values because this series has two families [15].

Periodic System of Basic Perfect Fullerenes

Series (horizontal) Groups (vertical)	Symmetry of Fullerenes				
	3-fold S $\Delta m=6$	3-fold T $\Delta m=6$	4-fold $\Delta m=8$	5-fold $\Delta m=10$	6-fold $\Delta m=12$
$\Delta n=6$	C₁₄ 1657 1367	C₁₈ 3985 4060	C₂₄ 3985 3046	C₃₀ 1907 3059	C₃₆ 1884 2443
$\Delta n=8$	C₂₀ 1647	C₂₄ 3667	C₃₂ 2291	C₄₀ 2007	C₄₈ 2562
$\Delta n=10$	C₂₆ 831	C₃₀ 3923	C₄₀ 2426	C₅₀ 1979	C₆₀ 2329
$\Delta n=12$	C₃₂ 1015	C₃₆ 4065	C₄₈ 2500	C₆₀ 1970	C₇₂ 2210
$\Delta n=14$	C₃₈ 1206	C₄₂ 4253	C₅₆ 2643	C₇₀ 2069	C₈₄ 2255
$\Delta n=16$	C₄₄ 1399	C₄₈ 4446	C₆₄ 2802	C₈₀ 2203	C₉₆ 2365
$\Delta n=18$	C₅₀	C₅₄	C₇₂	C₉₀	C₁₀₈

The energy minimum for the fullerenes of 3-fold-symmetry group S refer to fullerene C_{26} , for the fullerenes of 3-fold-symmetry group T corresponds to fullerene C_{24} , for the fullerenes of 4-fold-symmetry to fullerene C_{32} , for the fullerenes of 5-fold-symmetry matches to well-known fullerene C_{60} and for the fullerenes of 6-fold-symmetry to fullerene C_{72} . These results need further consideration.

References

- [1] A.I. Melker, S.N. Romanov, D.A. Kornilov, Computer simulation of formation of carbon fullerenes // *Materials Physics and Mechanics* **2(1)** (2000) 42-50.

- [2] D.A. Kornilov, A.I. Melker, S.N. Romanov, Conformation transitions in fullerenes at non-zero temperatures // *Proceedings of SPIE* **5127** (2003) 81-85.
- [3] E.A. Rohlfing, D.M. Cox, A. Kaldor, Production and characterization of supersonic carbon cluster beams // *J. Chem. Phys.* **81(7)** (1984) 3322-3330.
- [4] H.W. Kroto, The stability of the fullerenes C_n , with $n=24, 28, 32, 36, 60, 60$ and 70 // *Nature* **329** (1987) 529-531.
- [5] S. Irle, A.J. Page, B. Saha, Y. Wang, K.R.S. Chandrakumar, Y. Nishimoto, H-J. Qian, K. Morokuma, Atomistic mechanisms of carbon nanostructure self-assembly as predicted by nonequilibrium QM/MD simulations, In: *Practical Aspects of Computational Chemistry II: An Overview of the Last Two Decades and Current Trends*, Ed. by J. Leszczynski and M. K. Shukla (Springer-European Academy of Sciences, 2012) 59 p.
- [6] A.I. Melker, T.V. Vorobyeva, Polymer crystallization as the self-organization of chain macromolecules // *Zeitschrift für Naturforschung* **49a(11)** (1994) 1045-1052.
- [7] A.I. Melker, T.V. Vorobyeva, Parametric resonance of the transverse waves in polymer macro-molecules: a reason for folding // *Nanobiology* **4** (1996) 71-82.
- [8] A.I. Melker, Possible ways of forming mini-fullerenes and their graphs // *Materials Physics and Mechanics* **20(1)** (2014) 1-11.
- [9] A.I. Melker, S.A. Starovoitov, T.V. Vorobyeva, Classification of mini-fullerenes on graph basis // *Materials Physics and Mechanics* **20(1)** (2014) 12-17.
- [10] A.I. Melker, T.V. Vorobyeva, Fusion reactions of cupola half-fullerenes // *St. Petersburg State Polytechnical University Journal. Physics and Mathematics* **3(248)** (2016) 59-67.
- [11] Z. Chen, H. Jiao, M. Bühl, A. Hirsch, W. Thiel, Theoretical investigation into structures and magnetic properties of smaller fullerenes and their heteroanalogues // *Theoretical Chemistry Accounts* **106** (2001) 352-363.
- [12] M.D. Hanwell, D.E. Curtis, D.C. Lonie, T. Vandermeersch, E. Zurek, G.R. Hutchison, Avogadro: an advanced semantic chemical editor, visualization, and analysis platform // *Journal of Cheminformatics* **4(17)** (2012); Avogadro: an open-source molecular builder and visualization tool. Version 1.XX. <http://avogadro.cc/>
- [13] A.I. Melker, M.A. Krupina, Geometric modeling of midi-fullerenes growth from C_{24} to C_{48} // *St. Petersburg State Polytechnical University Journal. Physics and Mathematics* **3(248)** (2016) 52-58.
- [14] A.I. Melker, M.A. Krupina, Geometric modeling of midi-fullerenes growth from C_{32} to C_{60} // *St. Petersburg State Polytechnical University. Physics and Mathematics* **10(1)** (2017) 47-54.
- [15] A.I. Melker, M.A. Krupina, Designing mini-fullerenes and their relatives on graph basis // *Materials Physics and Mechanics* **20(1)** (2014) 18-24.

DESIGN AND SIMULATION OF ADDITIVE MANUFACTURED STRUCTURES OF THREE-COMPONENT COMPOSITE MATERIAL

A.Yu. Zobacheva*, A.S. Nemov, A.I. Borovkov, A.D. Novokshenov

M.V. Khovaiko, N.A. Ermolenko

Peter the Great St. Petersburg Polytechnic University, Polytekhnicheskaya 29

195251, St. Petersburg, Russia

*e-mail: zobacheva@compmechlab.com

Abstract. Modeling the microstructure of a three-component composite material obtained by layer-by-layer 3D printing is presented. The effect of the microstructure parameters on mechanical characteristics of the composite material created by 3D printing is studied. On the basis of multiscale simulations, an optimal configuration of the plate of composite material is designed and manufactured by 3D printer.

Keywords: composite, design, finite element, structure.

1. Introduction

A main tendency in the modern technology era is the transition from using traditional materials in the industry to using advanced materials with pre-defined properties such as composite materials. Nowadays, composite materials based on carbon fibers and polymer matrices are widely used in rocket-space and aviation engineering. The materials of such structures have high strength and low mass.

One of the modern approaches to creating composite materials is 3D printing or additive technologies. This manufacturing method allows obtain composite structures almost of any shape using different materials of binders and reinforcing fibers. An overview on 3D printing techniques of polymer composite materials and the properties and performance of 3D printed composite parts is given in Ref. [1]. A thermoplastic composite reinforced with long fibers and employed thermotropic liquid crystalline polymers is described in Ref. [2]. It was shown that the mechanical performance of the 3D printed thermosetting composites was superior to that of similar 3D printed thermoplastic composites and 3D printed short carbon fiber reinforced composites [3].

At the same time, the use of thermoplastic and thermosetting binders makes it possible to achieve good adhesion of the components while maintaining the inherent elasticity of the thermoplastics and maintainability of the material. The production of such three-component material is carried out in two stages during 3D printing. At the first stage, the carbon fibers are impregnated with a thermosetting binder and completely cured; at the second stage, the resulting microplastic is coated with a melt of a thermoplastic binder. When manufacturing composite products through the use of the described technology, a certain spread of microstructure characteristics arises inevitably, besides defects are also formed.

Studying and simulation of mesostructure and microstructure of a three-component composite material obtained by the 3D printing method, as well as studying the effect of a possible variation of the microstructure characteristics on mechanical properties of the material is described in Ref. [4]. Figure 1 shows an example of mesostructure of a real-scale sample

manufactured by 3D printer [5]. Finite element (FE) models of the mesostructure we were used to simulate the behavior of composite material. The developed technique of modeling three-component composite materials allows also studying large-sized structures of any configuration.



Fig. 1. Mesostructure of a three-component material and its FE model.

2. Optimization of lattice structures

Now lattice structures have become widespread in many areas. Their obvious advantage is the light weight and significant cost savings of a material. Application of unidirectional composite materials allows preserve the exceptional strength properties of composites in construction regardless of the loading direction. For this reason, the lattice composite structures are actively used in the aerospace industry.

The goal of this work is the study of the property change of lattice structures of three-component composite materials depending on their parameters, as well as the determination of optimal configurations of these structures. During the work, the software of finite element analysis ANSYS and the software modeFRONTIER for solving the tasks of criterion and multi-criteria optimization were used.

As an example of lattice structure, we considered construction of a plate type. The lattice structure element has the overall dimensions $(200 \pm 5) \times (200 \pm 5) \times (22 \pm 1)$ mm. A sample of a large-sized lattice structure should have the overall dimensions $(1400 \pm 5) \times (1400 \pm 5) \times (22 \pm 1)$ mm. The initial configuration variants of the plate are shown in Figure 2.

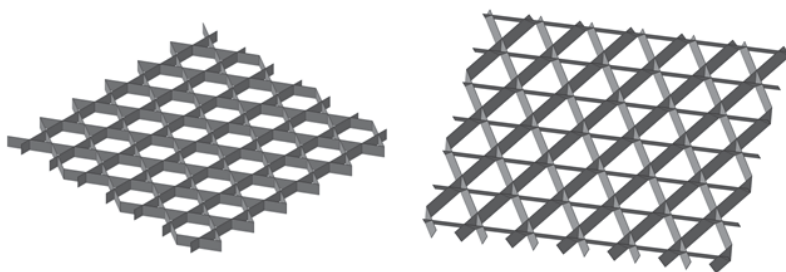


Fig. 2. Variants of the initial configuration of a plate.

The following set of optimization parameters is assumed: number of inclined ribs, number of horizontal/vertical ribs, inclination angle of the ribs to the horizontal axis in the plane of the plate, inclination angle of the diagonal ribs to the vertical axis perpendicular to the plate. The problem solution is considered in a 2-criterion formulation. The target functions are: weight of the structure, maximum deflection. Before performing parametric optimization the effect of

each optimization parameter on the target functions is investigated to study the possibility of limiting the parameters and the range of their variation.

In order to determine the initial configuration of the plate, two simplified versions of the structure are considered: with one vertical and one horizontal edge (Fig. 3a) and with two diagonal edges (Fig. 3b). The maximum displacements under the action of a given load are shown in Figure 3 and in Table 1.

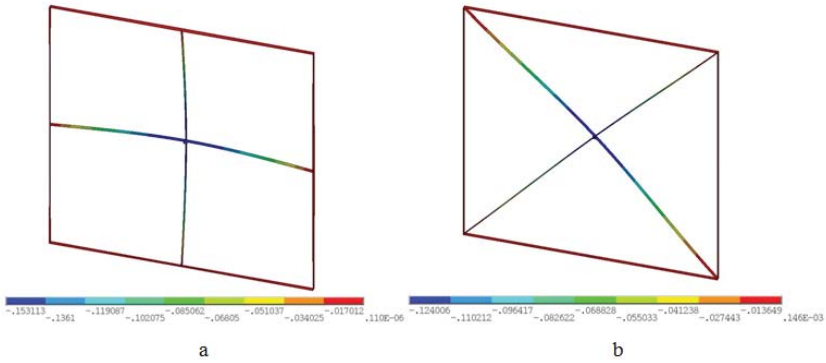


Fig. 3. Maximum displacement (deflection) of the plate, m.

Table 1. Results of calculation of a simplified plate configuration.

	Straight	Diagonal
Deflection, mm	153.11	124.01
Plate weight, kg	0.34	0.385

In the case of the rib diagonal position, the deflection is less than 19%. At the same time, the weight of such design is higher by 11%. It is necessary to investigate the dependence of weight on deflection with the number increase of edges in both constructions. The results of this analysis are shown in Figure 4. From this it follows that the configuration of the plate with diagonal ribs is characterized by a smaller deflection with a smaller weight. It should be noted also that among the designs with inclined edges, the minimum deflection is fixed at the inclination angle of the ribs equal to 45°. Figure 5 shows the dependence of the plate deflection on the slope angle of the edges with a constant weight of the plate. Thus, the configuration of the inclined rib design becomes the basis for further investigation; the angle of ribs being no longer considered as an optimization parameter.

We have considered the addition of straight (horizontal and vertical) edges to the basic construction (with diagonal edges). Figure 6 shows the displacements of the construction with 36 diagonal edges and 16 additional straight edges (a quarter of the construction is shown). The deflection of the structure is 12.80 mm with the weight $m = 4 \times 0.55317 \text{ kg} \approx 2.21 \text{ kg}$.

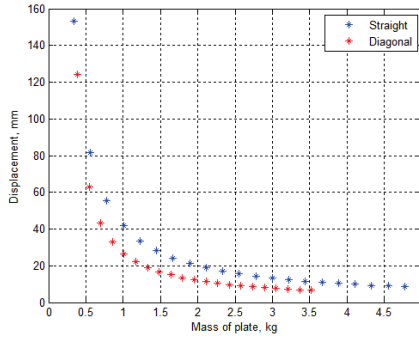


Fig. 4. Dependence of the deflection on the total mass of the plate for the straight and diagonal gratings.

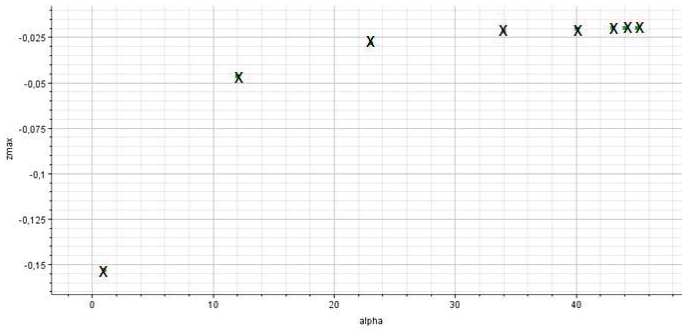


Fig. 5. The dependence of the deflection of the plate on the angle of inclination of the edges to the Ox axis.

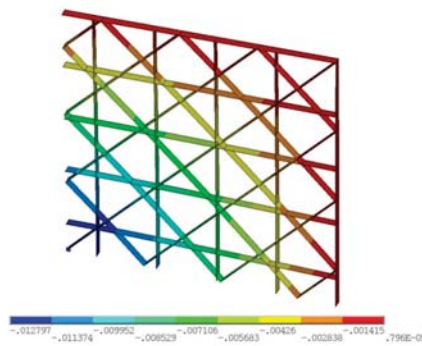


Fig. 6. Plate with additional horizontal ribs.

Figure 7 shows the dependence of the deflection of the structure with the increase in the number of straight edges at the fixed number of diagonal ones (36). Then we have studied the variation of the inclination angle of the ribs in the plane of the Oxy plate. For $\beta = 0$, the edges

are perpendicular to Oxy; the values of $\beta > 0$ correspond to the inclination outward from the central edge. The central edge always remains normal to the Oxy plane; the value range $-70 \leq \beta \leq 70$ being considered. In Figure 8 the dependence of the inclination angle of the ribs β to the vertical is illustrated. The dependence has a different character with decreasing and increasing β ; the minimum of deflection (9.61 mm) in this range of angles is reached when $\beta = -70$ (Fig. 9). The dependences obtained are asymmetric, since in the constructed model the edge rotation occurs around the lines lying in the Oxy plane, but not around the midline. However, this does not affect significantly on the results. It should be noted that the structure weight increases with increasing angle β .

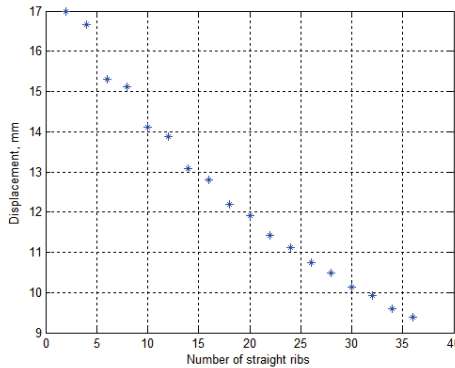


Fig. 7. Dependence of the plate deflection on the number of additional straight ribs.

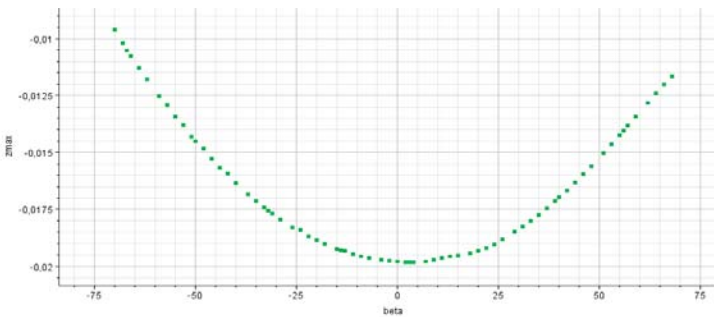


Fig. 8. Dependence of the deflection on the inclination angle of the ribs β to the vertical.

As the result of study, it was found that by changing the inclination angle of the ribs to the plate plane and by adding additional straight ribs, it is possible to obtain a deflection much less than in the initial configuration. It is obvious that the deflection can be reduced by simply increasing the number of diagonal ribs in the structure. Nevertheless, it is necessary to determine which of these three options is most effective. Figure 10 shows the dependence of the plate deflection on the slope angle of the edges at a constant mass of the plate.

The results indicate a low efficiency of the slope of the edges to the plate normal. In addition, it is seen that with a fixed mass, the best results are achieved in case 1, with a large number of diagonal ribs. However, the first point of graph 2 for a plate with additional straight

edges corresponds to a smaller deflection value than in case 1 for the same mass of the plate. This point corresponds to the configuration with two straight edges passing through the plate center.

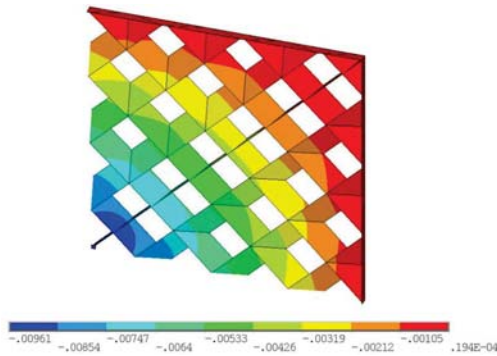


Fig. 9. Maximum deflection of the plate with the inclination angle of ribs -70° to the vertical in m.

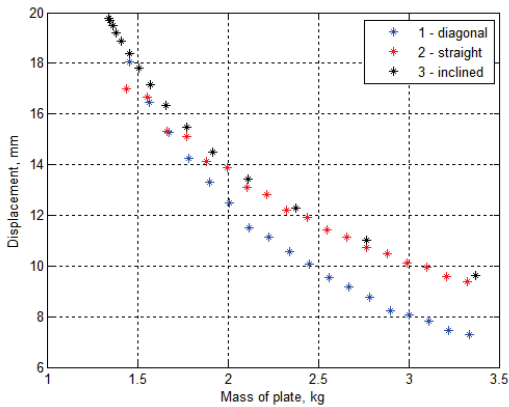


Fig. 10. Comparison of the dependence of plate deflection on the mass.

The solution of the parametric optimization problem is performed in the software modeFRONTIER. The geometrical model of the plate obtained during the optimization does not meet the technical requirements of the developed 3D printer. Therefore, an alternative version of the plate was designed to meet these requirements (Fig. 11). The presented configuration of the plate satisfies the limitations on the maximum deflection specified in the technical specification when the properties of a material determined by the results of full-scale tests of the samples; with the elements of the composite structure being consistent.

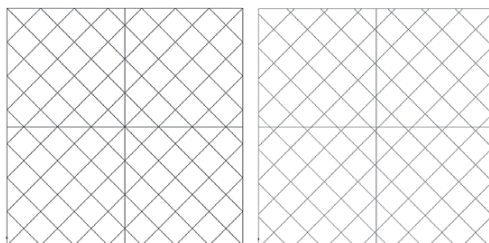


Fig. 11. Optimal and technologically-implemented plate configuration.

3. Full-scale experiment

The resulting plate configuration was printed on a developed 3D printer. Figure 12 shows the printing process and the printed plate. Virtual tests of the plate manufactured by 3D printing method is provided by the procedure of two-level submodelling described in Ref. [1] and correspond to full-scale tests carried out by the Testing Center «Polytest». The developed geometric and finite element models for the testing of the plate correspond to full-scale plate, taking into account the identified defects. In Figure 13, the full-scale test and the results of virtual tests are presented. The displacement values are reasonably close being 35.5mm in the case of full-scale test and 36mm in the case of virtual test.



Fig. 12. 3D printed lattice structure.

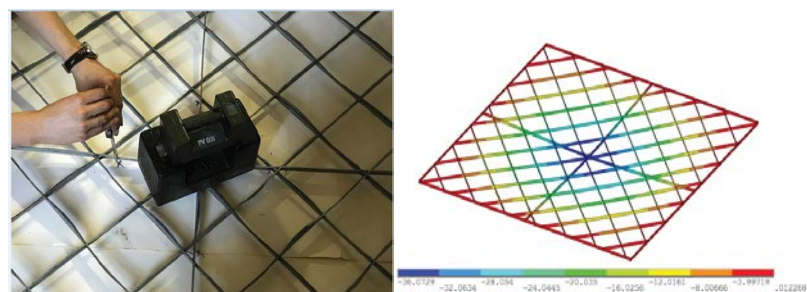


Fig. 13. Full-scale test and virtual test of plate

4. Conclusions

The parametric optimization of the lattice structure plate type is carried out. The dependences of the deflection and the first natural frequency on the plate mass are obtained, and a set of solutions optimal for the given criteria is determined. It is found that the minimum deflection is achieved at the inclination angle the ribs equal to 45° at a constant mass. There are strong grounds for believing that the variation of the inclination angle of the ribs to the plate plane is irrational.

Based on the results of solving the parametric optimization problem, among the quasi-optimal realizations, the variant with the maximum allowable deflection is selected. On the basis of multiscale simulations, an optimal configuration of the plate is designed and manufactured by 3D printer. The real-scale test results differ from the virtual nonlinear solution by 1%. The plate carried out the load; after removing the load the plate returned to its original configuration.

Acknowledgements

This work has been supported by RF Ministry of Education and Science (Contract No.14.581.21.0005, RFMEFI58114X0005).

References

- [1] X. Wang, M. Jiang, Z. Zhou, J. Gou, D. Hui, 3D printing of polymer matrix composites: a review and prospective // *Compos. Part B-Eng* **110** (2017) 442-458.
- [2] R.W. Gray, D.G. Baird, J.H. Bøhn, Thermoplastic composites reinforced with long fiber thermotropic liquid crystalline polymers for fused deposition modeling // *Polym. Compos.* **19(4)** (1998) 383-394.
- [3] Wenfeng Hao, Ye Liu, Hao Zhou, Haosen Chen, Daining Fang, Preparation and characterization of 3D printed continuous carbon fiber reinforced thermosetting composites // *PolymerTesting* **65** (2018) 29-34.
- [4] A.U. Zobacheva, A.S. Nemov, A.I. Borovkov, Multiscale simulations of novel additive manufactured continuous fiber-reinforced three-component composite material // *Materials Physics and Mechanics* **32** (2017) 74-82.
- [5] A.V. Chumaevskii, E.A. Kolubaev, S. Yu. Tarasov, A.A. Eliseev, Mechanical properties of additive manufactured complex matrix of three-component carbon fiber reinforced composites // *Key Engineering Materials* **712** (2016) 232.

VALIDATION OF EURONCAP FRONTAL IMPACT OF FRAME OFF-ROAD VEHICLE: ROAD TRAFFIC ACCIDENT SIMULATION

S. Alekseev*, A. Tarasov, A. Borovkov, M. Aleshin, O. Klyavin

Peter the Great St. Petersburg Polytechnic University, Polytekhnicheskaya 29

195251, St. Petersburg, Russia

*e-mail: alekseev@compmechlab.com

Abstract. The article is focused on the validation of the full-scale virtual model of a frame off-road vehicle. A high degree of coincidence with the real crash test according to EURONCAP rules is achieved. Modeling the processes of high-speed deformation and damage is a complex procedure, requiring a lot of input data parameters and large computing power. The special emphasis is placed on the ways to achieve the coincidence of the behavior of vehicle virtual elements with the behavior of car elements in the full-scale test.

Keywords: crash test, deformation, finite element, validation, vehicle.

1. Background

Frontal crashes of vehicles are responsible for more deaths and serious injuries than any other accident types. A typical scenario is a head-on collision between two oncoming cars at a moderately high speed. In the most collisions of this type, only a part of the vehicle front structure is involved, i.e. the two colliding vehicles are offset. In the full-scale test, the car is driven at 64 km/h with 40 percent overlap into a deformable barrier which represents the oncoming vehicle. The test replicates a crash between two cars of the same weight, both moving at 50 km an hour. Two frontal impact dummies representing the average males are seated in front of the car, child dummies being placed in child restraints in the rear seats.

In this crash, the vehicle structure is put to the test. Limited structural engagement can expose the occupants to increased intrusions. Crash forces have to be efficiently directed to the parts of the car where the energy can be efficiently and safely absorbed. The front crumple zone must collapse in a controlled way, leaving the passenger compartment undistorted as few as possible. Rearward movement of the steering wheel and the pedals must be limited if serious injuries are to be avoided. In Figure 1 the scheme of EuroNCAP frontal crash-test procedure is shown [1].

Computer simulation of traffic accidents is currently the predominant approach in the design of safe modern vehicles. Most of simulations of accident situations are accomplished virtually what allows accelerate developing a design of the cars, while the number of full-scale real experiments is reduced to a minimum. The full-size finite element (FE) model of a car is a complex structure which includes millions of elements; dozens of material models and thousands of different compounds what implies a high complexity of repeating the full-scale real test. Therefore, the first step after the model is created is the detailed comparison of the virtual simulation results with the full-scale test and step-by-step validation [2].



Fig. 1. Scheme of EuroNCAP frontal crash-test procedure.

2. Modeling

The complexity of this work and the difference from other works in this area lies in the lack of initial data; the industrial partner at the beginning of the work did not transfer all the necessary data, such as mathematical models of materials, kinematics parameters of chassis connections, airbags and belts FE models etc, therefore, the model validation procedure was developed in conditions of a lack of original data. In spite of this a good correlation of virtual and real experiment results is achieved.

As a result of modeling the “smart digital twin” was created;– the model which includes all the necessary parameters for prediction of object behavior during any physical interaction. “Smart digital twin” is the integral part of the digital factory, the complex of processes with the aim of achieving the new level of designing products, structures and approaches to production through the effective use of the entire complex of multi and transdisciplinary technologies of the world level.

The production of 2016 four-door passenger SUV was used as the basis for the model. CAD-models of the full vehicle were provided by the customer. Each part was meshed to create a representation of geometry models for finite element modeling that reflected all structural and mechanical features in a digital form. The parts were broken down into elements in such a way that critical features were consistent with the implications of element size on simulation processing times. Material characteristics data for the structural components were obtained through testing real samples. Based on material testing, appropriate stress, strain and damage values were included into the model for analyzing the crush behavior in a crash simulation. The experiment results were provided by the customer.

The resulting FE vehicle model has 3 million elements. This detailed FE model was constructed to include the full functional capabilities of a suspension, a driveline and steering subsystems. The representation of the model in comparison with the actual vehicle is shown in Figures 2 and 3. The set of elements representing the vehicle was translated into an FE model by defining each as a shell, a beam, or a solid element in accordance with the requirements for using LS-Dyna software. As the result of these efforts, the finite element vehicle model was designed with the following characteristics: number of parts 3544, number of nodes 3 million, and number of elements 3 million. The average element size used is 8 mm with a minimum size of 4 mm.



Fig. 2. Actual vehicle.



Fig. 3. Full scale FE representation.

Modeling detailed all the components of an off-road car. Figure 4 provides the bottom view of the vehicle model. The engine is modeled with a coarser mesh, because the previous simulation experience has shown that it reacts as a large rigid mass in crashes. It is modeled with external shell elements and mass elements having weight and inertia the same as the actual engine. The limp mass representation of the engine and the suspension elements can also be incorporated into the model.

Figures 5 and 6 illustrate the view of the modeled front and rear suspension systems. The moving parts are detailed to provide the capability for simulating suspension and steering responses. All inner components of the front and rear doors are incorporated into the initial version of the model and are presented in Figure 7. Structural components of the vehicle interior are included in the initial version of the model and shown in Figure 8.

To estimate the injuring criteria of a driver and a passenger according to Euroncap requirements, the model includes validated commercial models of Hybrid-3 50% dummies corresponding to the actual experiment. Figure 9 shows the FE model of dummies.

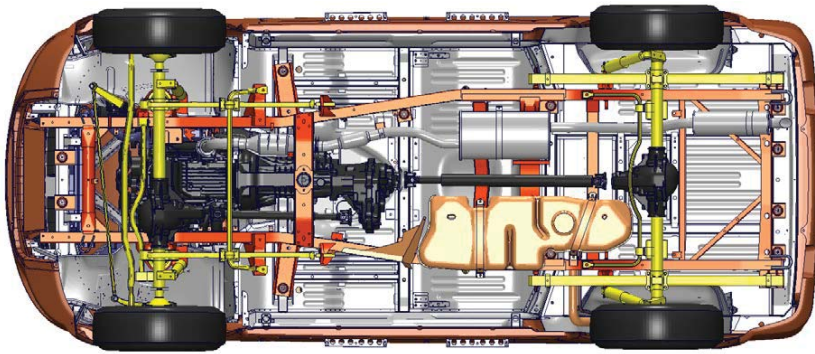


Fig. 4. Vehicle model bottom view.

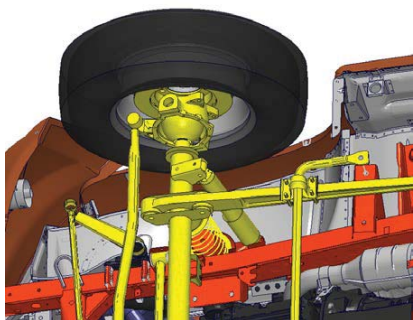


Fig. 5. Modeled front suspension.

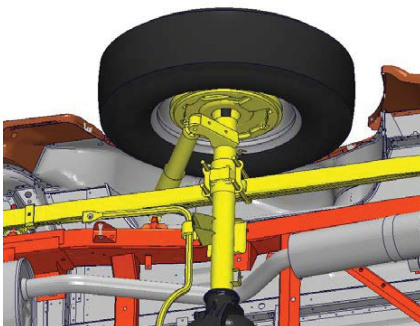


Fig. 6. Modeled rear suspension.



Fig. 7. Details of interior door components.

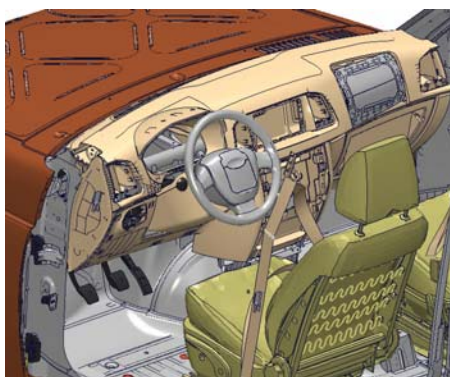


Fig. 8. Coarse representation of structural interior components.

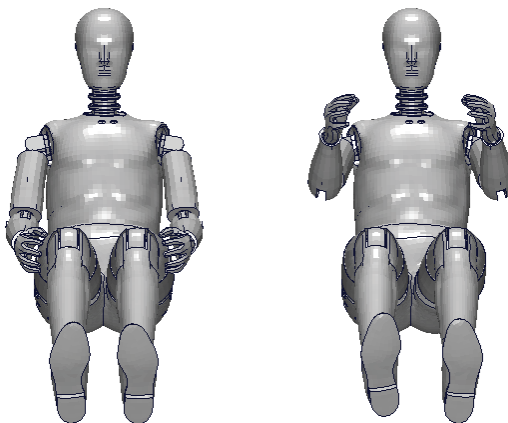


Fig. 9. FE models of driver and passenger dummies.

3. Model validation

The FE model was validated in various ways to make sure that it was an accurate representation of the actual vehicle [3, 4]. The initial efforts included checks for completeness of elements and adequacy of connection details. The measured properties at customer location for the vehicle were compared to those generated from the FE model. The results are given in Table 1.

Table 1. Comparison of measured properties of actual and modeled vehicle.

Property	Actual Vehicle	FE model
Weight, kg	2308	2308
Vehicle COG Z, mm	802	802
Vehicle COG X, mm	1492	1492
Clearance, mm	210	210
Width (without mirrors), mm	1900	1900
Length, mm	4785	4785
Height, mm	2005	2005
Wheelbase, mm	2760	2760

The FE model EuroNCAP simulation was performed using the LS-DYNA non-linear explicit finite element code. The FE vehicle model was run using LS-DYNA Code. The FE model response would be expected to vary for other facilities depending on hardware, LS-DYNA version, and precision used. The variations are typically minimal and the results from the different versions are comparable. The total duration of the simulation was 200 ms to capture the initial impact until the rebound of the vehicle from the EuroNCAP load.

Due to the lack of data provided by the manufacturer, the first virtual tests according to the EURONCAP rules had a low degree of correlation with the full-scale crash test. The following data were not provided:

- results of testing plasticity and damage of a car body and frame materials, taking into account viscous properties and high-speed deformations curves;
- stiffness and damping curves of kinematic connections in suspensions;
- shock absorber behavior data;
- kinematic parameters of the engine, gearbox and cardan;
- virtual model of airbags and seat belts./

To select appropriate material models, a series of crash simulations was performed in order to achieve deformation coincidence. The customer provided the material models that do not take into account high-speed hardening; therefore, at high strain rates, deformations significantly exceeded the values reached in the actual EuroNCAP test.

Figure 10 shows deformations for a body with materials that do not take into account high-speed hardening. Fig. 11 shows body deformations with selected material from the database of contractor, with strain-stress curves for high-speed deformations. For comparison Fig. 12 shows deformation from actual crash impact. As a result of the multivariant optimization, it was possible to achieve a similar character of deformation of the frontend, the body sill, and the doors of the off-road vehicle.



Fig. 10. Deformation with customer material models.



Fig. 11. Deformation with optimized material models.



Fig. 12. Deformation in actual crash-test.

One of the features of the vehicle crash test is the rotation of the front wheel, and its subsequent intrusion into the car floor with subsequent disruption of the living space integrity for a driver and passengers. With the view of simulating this effect correctly, a detailed multivariate adjustment of parameters of the front suspension and front axle of the off-road vehicle in the kinematic MBS (Multi Body System) model was performed, and then all the chosen parameters were transferred to the full-scale LS-Dyna FE model. The adjusted front suspension model includes all the kinematic parameters of the bushings, wheels and suspension. Figure 13 shows the performed tests of the front suspension in MBS model. Figure 14 and 15 shows the position of the wheel in 150 ms in the model with unconfigured suspension and in the model with the adjusted suspension.

Virtual model of airbags and seat belts were not provided by customer, so they were adjusted according to EuroNCAP test results. In Figures 16 and 17 one can see comparison of driver airbag behavior in simulation and in the actual test at the moment of head collision with surface of airbag on 90 ms. Figure 18 exhibits the side view of the frontal deformations taken at five intervals during the impact. It can be noted that the actual and simulated views reflect similarity at each time point.

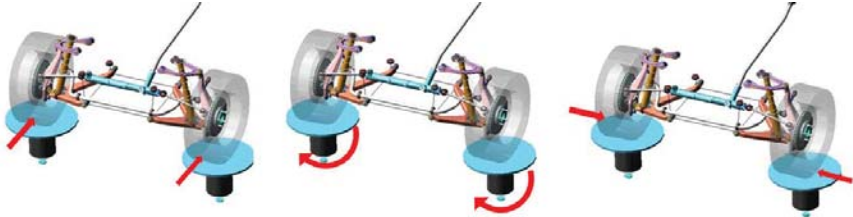


Fig. 13. Frond suspension MBS model adjusting.

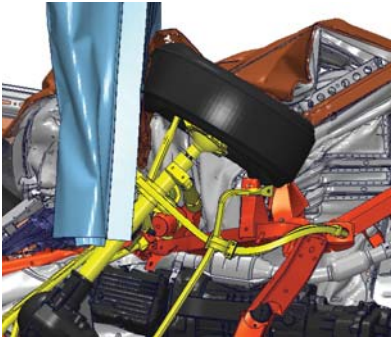


Fig. 14. Front suspension behavior during the initial virtual crash-test.

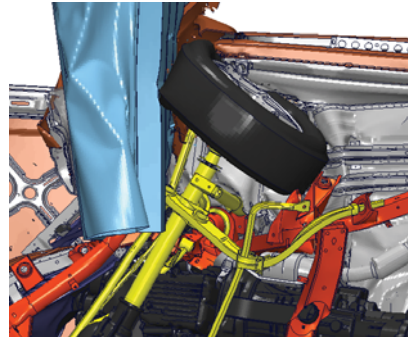


Fig. 15. Front suspension behavior during the virtual crash-test with adjusted and configured parameters.



Fig. 16. Collision of dummy head with airbag, virtual crash-test 90 ms.



Fig. 17. Collision of dummy head with airbag, actual crash-test 90 ms.

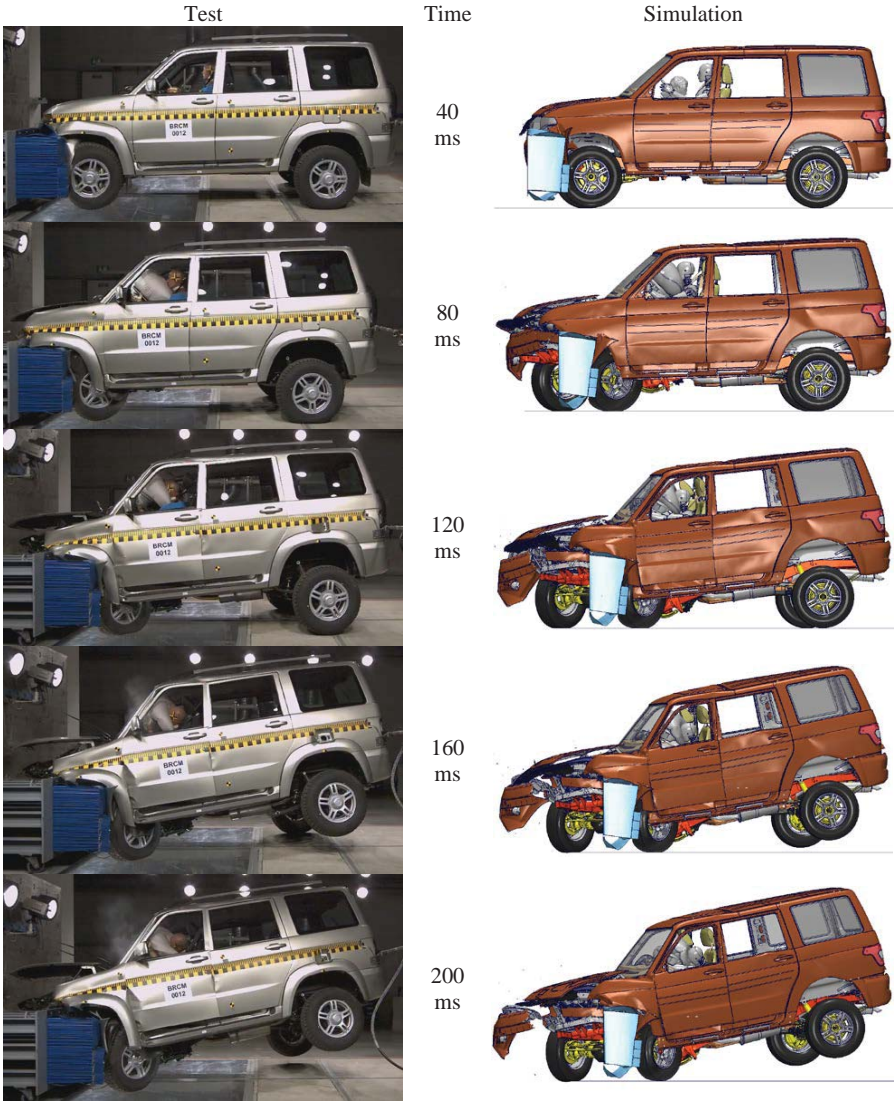


Fig. 18. Sequential side views of the actual and simulated EuroNCAP frontal deformable barrier test for the off-road frame vehicle.

The side view shows a high degree of deformation coincidence of the vehicle front part. In both cases the hood does not interact with the barrier and ejects forward due to high inertial forces. The fenders and front part of car body have almost identical deformations. The rear part of the vehicle rises up in both tests due to the high position of center of gravity.

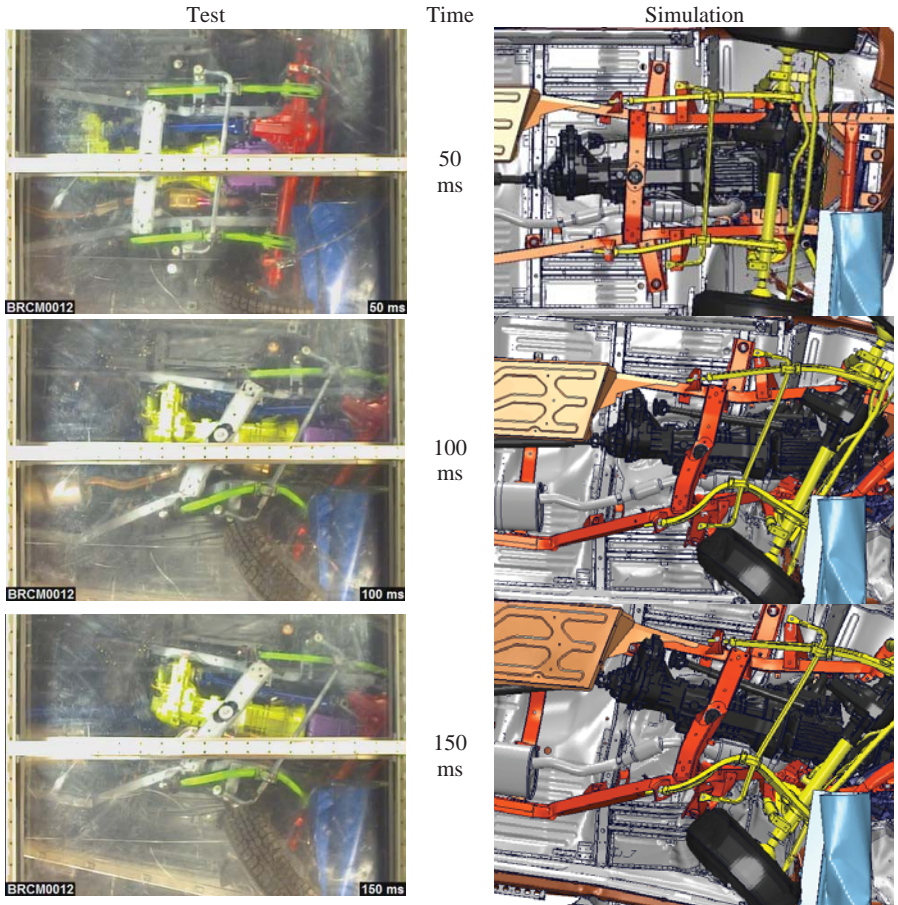


Fig. 19. Sequential bottom views of the actual and simulated EuroNCAP Frontal deformable barrier test for the off-road frame vehicle.

Figure 19 shows the bottom view of the frontal deformations taken at three intervals during the impact. There is a high degree of coincidence of frame deformations in full scale and virtual tests. One can see that fractures appear in the same places, the deformation paths have a similar pattern, the fastening point between the torque divider and the front cardan is broken in both cases, and the same support damage between car body and frame can be noticed. In both cases, the front wheels rotate with the subsequent destruction of the car body floor and a breakdown of the integrity of the living space of a driver and passengers.

Figure 20 illustrates the top view of the frontal deformations taken at three intervals during the impact. The top view for full scale and virtual tests demonstrate the same turning angle of the vehicle after the impact, the similar picture is for opening the hood and deformation of the left wing.

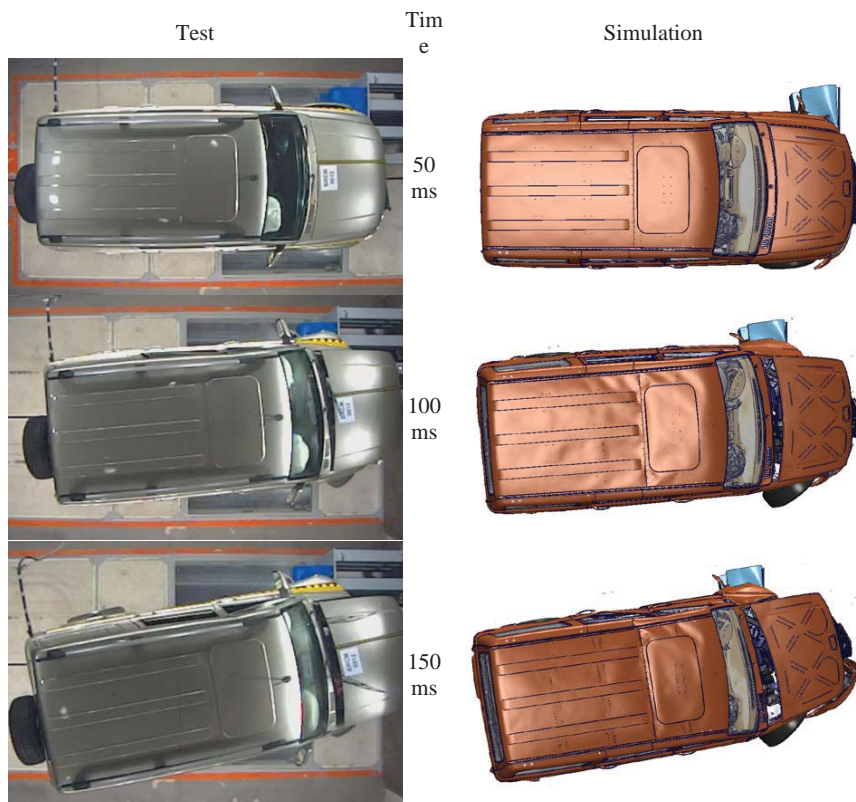


Fig. 20. Sequential top views of the actual and simulated EuroNCAP frontal deformable barrier test for the off-road vehicle frame.

4. Summary and conclusions

A FE model of the 2016 passenger SUV was created and validated using LS-Dyna solver. Modeling led to a detailed model that consists of 3 million elements, includes all vehicle structural and interior components, and has functional representations of the steering, suspension and driveline systems. A multistage process of selecting the missing characteristics was carried out. As a result of the iterative process of validation of off-road vehicle model, a high degree of coincidence with the full-scale test is achieved. Missing characteristics of SUV were selected and fitted during the validation process, the selected characteristics showed a sufficient degree of correlation. The final model will be used to conduct virtual tests to determine the passive safety according to EURONCAP rules in the process of developing the off-road vehicle for future production.

The model was validated by comparison to images and data derived from the customer, which involved actual frontal impact into a deformable barrier at 64 km/h according to EuroNCAP rules. Comparisons of data from the test and the model included:

- Measurements checks : length, width, height, clearance and wheelbase;
- Weight and coordinate of gravity center;

- Deformation of car body and frame from side, bottom and top views;
- Wheel rotation during the impact with subsequent intrusion to the living space of a driver and a passenger;
- Behavior of front suspension and front axle during the process of impact

All the comparisons showed overall good correlation with the physical test results. Validated model is approved by the manufacturer and will be used as the basis in further frontal impact virtual tests during the development of a new off-road vehicle.

Acknowledgements

The works are carried out during the implementation of the comprehensive project with the financial support of the Government of the Russian Federation (Ministry of Education and Science of Russia). Contract 02.G25.31.0140 of 01.12.2015.

References

- [1] Offset deformable barrier frontal impact testing protocol Euroncap (November 2015) Version 7.1.1.
- [2] Concepts of model verification and validation (Los Alamos National Laboratory, LA-14167-MS? October 2004).
- [3] D. Marzougui, D. Brown, H.K. Park, C.D. Kan, K.S. Opiela, Development and validation of a finite element model for a mid-sized passenger sedan, In: *13th International LS-DYNA Users Conference*.
- [4] M. Mongiardini, M.H. Ray, R. Grzebieta, M. Bambach, Verification and validation of models used in computer simulations of roadside barrier crashes, In: *Proceedings of the 2013 Australasian Road Safety Research, Policing & Education Conference*.

NVH ANALYSIS OF OFFROAD VEHICLE FRAME. EVALUATION OF MUTUAL INFLUENCE OF BODY-FRAME SYSTEM COMPONENTS

A. Patrikeev*, A. Tarasov, A. Borovkov, M. Aleshin, O. Klyavin

Peter the Great St. Petersburg Polytechnic University, Polytekhnicheskaya 29

195251, St. Petersburg, Russia

*e-mail: patrikeev@compmechlab.ru

Abstract. The article focuses on the basic NVH characteristics of a vehicle such as global static stiffness, eigenfrequencies and local dynamic stiffness. We built the Smart Digital Twin of serial SUV that allow reduce the time and costs of the design stage by reducing the number of real tests. The optimal target values of static stiffness for the Frame and BIW were selected to achieve the target static stiffness of the Trimmed body.

Keywords: finite element, frame, frequency, stiffness, vehicle.

1. Introduction

In the modern world people spend a lot of time in a vehicle, so vibro-acoustic comfort in a car plays a very important role, influencing the customer product satisfaction and, although not directly, on safety, reducing driver tiredness. Term NVH unites a complex of characteristics related to behavior of the vehicle structure under the operating loads and responsible for vibro-acoustic perception by human senses. During the development of new vehicles, it is always required to work out the tasks of improving the design effectiveness, i.e. to find the best compromise between high level of safety, light weight, fuel efficiency, reliability and such customer demands as perfect handling, vibro-acoustic comfort, load carrying capacity etc.

In body-on-frame vehicles much attention is paid to the frame as the main load-bearing part, which is a support for the powertrain, suspension and body. In the case of body-on-frame SUV, there are two separate subsystems, the frame and the body, which are designed usually by separate departments. Each system has its own individual characteristics, which change when the systems become the parts of an assembly.

In this paper we present the results of our work for the new body-on-frame SUV. Its predecessor, the serial SUV, was used as the basis for analysis. In order to completely switch to digital design in the new paradigm of Digital factories, we built the Smart Digital Twin of serial SUV, that will allow reduce the time and costs of the design stage in future, by reducing the number of real tests. The final purpose of the work is: having the target levels for selected characteristics on a trimmed body, to cascade them down to the lowest levels and to issue target values for individual subsystems, the Frame and the Body, with the purpose of using in the respective departments. The analyzed objects, Smart Digital Twins of the Frame, the Body and the Trimmed body are shown in Figure 1. The new vehicle design based on the Smart Digital Twin validated by results of our work; make us convinced the digital design will give us the results that will match the acceptance tests.

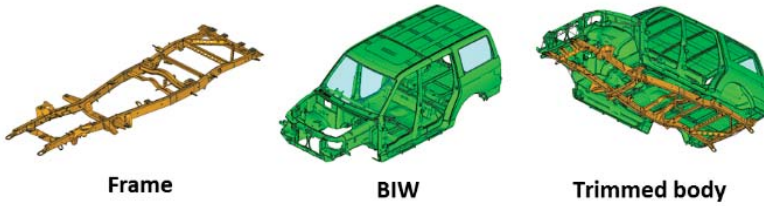


Fig. 1. Analysis objects.

2. Static and dynamic stiffness analysis of body-on-frame SUV

One of the design effectiveness key indicators is the static and dynamic stiffness. Static stiffness of the frame is mainly defined by its global torsional, vertical and lateral stiffness. The torsional and vertical stiffness of the frame plays big role in isolating PWT and road vibrations and load carrying capacity of a vehicle. The lateral stiffness of the frame is very important for appropriate handling and cornering ability of the vehicle.

Dynamic stiffness of the frame is mainly defined by its global eigenfrequencies and local dynamic stiffness (LDS), and also plays major role in isolating main sources of noise and vibrations. The eigenfrequencies of the frame should be as high as possible and be decoupled with frequencies of harmonic excitations of such systems as PWT, chassis, fans etc. The local dynamic stiffness should be high enough to provide good filtration of rubber mounts. Because of the similarity of approaches, static stiffness is represented by the example of torsional stiffness, modal analysis by the example of torsional mode, local dynamic stiffness by the example of powertrain mounts only.

Static stiffness. To define the torsional static stiffness of the trimmed body, the frame is loaded with a twisting moment, and twisting angle of the BIW is evaluated (Fig. 2). To define the torsional static stiffness of the trimmed body, the frame is loaded with a twisting moment, and twisting angle of the BIW is evaluated (Fig. 2).

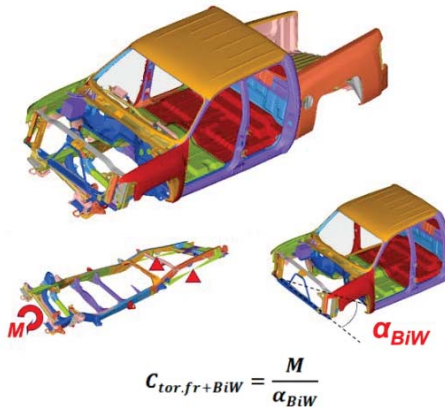


Fig. 2. Torsional stiffness of the trimmed body evaluation test scheme.

Torsional static stiffness of the yrimmed body is the ratio of twisting moment (applied to the frame) to twisting angle of the BIW. This characteristic is included in the vehicle technical

requirement list. It is useful for the structure analysis to make a plot of twisting angles along the BIW length as shown in Figure 3.

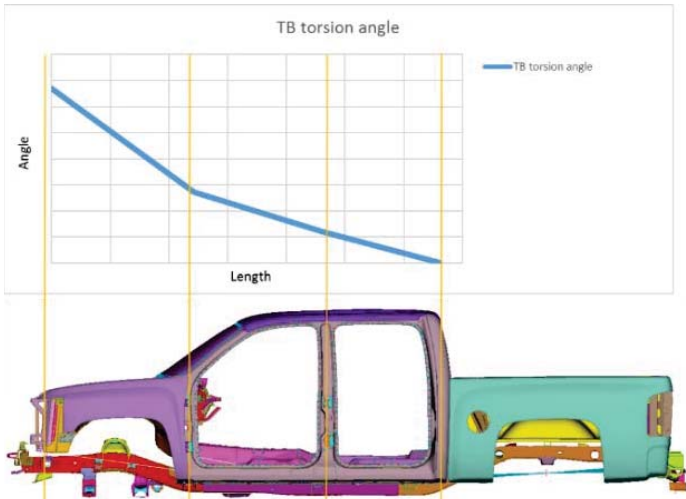


Fig. 3. Example of the plot of twisting angles along the BIW length.

Modal analysis. The lowest eigenfrequencies of the trimmed body are defined to decouple them with the eigenfrequencies of unsprung masses and the frequencies of engine idle vibrations (Fig. 4).

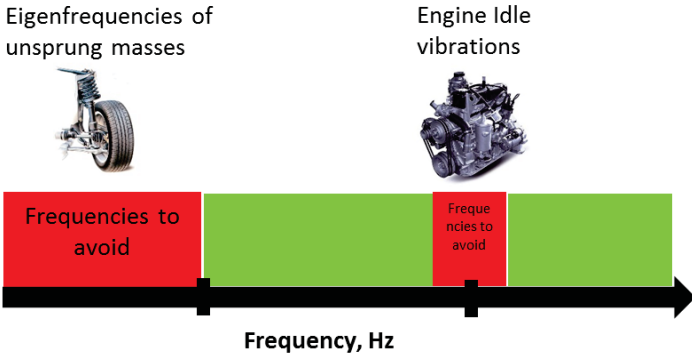


Fig. 4. Global eigenfrequencies to avoid scheme.

Local dynamic stiffness of the rubber mounts installation zones is evaluated to ensure good filtration. Local dynamic stiffness of Frame/BIW in the rubber mounts installation zones should be several times higher of the respective rubber stiffness (Fig. 5).

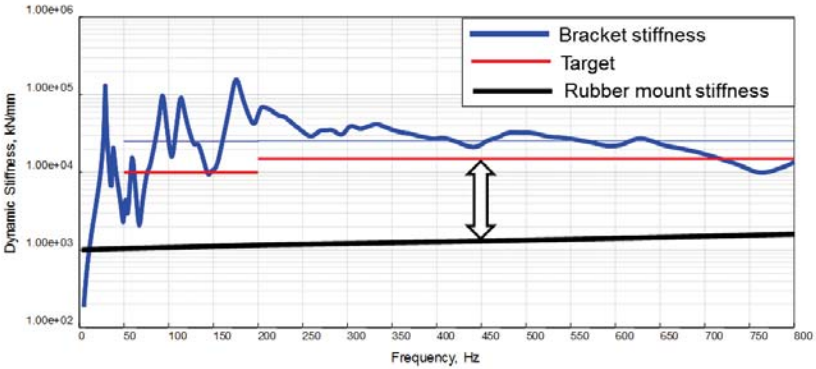


Fig. 5. Example of the local dynamic stiffness targeting.

3. Simulations results

Static stiffness results. Plot of twisting angles of the BIW (as part of the trimmed body) of the Serial SUV Smart Digital Twin is presented in Figure 6. The point marks the twisting angle corresponding to the target stiffness. The dotted line is the relative level below which all the twisting angles of the BIW as part of trimmed body must be. The continuous line demonstrates the simulation results. It is seen from the plot that the part corresponding to twisting the front end does not meet the target level. This is due to the concept of body-on-frame construction; the frame receives all the main loads, so the body needs no power elements such as longerons in the front end. This should be taken into account assigning target stiffness for the frame and the body individually.

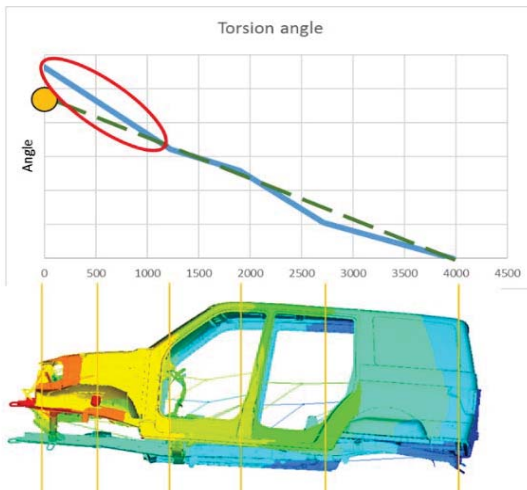


Fig. 6. Plot of twisting angle of the serial SUV Smart Digital Twin.

Modal analysis results show the following dynamics.

The lowest eigenfrequencies of the frame as part of trimmed body are higher in comparison with those of the individual frame by 10 Hz. This is explained by the change of boundary conditions (elastic contact with “heavy” body) at slight change in mass.

The lowest eigenfrequencies of the BIW as part of trimmed body are lower in comparison with those of the individual BIW by 7 Hz. This is explained by a minor change of boundary conditions (elastic contact with “light” frame) at significant increase in mass, because the mass of such components as openings and trims is included in the trimmed body.

The dynamic changes schematically are shown in Figure 7. The changes should be taken into account, when assigning target values of the lowest eigenfrequencies for the frame and the body individually, in order to eliminate the coupling between the frequencies of the frame and BIW with each other as well as with engine idle vibrations on the trimmed body.

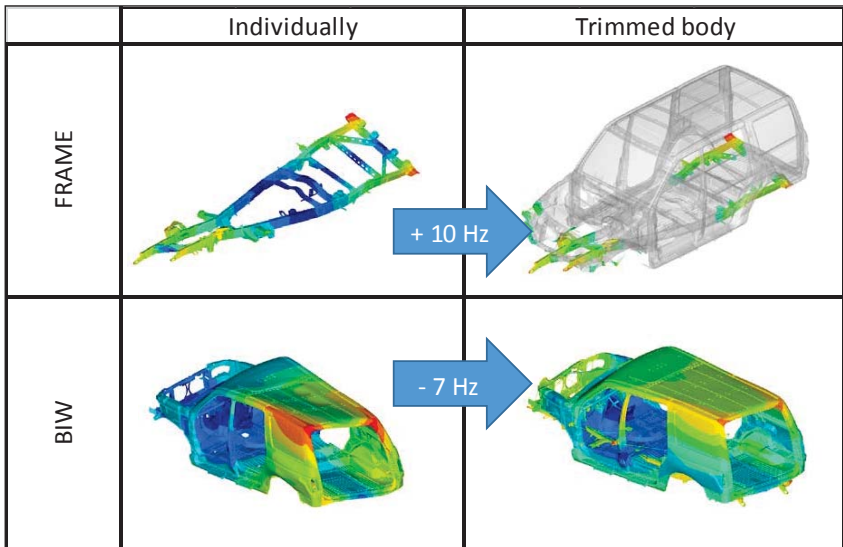


Fig. 7. Dynamics of eigenfrequency change at switching from the individual frame and BIW to the trimmed body.

Local dynamic stiffness of the powertrain mounts was calculated in the frequency range from 0 to 800 Hz. The calculations were done for the frame and the trimmed body. The results were averaged for low and medium frequency ranges. The difference between averaged results for frame and trimmed body is shown in Table 1. We see that differences are:

- maximum 3.8 % for the low frequency, that is significant;
- maximum 0.5 % for the medium frequency, that is insignificant.

The reason is that with increasing frequency the wavenumber (the number of waves in a specified distance) increases too; thus mode shapes become more localized and the frame boundary conditions have less influence on the results.

Table 1. Local dynamic stiffness on the Frame and on the Trimmed body comparison.

Point	Units	Dir.	Difference between component in separately and in assembly, %	
			Low freq.	Mid. Freq.
Engine left mount	N/mm	x	-3.8	0.0
		y	2.6	0.2
		z	-0.7	0.2
Engine right mount	N/mm	x	-3.5	0.1
		y	1.4	0.0
		z	1.2	0.1
Gearbox mount	N/mm	x	1.4	-0.1
		y	-1.5	-0.5
		z	0.5	-0.2

4. Conclusion

The optimal target values of static stiffness for the Frame and BIW were selected to achieve the target static stiffness of the Trimmed body. The optimal target values of lowest eigenfrequencies of the Frame and BIW were selected to eliminate the coupling between the frequencies of the frame and the body with each other and with engine idle vibrations on the trimmed body. From the results of LDS analysis we can conclude that in the absence of full Trimmed body model it is possible to make first estimations of LDS on the Frame. However, when the Trimmed body model is available it is necessary to update the results for the low frequency range.

Acknowledgements

The work is carried out during the implementation of the comprehensive project with the financial support of the Government of the Russian Federation (Ministry of Education and Science of Russia). Contract 02.G25.31.0140 of 01.12.2015.

References

- [1] P. Kurisetty, N. Sukumar, U. Gupta, Parametric study of ladder frame chassis stiffness // *SAE Technical Paper* 2016-01-1328 (2016). doi:10.4271/2016-01-1328.
- [2] S. Mooherjee, V. Katkar, Integrated cost reduction of a light truck frame – design approach // *SAE Technical Paper* 2007-01-4166 (2007). doi: 10.4271/2007-01-4166.
- [3] E. Sampo, A. Sorniotti, A. Crocombe, Chassis torsional stiffness: analysis of the influence on vehicle dynamics // *SAE Technical Paper* 2010-01-0094 (2010). doi:10.4271/2010-01-0094.

INTEGRATED SYSTEM AS A TOOL FOR IMPLEMENTATION OF SIMULATION- AND OPTIMIZATION-BASED DESIGN METHODOLOGY

Aleksei Novokshenov*, Alexander Nemov, Dmitriy Mamchits, Aleksandra Zobacheva

Peter the Great St. Petersburg Polytechnic University, Polytekhnicheskaya 29

195251, St. Petersburg, Russia

*e-mail: novokshenov@compmechlab.ru

Abstract. Within the framework of the work, topology optimization program module and integrated computer-aided design and engineering system are developed. Topology optimization of bracket and parametric design optimization of space waffle shell were carried out through ISCDE. The obtained results will be used in the Russian space companies.

Keywords: design, modeling, space bracket, topology optimization.

1. Introduction

Today in the world design engineering practice two approaches to design of structures can be distinguished. The first, more traditional, is that the designer on the basis of operational requirements and his experience invent a sketch of the structure, which then turns into a CAD-model. After that, a real prototype is created and full-scale tests are carried out. CAE calculations are also performed, mainly to verify those loading cases that have not been tested in full-scale tests. In case of dissatisfaction with some requirements, the model is returned to the designer, and the loop is repeated.

With the traditional approach, the engineers use other approach based on mathematical modeling and optimization methods. Using this approach, called simulation- and optimization-based approach, allows one to get a design of structure under specified operating conditions through the use of computer simulation and optimization. This approach is currently being implemented by leading Western industrial companies in the development of new aircraft, ground vehicles, etc. A key role in this approach is topological optimization, allowing for predetermined loads to predict the most effective material distribution in structure.

This work is devoted to the development of a tool for implementing the design approach based on mathematical modeling and optimization. The work includes the development of an integrated computer design and engineering system, a topological optimization module in the ANSYS APDL environment, and demonstrates obtained solutions.

2. Topology optimization program module

The problem of topology optimization, in the classical formulation, is the problem of choosing the optimal distribution of material in fixed space (Fig. 1). For each point of the body, we should answer the question whether there is material in this place or not. To look at this initially discrete problem as on the continuous problem we use the SIMP (Solid Isotropic Material with Penalization) method, which allows associate the elastic properties of a material with an additional parameter called "density" [1].

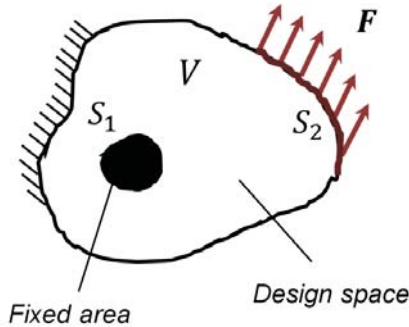


Fig. 1. Formulation of topology optimization problem.

$$E(x) = \rho(x)^p E^0 \quad (1)$$

In ANSYS APDL, this was implemented by assigning each finite element its own material. The further task is to achieve a minimum of the functional of external forces work, when the equilibrium condition of the system is satisfied.

$$\begin{aligned} & \min_{\mathbf{u} \in U, E} A^{ex}(\mathbf{u}) \\ \text{s.t.} \quad & A^{ex}(\delta \mathbf{u}) = \delta \left(\rho_r \psi(\boldsymbol{\varepsilon}(\mathbf{u})) \right), \forall \delta \mathbf{u} \in U \\ & V \leq \alpha V_0, 0 < \alpha < 1 \end{aligned} \quad (2)$$

For this goal, we use the Method of Moving Asymptotes (MMA) [2]. This method now is used in most popular world optimization software, like Altair Optistruct and DS Simulia Tosca Structure [3, 4]. To apply this method, it is necessary to define the partial derivatives (sensitivities) of an object with respect to design variables. In the case of minimizing the compliance of the system with a constraint on the volume, these derivatives are related to the potential deformation energy at each point.

$$\frac{\partial c}{\partial \rho_e} = -\mathbf{u}^T \frac{\partial \mathbf{K}}{\partial \rho_e} \mathbf{u} = -p \rho_e^{p-1} \bar{\mathbf{u}}^T \mathbf{K}_0 \mathbf{e} \mathbf{u} \leq 0 \quad (3)$$

In ANSYS APDL, the procedure for finding sensitivities is consist in performing FE calculation and obtaining the strain energy in each finite element. After that, a convex approximation of objective function is analytically constructed [3]:

$$c^{(k)}(\boldsymbol{\rho}) = c(\boldsymbol{\rho}^{(k)}) - \sum_{j=1}^n \frac{(\rho_e^{(k)} - L_e^{(k)})^2}{\rho_e - L_e^{(k)}} \frac{\partial c}{\partial \rho_e}(\boldsymbol{\rho}^{(k)}) + r^{(k)}(\boldsymbol{\rho}^{(k)}) \quad (4)$$

Minimum of this function can be easily determined by constructing a Lagrangian functional and solving dual optimization problem. The founded solution is the next calculation point for the approximation. The iterative process is repeated until the results converge.

The mapping of optimization results was performed by the exclusion those finite elements, which density parameter is lesser a specified level. To ensure the possibility of the designer to work with obtained optimal not-smooth finite-element model, the postprocess procedure based on the Laplacian smoothing algorithm is carried out. This algorithm was implemented in ANSYS ADPL program module by triangulation of the surface of the optimized finite element model, and further iterative process of averaging the vertices coordinates of neighboring finite elements (Fig. 2).

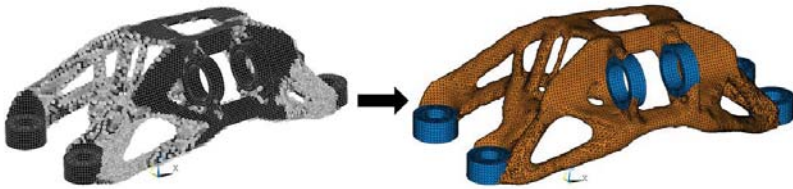


Fig. 2. Laplacian smoothing as a postprocess tool.

Additionally, the mesh density filter was implemented to the program module in order to prevent an appearance of «checkboard» (Fig. 3).

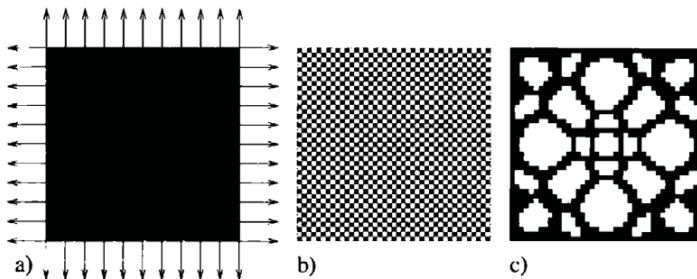


Fig. 3. Checkboard effect [3] a) original task; b) result without filtering; c) result with filtering.

Mesh density filter is based on operation of weighted averaging of sensitivities in the area of initially defined radius r_{min} :

$$\frac{\partial c}{\partial \rho_e} = \frac{1}{\rho_e \sum_{i=1}^N \bar{H}_i} \rho_e \sum_{i=1}^N \bar{H}_i \rho_i \frac{\partial c}{\partial \rho_i}, \quad \bar{H}_i = r_{min} - dist(e, i) \quad (5)$$

The developed topology optimization module shows good consistency with the results given in Ref. [6] and shown in Figure 4.

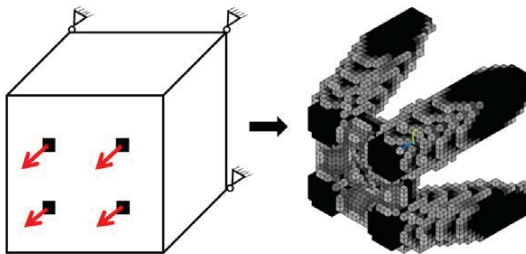


Fig. 4. Results of topology optimization for solid block with developed program module (Minimizing compliance with volume fracture 20 %).

3. Integrated system of computer design and engineering (ISCDE)

For conception simulation- and optimization- based design, only the topological optimization is not enough. This approach requires the following functionality:

1. For optimization of structure one needs to know the layout volume, interface elements, and functionality of design structure. For this you need a hierarchical database of structures. This database should also contain information about all loading conditions for structure.
2. Both for structural or parametric optimization, one needs to know the technological limitations - this requires a technology database.
3. To perform engineering and optimization calculations of structures, a database of materials, available for design engineer, is needed.
4. To ensure simultaneous access of specialists of all profiles and levels to the design process, the system should have a client-server architecture.
5. In order to cover all nuances of design behavior in simulation, the system should integrate the best world modeling and optimization solutions: ANSYS, DS Simulia ABAQUS, MSC NASTRAN, Alatair Optistruct, DS Simulia Tosca Structure, Esteco modeFrontier. The system also will integrate the developed topological optimization ANSYS APDL module (for case, if company have no optimization software).
6. The system should have automated postprocess tools to track the specified target values for part or for assembly during simulations.

All this was implemented in the integrated computer design and engineering system (ISCDE) (Fig. 5).

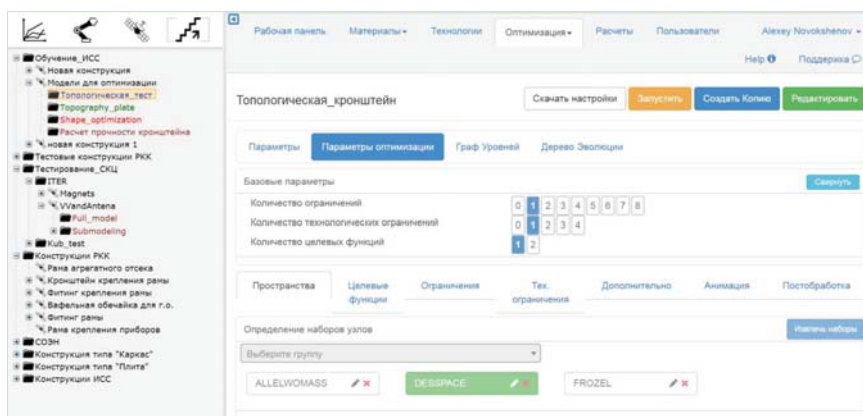


Fig. 5. ISCDE interface in case of optimization with DS Simulia Tosca Structure.

The developed system has a server and a client part. The server part is written in JAVA, the client in JavaScript, the used database is PostgreSQL. The system includes a tree of materials (homogeneous and composite), a tree of technologies, a hierarchical tree of constructions, and the calculation and optimization module. The system implements User Account Control (UAC). Figure 5 shows the interface of the system (available through the web-browser) when optimizing the design in DS Simulia Tosca.

4. Examples

Topology optimization of the space bracket with Altair Optistruct through ISCDE was performed and shown in Figure 6. Mass reduction makes up 43%. The bracket was manufactured using the technology of titanium 3D printing. For optimal design all restrictions (such as stress safety factors, natural frequencies) are satisfied.

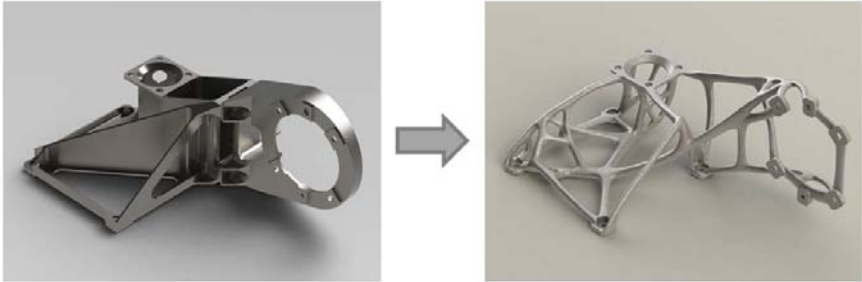


Fig. 6. Topology optimization of space bracket.

Parametric design optimization of space waffle shell Parametric design optimization of space waffle shell with Esteco modeFrontier through ISCDE was performed and shown in Figure 7. Mass reduction is 32%. MOGAI algorithm was used. For optimal design all restrictions (such as stress safety factors, natural frequencies, buckling safety) are satisfied. The original shell is manufactured from aluminum billet by milling.

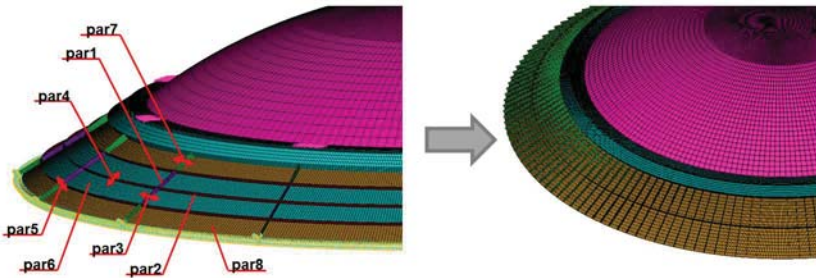


Fig. 7. Parametric design optimization of space waffle shell.

Topology optimization of stellar sensor bracket with Simulia Tosca Structure through ISCDE was performed and shown in Figure 8. Mass reduction is 60%. Topo Sensitivity algorithm, based on SIMP model and Method of Moving Asymptotes was used. For optimal design, stress constraint and first natural frequency are satisfied.

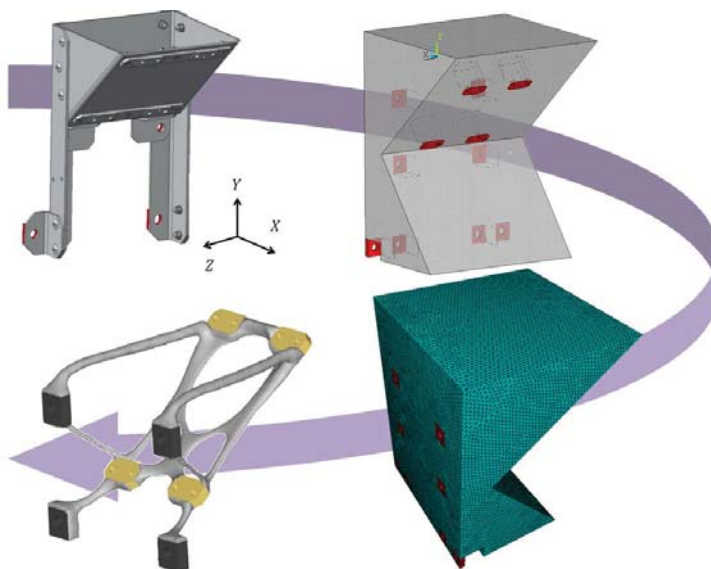


Fig. 8. Topology optimization of stellar sensor bracket.

5. Conclusion

Within the framework of the work, topology optimization program module and integrated computer-aided design and engineering system are developed. Topology optimization of bracket and parametric design optimization of space waffle shell were carried out through ISCDE. The obtained results will be used in the Russian space companies.

Acknowledgement

This work has been supported by RF Ministry of Education and Science (Contract No.14.581.21.0005, RFMEFI58114X0005).

References

- [1] M.P. Bendsoe, O. Sigmund, Material interpolation schemes in topology optimization // *Archives of Applied Mechanics* **69(9-10)** (1999) 635-654.
- [2] K. Svanberg. The method of moving asymptotes – a new method of structural optimization // *International journal for numerical methods in engineering* **24** (1987) 359-373.
- [3] *SIMULIA Tosca Structure Documentation* 8.0. Version 8.0 Rev. 1 - 10.2013. www.3ds.com/tosca.
- [4] *Altair HyperWorks* 14.0 Online Documentation
- [5] M.P. Bendsoe, O. Sigmund, *Topology Optimization. Theory, Methods and Applications* (Springer, 2003).
- [6] H. Eschenauer, N. Olhoff, Topology optimization of continuum structures: A review // *ASME, Applied Mechanics Reviews* **54(4)** (2001).

VEHICLE DYNAMICS PREDICTION MODULE

J. Leoro^{1*}, S. Krutitskiy¹, A. Tarasov², A. Borovkov², M. Aleshin², O. Klyavin²

¹ Compmechlab Ltd., Gzhatskaya 21/2 – 219, 195220, St. Petersburg, Russia

² Peter the Great St. Petersburg Polytechnic University, Polytekhnicheskaya 29

195251, St. Petersburg, Russia

*e-mail: leoro@compmechlab.com

Abstract. In this contribution we used the vehicle dynamics for creation a vehicle motion prediction module for autopilot tasks. A Vehicle Dynamics Prediction Module (VDPM) was created as an application for self-driving hardware assistance for high velocities maneuvering (above 40km/h). The dynamic characteristics of a vehicle have a complex mathematical mechanism, but have a regularity character. This fact allows us to create a basis with a limited number of pre-calculated maneuvers to describe the behavior of the vehicle dynamics for maneuvering in public roads.

Keywords: dynamics, modeling, prediction, trajectory, vehicle.

1. Background

Modern automotive industry is focused on self-driving vehicles and needs an appropriate virtual testing environment not only for sensor testing and visualization, but also for vehicle simulation dynamics. Planning autonomous or intelligent driving is divided into hierarchical classes. Generally, there are four classes: route planning, path planning, maneuver choice and trajectory planning [1]. Three of them (path, maneuver and trajectory) are components of autonomous on-road driving, which takes into account vehicular dynamics, obstacles, road geometry and traffic interactions. Often these three classes are combined as one. Route planning is concerned with finding the best global route from a given origin to a destination, supplemented occasionally with real-time traffic information.

The path is determined as a continuous sequence of initial and terminating configurations with the boundary conditions. Consequently, path-planning is the problem of finding a geometric path from an initial configuration to a given terminating configuration such that each configuration and state on the path is a feasible one. For driving autonomously on public roads the vehicle at each moment should be able to choose the best and safest maneuver to perform after finding the best geometric sequence of waypoints to follow. After finding the best path to follow and the best maneuver to perform, a trajectory must be generated such that the motion model and state constrains are satisfied and this trajectory guarantees comfort for a passenger and smoothness for a trip. The problem of generating a trajectory, according to the path and the maneuver, is foremost solved by selecting a geometric curve to ensure smooth motion through the road network. After that the trajectory is optimized by using a cost function according to the dynamic model and the presence of obstacles along that trajectory. There are many approaches to solve the problems of route, path and maneuver planning. They are described in Refs. [1-3] and are not considered in this work.

Majority of existing planning methods rely on bicycle or car-like kinematic model for modeling a vehicle, but these models cannot exploit the basic maneuver capabilities of the car, because it doesn't take into account, for example, tire forces. A few approaches [4, 5] have

utilized the dynamic approach based on the bicycle model, and consequently take into account the mass of the vehicle and friction. However, the dynamic model which efficiently describes the motion and the distribution of forces of the vehicle in a real-world environment is yet to be implemented. One of the big challenges is to capture and abstract a vehicle's capability and constraints and then introduce this information in maneuver and trajectory planning. Examples include acceleration, braking or steering constraints and the influence of weather or road surface on these capabilities or constraints.

Because the simulations of the vehicle physics (and dynamics) are complicated, it is unfeasible to use real-time and online simulations for vehicle trajectory prediction algorithms. This leads to alternative solutions like using the pre-calculated dynamic database. One of the biggest problems in vehicle dynamics is the tire kinematics behavior. The slip characteristics and the damping of the tires have a big influence on the vehicle steering capacities. The tire slip angle has a non-linear behavior that is a function of the steering angle and acceleration. These features must be considered during the steering path analysis and setting.

Nowadays, a lot of accidents occur as a result of misplaced perception and decision making on the part of the human driver. Autonomous driving is envisaged to considerably reduce these mistakes because accurate risk assessment is vital for preventing accidents. Despite current systems are successfully applied to finding paths and detecting obstacles in reality, accidents still happen. Therefore, big accent must be given to precise risk estimation in real-time.

All sources [1-5] describe methods of route, path and maneuver planning that use strongly simplified car models. For correct real-time planning we need to consider the most realistic model of a car. The contribution of this work is to show the method of creation a vehicle motion prediction module for autopilot tasks with considering dynamic effects of all suspension parts using MBS model and also considering stiffness and damping of tires.

2. Modeling

There are three representative vehicles assigned to adjustment and test of the VDPM. All the vehicles will be modeled in MBS software with options like flex-body modeling. For this job MSC ADAMS-car has been chosen for the vehicle dynamic analysis. The virtual models of the representative vehicle have been created based on the study of every part.

At the first step, the vehicle needs to be separated into subsystems: body, front and rear axles, steering system, wheels, brakes and powertrain (Fig. 1). The body, power train, brakes and some subsystem parts usually are modeled as rigid parts (mass point), obviously only if they don't have any influence into the vehicle dynamics. It means, the compliance of the subsystems/parts should be analyzed and their global influence in the vehicle dynamic behavior has to be checked. The more relevant subsystems and parts are:

- *Body subsystem:* Bending and Roll stiffness are the most important characteristics of the vehicle (e.g. Body-on-frame trucks). If the stiffness of the vehicle is relatively low, the influence on the understeer characteristics of the suspension will be high. It means the body must be modeled as a flex body. One of the more relevant tests for the study of the understeer characteristics is the standard ISO 4138. This International Standard specifies the open-loop test methods for determining the steady-state circular driving behavior of passengers cars [6];

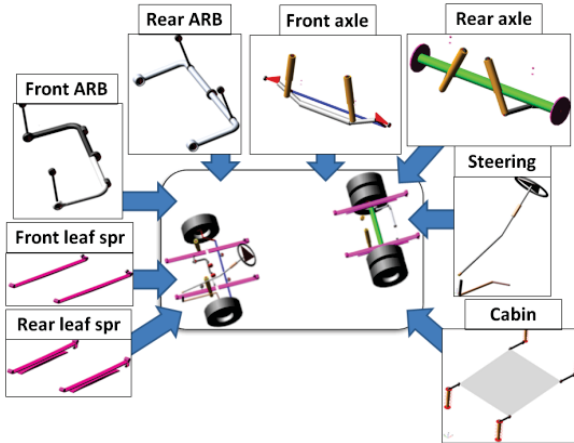


Fig. 1. Subsystems of the truck assembly.

- *Anti-roll bars (ARB)*: The stiffness of the ARB has the most significant on the suspension roll stiffness characteristics, and obviously the difference between the front and rear axle stiffness give us the understeer characteristic of the vehicle. This part can be modeled as flex-body or as two rigid bodies joined with a calculated torque able reproduce the flex-body roll stiffness characteristics;

- *Low stiffness parts*: In some vehicles (e.g. Lada Kalina) the lower control arms of the front suspension have a relatively low stiffness. This type of parts has to be modeled as flexible bodies, because they have some influence in the vehicle dynamics.

Usually, for the flex-body modeling in the MBS software the Craig-Bampton method is used. This method permit to get the linear deformation behavior of the body, based on the superposition of the normal modes [7]. This type of methods has low CPU requirements and are one of the more frequently used methods to speed up the CPU time. There are other methods, like co-simulation with finite-element solvers, but the CPU time cost is very high relatively to the flex-body ones. All these subsystems should be validated by natural tests rigs, like K&C. And then a final full vehicle dynamics validation must be performed, to be sure the MBS model of the vehicle is an accurate digital twin of the original one (e.g. ISO 7401 and ISO 4138).

The next step is to simplify the models without losing precision. This is done by replacing flexible bodies with equivalent simple elements, e.g. anti-roll bars can be modeled as two rigid bodies and equivalent forces, the lead springs of the trucks and etc.

3. Virtual maneuvers

The target of the VDPM use is the prediction and rating of maneuver dynamic parameters of the vehicle. To create a database of maneuvers, it is crucial to parameterize them. Then the parameterized maneuvers are classified as standard maneuvers. If a maneuver cannot be parameterized, it is classified as non-standard. For instance, usually single lane change is designed by smooth paths. The input parameters of the maneuver are: road friction, vehicle speed, longitudinal and lateral target displacement. In the maneuver parameterization step this maneuver will be classified as standard. For this job, the assigned standard maneuvers are:

- *Lane change*: In Figure 2 the lane change trajectory of a vehicle is designed as a smooth curve. A quintic polynomial is used to describe this curve from the start point to the final point

of the maneuver. The lateral displacement is based on the lane road width standards and vehicle dimensions. The longitudinal displacement is limited by the vision sensors range.

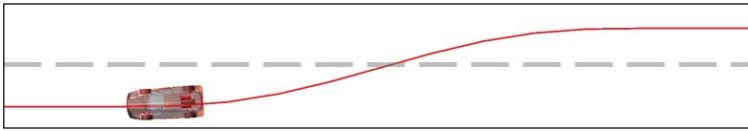


Fig. 2. Lane change maneuver.

- *Evasive maneuver:* this maneuver is simulated for a given initial trajectory based on the lane changer maneuver and initial speed. At the same time, at the beginning of the lane change maneuver from point A0 to A1 (Fig. 3), the car was subjected to a longitudinal acceleration, corresponding to braking (direction is opposite to the vehicle direction). The final target is to define the stop time, the path derivation and the slip angle of the vehicle. An example of the study of the evasive maneuver for a light vehicle with a start speed of 40km/h and different acceleration values is shown in figure 3.

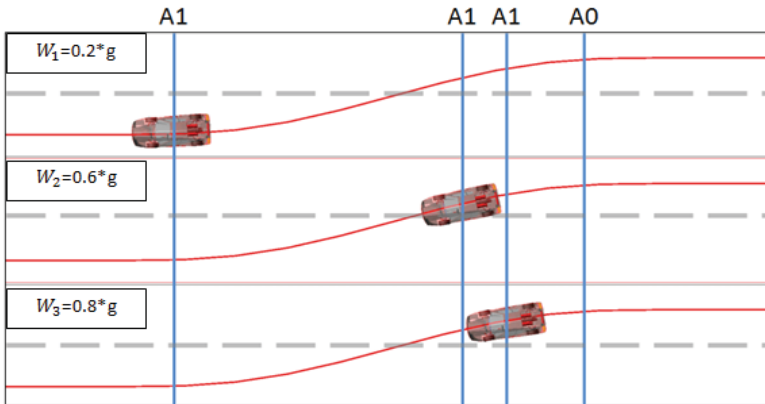


Fig. 3. Evasive maneuvers (40km/h).

The problem of the non-standard maneuvers will be solved by an interpolation and stitch of primitive maneuvers.

- *Primitive maneuvers:* to understand and to use the primitive maneuvers it is necessary to understand the vehicle response to a direction change. In Figure 4 the peculiar graphics of the steering path and lateral acceleration for lane change maneuvers are shown. Here curve 1 is a lane change start with a non-zero initial steering angle, and curve 2 is for a zero initial steering angle. As can be seen, the two steering paths are similar at the time 2s, but the acceleration is similar only at the time $\sim 2.3s$. The acceleration graphic shows that the vehicle response to the steering change is $\sim 0.3s$. It means that the path of the vehicle will be identically at the time $\sim 2.3s$. The approbation of this effect allows one to stitch different parametrical (standard) maneuvers for reproducing a non-standard maneuver.

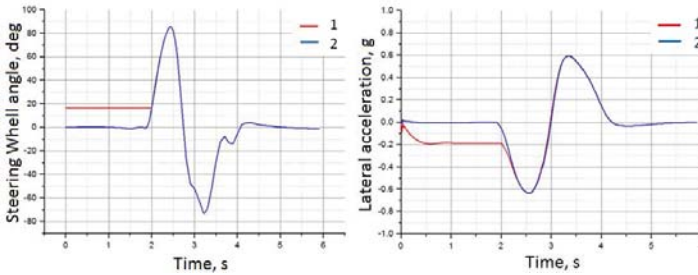


Fig. 4. 1-steering path, 2-lateral acceleration.

The last affirmation helps us to understand the primitive maneuvers stitching logic. But the study of the equivalence of the vehicle dynamics during the last maneuvers is not only based on the lateral acceleration; it is also necessary to take a look to the slip angle of the tires, roll angle of the vehicle, etc.

4. Pre-run simulations

Before the VDPM starts the database generation, the information of the primitive maneuvers functions and the vehicle physical limits must be given. The primitive maneuvers functions are designed using standard functions for the selected self-driving inputs and steering actuator capacities. Therefore, these functions depend on the particular automobile and also on the self-driving algorithms they are generated for. To obtain the vehicle physical limits, it is necessary to study the vehicle capacity to reproduce the required steering inputs inside a safe maneuvering area. To define the physical limits of the vehicle several tests are run [8]. This step gives us the possibility to reach the critical values and dependencies of the automobile dynamic parameters, e.g. the maximum lateral acceleration, as functions of the steering values and steering speeds. The analysis of this information helps us to create rating criteria for the vehicle maneuvers. The steering capacities of a vehicle are represented in Figure 5. In this figure three rating areas can be found. These areas are separated by step steering and smooth maneuvering by the steering path timing. The values of these areas change from vehicle to vehicle. It is also important to note that the higher the steering speed signal, the lower the vehicle is able to reproduce the steering amplitude. The information about maneuvers and their real values are not presented in this paper because this information is confidential.

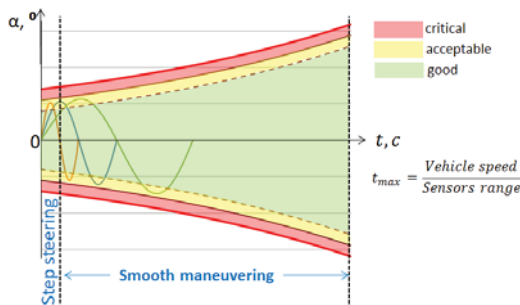


Fig. 5. Steering path working area.

5. Fitting algorithm

The procedure of the VDPM is described by the following basic steps:

1. The autopilot has a task to move from point A to point B, e.g. single lane change shown in Figure 6.



Fig. 6. Single lane change.

2. In this step, the autopilot creates a reference road course from point A to point B. A steering input is calculated by the autopilot algorithms. The steering input is based on the initial conditions of the vehicle at point A (e.g. velocity, steering angle, etc.) and is illustrated in Figure 7.

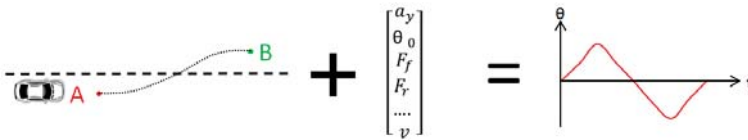


Fig. 7. Maneuver inputs.

3. Then using the initial conditions of the vehicle and the steering input, the VDPM is able to find a solution from the pre-calculated simple maneuvers database. After the solution with the initial conditions is found, the VDPM compares the autopilot and the database steering input.

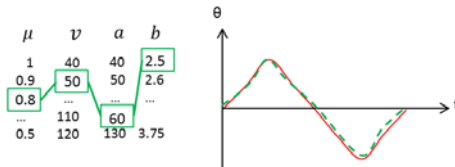


Fig. 8. Maneuver searching.

4. Then the difference (error) between the autopilot and VDPM steering inputs is calculated (Fig. 8):

If the error is lower than a defined threshold, the VDPM database outputs the predicted output parameters array. The output parameters describe the vehicle dynamic status on the way from point A to point B. The evaluated output parameters, for example, are: path derivation, wheel forces balance, lateral acceleration, roll angle, vehicle slip angle, etc.

If the error is higher than a defined threshold and the steering inputs differs, the VDPM searches a solution with a parameters array based on primitive maneuvers. These maneuvers have a limited number of variations. And all these variations cover every possible dynamic behavior of the vehicle. Interpolation algorithm is responsible of finding the required function and computes the corresponding parameters array.

Once a solution is found, the VDPM creates an output parameters array of the vehicle from point A to point B as an interpolation, and stitches primitive maneuvers. The created

output parameters array describes the vehicle dynamic behavior on the course from point A to point B by discrete steps i . The procedure of the last algorithm can be described as a maneuver division into n steps, based on the vehicle steering response characteristics. The output parameters at step i solution are used as input parameters for searching and interpolate a solution in the database for the next step $i+1$. At the final step, after all the solutions are found, they are stitched in.

6. Database optimization and CPU time and searching

To optimize the database generation and its usage, a few techniques were adopted from the time step for calculations to the memory use during the database search process:

1. Time step: early, in Figure 4 the peculiar steering path was mentioned. Now, we will try to study the influence of the discretization of this path by two ways. In Figure 9, we have a discretization of the steering path (curve 1) with a fixed time step of 0.1s in the left side (curve 2), and in the right side, the same discretization method but with the count of the function extremums (curve 3).

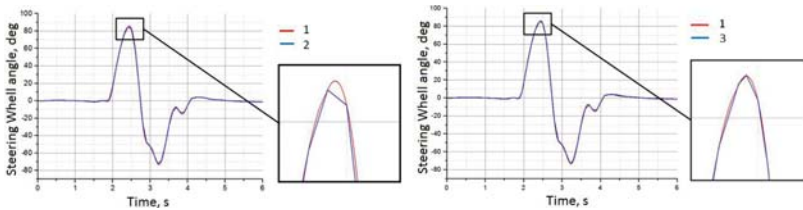


Fig. 9. Steering path discretization.

The results of the discretization methods show the influence of the extremums count in the steering path function (fig. 10). As we can see, the lateral acceleration is very similar to in all 3 cases, but the lateral displacement show a big derivation from the original one when the steering path extremums are not on count.

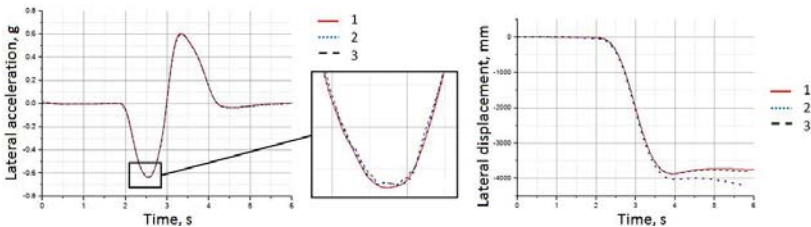


Fig. 10. Results of the steering path discretization methods.

The last affirmation force us to use the discretization process to run the MBS analysis, but only if the extremums of the steering function is on count.

The next step is the optimization of the memory usage. There exist vehicle state parameters that will not change abruptly while the vehicle is moving, e.g. the velocity or friction coefficient. Therefore, to speed-up the VDPM response, a several number of decisions are fixed;

The database has a subordination order, from the parameters with the lower changes during the vehicle movement to the parameters with the higher changes, e.g. the friction coefficient with the road is the first search parameter, then the speed, etc;

The VDPM is always working while the vehicle moves, and a corresponding searching corridor is loaded to the memory all the time. The limits of this corridor are the minimum and maximum probable “parameters” moving corridor of the automobile in the current movement case. This corridor permits to constrain the searching process and load only the needed segment of the database.

7. Summary and conclusions

The three MBS models of the vehicles were created to test and calibrate the VPDM. All these models were optimized to reach more rapid testing without any loss of accuracy on the dynamic behavior of the vehicles.

The VDPM considers the physical limits of the vehicle. Because these limits are known, the VDPM describes all the maneuvers inside safe maneuvering areas. The non-pre-simulated maneuvers (non-standard) are described by stitching primitive maneuvers.

Acknowledgement

Researches were implemented as a part of the project, financed by the Foundation for Assistance to Small Innovative Enterprises (FASIE).

References

- [1] C. Katrakazas, M. Quddus, W. Chen, L. Deka, Real-time motion planning methods for autonomous on-road driving: State-of-the-art and future research directions // *Transportation Research Part C: Emerging Technologies* **60** (2015) 416–442.
- [2] V.T. Minh, J. Pumwa, Feasible Path Planning for Autonomous Vehicles // *Mathematical Problems in Engineering* **12** (2014).
- [3] M. Althoff, D. Althoff, D. Wollherr, M. Buss, Safety Verification of Autonomous Vehicles for Coordinated Evasive Maneuvers // *IEEE Intelligent Vehicles Symposium IV* (2010).
- [4] J. Jeon, R.V. Cowlagi, S.C. Peters, S. Karaman, E. Frazzoli, P. Tsiotras, K. Iagnemma, Optimal motion planning with the half-car dynamical model for autonomous high-speed driving, In: *American Control Conference* (US, Washington, 2013) pp. 188–193.
- [5] O. Sawodny, J. Zimmermann, A. Lutz, Motion planning for an autonomous vehicle driving on motorways by using flatness properties, In: *2010 IEEE International Conference on Control Applications* (Japan, Yokohama, 2010) pp. 908–913.
- [6] ISO 4138 Passenger cars – Steady-state circular driving behavior – Open-loop test methods.
- [7] MSC ADAMS help. Adams/flex. Theory of the flexible bodies.
- [8] ISO 7401 Road vehicles – Lateral response test methods – Open-loop test methods.

APPLICABILITY OF POLYMER COMPOSITE MATERIALS IN THE DEVELOPMENT OF TRACTOR FALLING-OBJECT PROTECTIVE STRUCTURES (FOPS)

Dmitrii Lebedev*, Alexey Okunev, Mikhail Aleshin, Kirill Ivanov, Oleg Klyavin,

Svetlana Nikulina, Oleg Rozhdestvenskiy, Alexey Borovkov

Peter the Great St. Petersburg Polytechnic University, Polytekhnicheskaya 29

195251, St. Petersburg, Russia

*e-mail: lebedev@compmechlab.ru

Abstract. Analysis of application efficiency of polymer composite materials (PCM) in the development of tractors falling-object protective structures with the use of finite element method and modern systems of engineering analysis (CAE) is done. An elasticity and fracture model of composite materials is developed. A series of virtual crash tests of the tractor cab is carried for both cases with and without PCM. On the basis of this research, a methodology of designing PCM roofs for tractor cabs is developed.

Keywords: composite material, crash test, design, finite element model, tractor cab.

1. Introduction

Often tractors on the same platforms are used for different applications, e.g., agricultural and logging operations. However, the requirements to protective structures for tractor cabs to ensure protection from falling objects differ significantly, depending on the purpose of using a tractor. Development and production of a universal cab for both agricultural and logging operations is very expensive and inappropriate.

Trends in the global tractor industry also dictate the increased requirements to the tractor design. The tractor roof, as part of the falling-object protective structures (FOPS), is one of the design main elements. Using polymer composite materials (PCM) in the roof structure removes almost all constraints on its shape, which in its turn has a positive effect on the design. Due to mechanical properties of composite materials, besides the aesthetic function, it allows significantly decrease the impact from falling objects.

2. Goals and objectives

The goal of the project, funded by the Ministry of Education of the Russian Federation, is to develop a methodology for designing tractor cabs, taking into account regulatory and design requirements. The methodology approbation was carried out on the new generation of articulated tractors produced by Zavod SPETSTEHNKI LTD (St. Petersburg) with improved safety, design, visibility and ergonomics, vibro-acoustic and climate comfort.

At the first stage of the project, a digital model of the tractor original design is developed to define layout constraints for the design. After that an updated exterior surface is developed; a cab frame structure being designed. Currently the work of refining the design and structural configuration of the cab is underway and shown in Figure 1 [1].

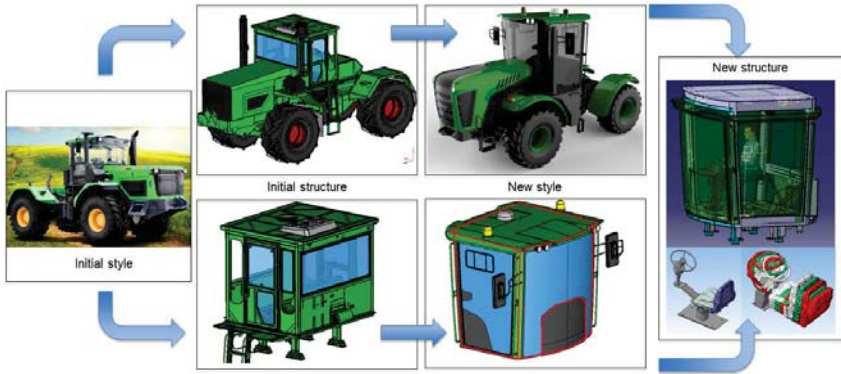


Fig. 1. New design development of a cab.

The purpose of this work is to develop a methodology for designing a unified falling objects protective structure of the tractor cab using polymer composite materials, capable to pass both level I and level II penetration protection tests [2]. To achieve this, the following problems are developed and solved within the current study for a tractor:

- finite element model (FEM) of falling-object protective structures (FOPS);
- elasticity and fracture model of composite materials;
- series of virtual FOPS crash tests;
- methodology of designing FOPS for reducing impact loads on a cab.

3. Finite element model of tractors FOPS

The cab roof was not initially taken into account, in the first version of the analysis and it was not modeled (Fig. 2a). In the second variant, the FEM included the roof with panel of the PCM (Fig. 2b). In this case, it has two functions: a full FOPS element and a design element (exterior panel). A FEM of FOPS was developed in the software package ANSA [3] for the purpose of conducting virtual testing. The FEM parameters are shown in Table 1.



Fig. 2. FEM model of FOPS: *a)* traditional FOPS, *b)* FOPS from composite panels.

Table 1. FEM parameters.

№	Parameter	Value, traditional FOPS	Value, FOPS with PCM panel
1	Number of elements	154169	186388
2	Number of nodes.	172350	182245
3	Type of the elements	PSHELL	PSHELL
4	Calculation time	57 min	73 min

4. Composite material model development and verification

In the LS-DYNA software package there are several models of polymer composite materials. Comparison of the most popular of them is shown in Figure 3 [4]. To simulate the composite panel material type 22 *mat_composite_damage [5] was selected; it takes into account possible fractures of the material. The model allows define the properties of an orthotropic material with optional brittle fracture for composites [6, 7]. As a material for the tractor roof, three-layer structure is selected: glass Mat company Metyx, Metycore 600M/250PP1/600M, covered of both sides with fiberglass-type 120 and binder VSE-34. According to Ref. [8], for calculating the tensile strength and elastic modulus of fiberglass it is necessary to determine the physical and elastic-mechanical characteristics of its constituents: glass reinforcing filler and binder (matrix). The data of commercially available glass fiber reinforcement are widely presented in the literature [9-12]; on contrary, the matrices properties should be often determined experimentally. Characteristics of fiberglass and binder are given in Ref. [8].

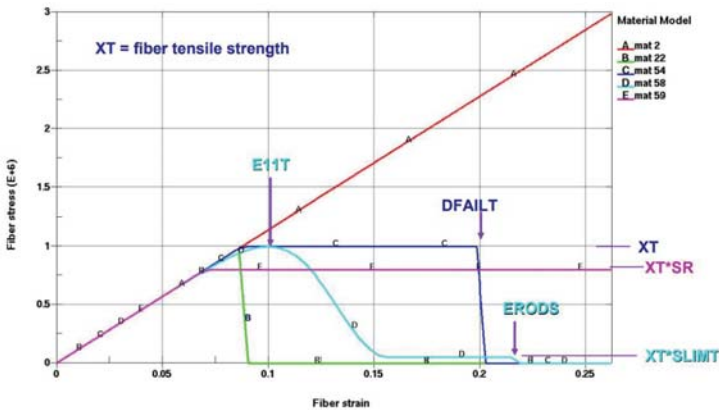


Fig. 3. Comparison of composite materials models.

MAT22 is based on a reduced Chang-Chang failure criterion, where elements are deleted when the Chang-Chang criterion is fulfilled. Chang and Chang [16] proposed a 2D failure criterion for unidirectional composite lamina which is as follows:

$$\text{For tensile fiber mode: if } \sigma_{11} > 0, \text{ then } \left(\frac{\sigma_{11}}{X_t}\right)^2 + \frac{\sigma_{12}}{S_c} = 1;$$

$$\text{For compressive fiber mode: if } \sigma_{11} < 0, \text{ then } \left(\frac{\sigma_{11}}{X_c}\right)^2 = 1;$$

$$\text{For tensile matrix mode: if } \sigma_{22} > 0, \text{ then } \left(\frac{\sigma_{22}}{Y_t}\right)^2 + \left(\frac{\sigma_{12}}{S_c}\right)^2 = 1;$$

$$\text{For compressive matrix mode: if } \sigma_{22} < 0, \text{ then } \left(\frac{\sigma_{22}}{2S_c}\right)^2 + \left[\left(\frac{Y_c}{2S_c}\right)^2 - 1\right] \frac{\sigma_{22}}{Y_c} + \left(\frac{\sigma_{12}}{S_c}\right)^2 = 1.$$

Here σ_{11} is the lamina stress in the fibers direction, σ_{22} is the lamina stress in the transverse direction to the fibers, σ_{12} is the lamina in-plane-shear stress, X_t is the fiber tensile strength and X_c is the fiber compressive strength, Y_t is the fiber tensile strength in the transverse direction and Y_c is the fiber compressive strength in the transverse direction; S_c is the in-plane-shear strength.

The material model *mat_composite_damage allows simulate the behavior of a layered structure that was also done in the present work.

5. Design of a PCM panel

The main function of the PCM roof panel at crash tests is to maximize the energy absorption from falling objects. Consider the panel as a simply supported plate. The strain energy resulted from plate bending in terms of deflections $w(x,y)$ is:

$$U = \frac{1}{2} \iiint_V (\sigma_x \varepsilon_x + \sigma_y \varepsilon_y + \sigma_z \varepsilon_z + \tau_{xy} \gamma_{xy} + \tau_{xz} \gamma_{xz} + \tau_{yz} \gamma_{yz}) dx dy dz, \quad (1)$$

where V is the plate volume.

Using the hypotheses of the plate bending theory and integrating equation (1) along the thickness, we obtain the following expression:

$$U = \frac{D}{2} \iint_A \left[\left(\frac{\partial^2 w}{\partial x^2} \right)^2 + \left(\frac{\partial^2 w}{\partial y^2} \right)^2 + 2\nu \frac{\partial^2 w}{\partial x^2} \frac{\partial^2 w}{\partial y^2} + 2(1-\nu) \frac{\partial^2 w}{\partial x \partial y} \right] dx dy = \frac{D}{2} \iint_A \left\{ \left(\frac{\partial^2 w}{\partial x^2} + \frac{\partial^2 w}{\partial y^2} \right)^2 - 2(1-\nu) \left[\frac{\partial^2 w}{\partial x^2} \frac{\partial^2 w}{\partial y^2} - \frac{\partial^2 w}{\partial x \partial y} \right]^2 \right\} dx dy, \quad (2)$$

where A is the area of plate middle surface, D is the plate cylindrical stiffness.

Assuming that the deflection of plate faces is zero, we have the following expression for the plate potential energy:

$$U = \frac{D}{2} \iint_A \left(\frac{\partial^2 w}{\partial x^2} + \frac{\partial^2 w}{\partial y^2} \right)^2 dx dy \quad (3)$$

From equation (3) it follows that the energy absorption of a composite roof plate can be increased both by enlarging the stiffness and by increasing the deflection. On the other hand, the maximum deflection is limited to metal beams of the FOPS structure (Fig. 4).

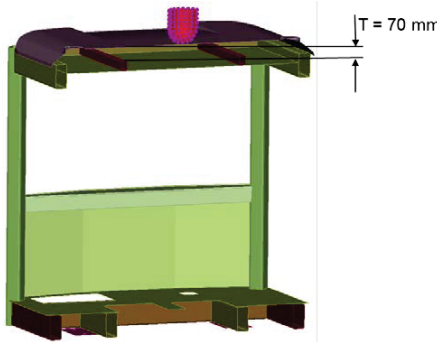


Fig. 4. Tractor FOPS in section.

Thus, it is important to choose the thickness and the material composition for the roof in such a way that its critical deflection, before fracture begins, does not exceed the distance from the roof plane to the FOPS beams. This parameter can be modified during the development of cab; in the current work it is equal to 70 mm.

A series of static tests was performed for a composite roof of different stiffness with various number of fiberglass layers (Fig. 5). Figure 6 shows the dependence of the roof panel maximum deflection on the PCM thickness. From the figure one can see that deflection 70 mm is achieved if the roof-material thickness is slightly less than 6 mm. This configuration will be used in subsequent calculations.

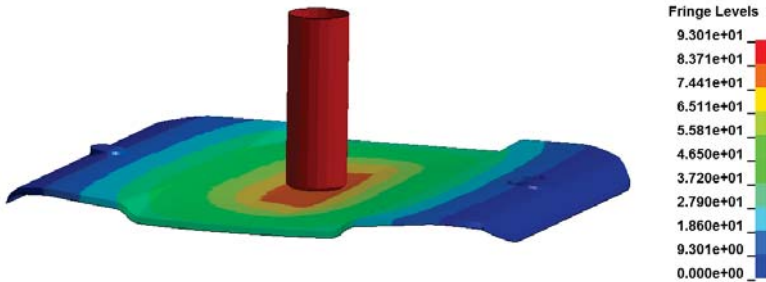


Fig. 5. Deflection of composite roof during static tests.

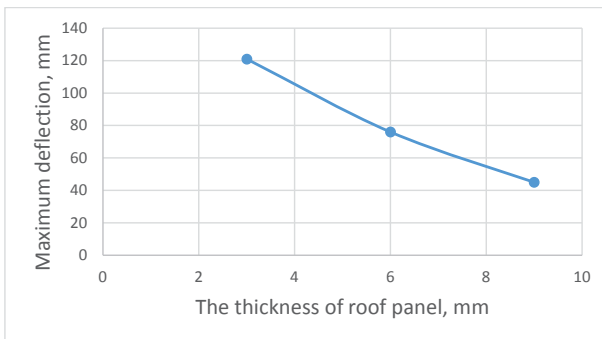


Fig. 6. Dependence of roof-panel deflection on PCM thickness.

6. Virtual tests

According to Ref. [13] the tractor FOPS can be divided into two categories: level I impact protection deals with the impact from small falling objects (e.g., bricks, small concrete blocks, hand tools, etc.) encountered in highway maintenance, landscaping and other construction site services; level II impact protection does from large falling objects (e.g., trees, rocks) for machines involved in site clearing, overhead demolition or forestry. In laboratory conditions, these tests are conducted by dropping a standard object (indenter) of a predetermined shape and mass from a certain height. The test parameters are given in Table 2.

Table 2. Test parameters for level I and II impact protection.

Impact protection level	Indenter parametrs		
	Form	Weight, kg	Drop height, m
Level 1	round	45	3,1
Level 2	cylindrical	227	5,22

One of the objectives of the present work is the development of a methodology for designing unified tractor cabs, according to the technical regulations of the Customs Union [14], which are able to ensure both the level I and level II impact protection. This cab will significantly reduce the cost of development and manufacture.

Both FOPS, investigated within the present work, pass the test of level I impact protection. Figure 7 shows tractor FOPS after a series of virtual tests for level II impact protection. The places for the test impact were selected according to [13] and [15].

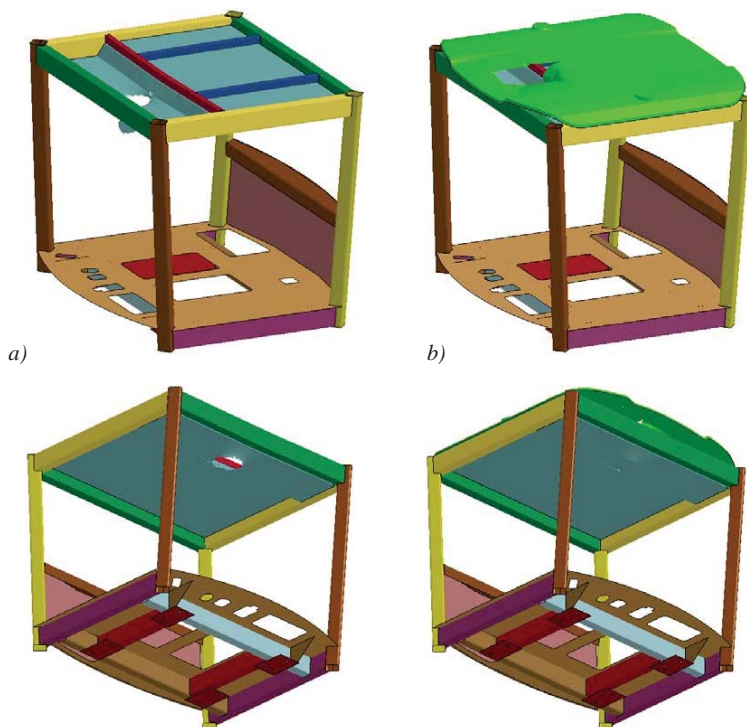


Fig. 7. Results of level II impact protection test, where *a)* traditional tractor FOPS, *b)* tractor FOPS with composite roof panels.

From Figure 7 it follows that the traditional tractor FOPS failed level II impact protection test, while the FOPS tractor with composite panel passed this test. Analyzing the data calculated for the FOPS of the tractor cab with a PCM roof, one can see that the FOPS have passed of the crash tests. The PCM roof of the cab collapsed at all the stages of testing, but the deflection of metal structures was reduced by an average of 30%, thus ensuring greater protection of a tractor driver. Applying an indenter in the crash tests of a PCM tractor cab roof panel, we have observed the decrease of its speed by 36% for level I impacts and by 16% for level II impacts at the moment of interaction. From this we can conclude that the PCM roof panels absorb a significant amount of the energy of a falling object, particularly 59% for level I impact protection tests and 30% for level II impact protection ones.

7. Conclusions

The results of the research presented in this work were used to design a universal tractor cab satisfying the requirements for level I and level II penetration protection (FOPS). The results were achieved through the use of PCM as the cab roof panel material. While remaining an important design element, the roof became a functional part of the tractor FOPS. A design methodology aimed at minimizing roof deflection on impact was also developed. In the future, PCM roof panels can replace traditional metal roofs through the use of new strengthened composite materials, by using thicker plates or implementing reinforcing metal insertions. As the result, reduction in materials consumption and overall weight of the cabs together with improved ergonomics (due to extension of the workspace) might be achieved.

Acknowledgments

The work is carried out with financial support of the Ministry of Education and Science of the Russian Federation; the Federal Program "Research and Development in Priority Areas for the Development of Russian Science and Technology Complex for 2014-2020", Activity 1.3., Agreement on the Grant No. 14.578.21.0206 of 03.10.2016, the unique identifier of the program of research and experimental works: RFMEF157816X0206.

References

- [1] A. Leontev, Optimal design of power frames for special purpose vehicles' cockpits with regard to their eigenfrequencies and shock resistance, In: *International Conference on Engineering Vibration* (Sofia, Bulgaria, 2017).
- [2] GOST R ISO 3449-2009 digging Machines. Device protection from falling objects. Laboratory tests and technical requirements.
- [3] <https://www.beta-cae.com/ansa.htm>
- [4] LS-DYNA composite materials guidelines, Livermore software Technology Corporation.
- [5] Ls-Dyna keyword user's manual, Livermore software Technology Corporation, 2001.
- [6] F.K. Chang, K.Y. Chang, A post-failure analysis of bolted composite joints in tension or shear-out mode failure // *J. Composite Materials* **21** (1987) 809-833.
- [7] I.S. Sandler, D. Rubin, An algorithm and a modular subroutine for the cap model // *Int. J. Numer. Anal. Meth. Geomech.* **3** (1979) 173-186.
- [8] D.A. Melnikov, A.A. Gromov, A.E. Raskutin, A.O. Kurnosov, Theoretical calculation and experimental determination of the modulus and strength of FRP VPS-53/120 // *Trudy VIAM* (2017)
- [9] S.L. Roginskii, M.Z. Kanovich, M.A. Koltunov, *High Strength Fiberglass* (Moscow, Chemistry, 1979) 144 p.
- [10] B.A. Kiselev, *Fiberglass* (Moscow, GOS, 1961) 240 p.
- [11] G.M. Gunaev, *Structure and Properties of Polymeric Fibrous Composites* (Moscow, Chemistry, 1981) 232 p.
- [12] A.M. Skudra, F.Y. Mace, *Strength of Reinforced plastics* (Moscow, Chemistry, 1982) 216 p.
- [13] GOST R ISO 3449-2009 digging Machines. Device protection from falling objects. Laboratory tests and technical requirements.
- [14] TR CU 031/2012. Technical regulations of the Customs Union. On safety of agricultural and forestry tractors and trailers.
- [15] GOST ISO 8083-2011 (GOST R ISO 8083-2008) Machines for the forest. Device protection from falling objects. Technical requirements and test methods.
- [16] F. Paris, A study of failure criteria of fibrous composite materials, *NASA/CR- 2001-210661* (March 2001).

VARIATIONAL PROBLEM FOR HYDROGENERATOR THRUST BEARING

O.V. Antonova*, A.I. Borovkov, Yu.Ya. Boldyrev, I.B. Voynov

Peter the Great St. Petersburg Polytechnic University, Polytekhnicheskaya 29

195251, St. Petersburg, Russia

*e-mail: antonova_ov@spbstu.ru

Abstract. Reversible and irreversible heavy loaded thrust bearings of a hydrogenerator are investigated. The problem of oil wedge microgeometry profiling for load capacity optimization is considered. The analysis is based on optimization methods using variational calculus. The results of oil wedge microgeometry optimization for reversible and irreversible thrust bearings are presented.

Keywords: hydrogenerator, load capacity, optimization, thrust bearing.

1. Introduction

In conditions of dynamic development of the world hydropower and construction of a large number of hydropower plants in developing economics: Brazil, China, India, etc. it is important to ensure reliable trouble-free operation of the key structural elements of the plant. One of the most important structural elements is a hydrogenerator thrust bearing which perceives a major part of a load. Generally, the load on the thrust bearing is produced by a rotor, an impeller, and turbine shaft weight and water pressure on the impeller [1, 2]. The important operational parameter that characterizes the efficiency of the bearing is the load capacity of an oil wedge that is a nonlinear function of the gap magnitude. The main role performs the minimal oil film thickness; the thinner the oil layer, the higher the bearing load capacity. However, reduction of oil film thickness leads to decreasing the bearing stability under dynamic loads.

There are various classifications of the bearings: by geometrical characteristics, by perceived load, by number and type of supports and by kind of mounting. By the surface type realization bearings are divided into one-piece and segmented. One-piece bearing carrier surface is a surface coated with a relief profile. Such bearings are called profiled. Segmented or self-aligning acting bearings are the bearings which fixed part consists of separate segments, mounted on special supports that allow each segment to turn in the flow of liquid lubricant, forming an angle with the rotating disk surface. In order to provide greater load capacity, the support is moved relative to the segment axis by a certain value in the direction of rotation, creating eccentricity. Typically, the value of the eccentricity is 5-8 % of the segment length. Such bearings are called irreversible because they demonstrate the load capacity for only one rotation direction. In hydropower they are used for a wide range of devices on the majority of the existing plants.

However, in some cases, for example for devices with variable rotation direction of the turbine generators, it is necessary to set zero segments eccentricity to ensure the durability of the device. Such bearings are called reversible. Currently, the thrust bearing of this type is installed on Zagorskaya GAES, unique and the Russian only pumped storage power station.

In this work we consider the lubricant layer microgeometry profiling with the aim of optimal design of the hydrodynamic bearing for ensuring the maximum load capacity.

2. Optimization problem statement

Note that historically the first formulation of the considered problem in one-dimensional case goes back to the work by J.W. Rayleigh published in 1918 [5]. The Rayleigh results were much ahead of his time, were repeated later by S.Y. Maday only in 1967 [6]. In 1975 one of the authors together with V.A. Troitsky considered the spatial variational problem put by Rayleigh to gain the optimal shape profile for the rectangular gap region [3]. For the sector bearings considered here, one of the authors, jointly with Yu.V. Borisov obtained the first results in Ref. [7]. Here we enlarge the results of the previous works [3, 7] in relation to the hydrogenerator sector thrust bearings based on advanced computing technologies. It is worth noting that over the last years unique technologies of desired shape surface microgeometry manufacturing were developed, the optimization results can being implemented.

We consider the optimization problem of the thrust sector bearing microgeometry [3]. An example of such bearing is shown in Figure 1. One bearing segment with installation angles indication is presented in Figure 2. All the sectors are assumed to be identical and the sector angle $\Delta\varphi = 2\pi / N$, where N is the number of sectors. We assume that region Ω with boundary $\partial\Omega$ (Fig. 3), corresponding to one thrust bearing sector, is located in (r, φ) plane of cylindrical coordinates (r, φ) . Plane (r, φ) moves in the φ direction with constant angular velocity ω .



Fig. 1. Michell thrust bearing [4].

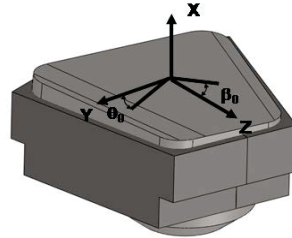


Fig. 2. Thrust bearing segment.

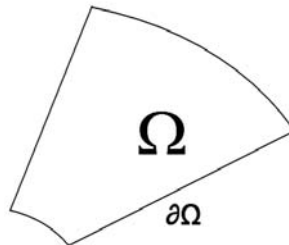


Fig. 3. Region Ω .

We will describe the profile shape of the lubricating layer by piecewise-smooth function $h(r, \varphi)$ and assume that h_{min} is its minimum value. We suppose that pressure field $p(r, \varphi)$ in the lubricant layer is described by the linear Reynolds equation written in the following dimensionless form:

$$\operatorname{div}(h^3 \nabla p - h \mathbf{V}) = 0 \text{ in } \Omega \tag{1}$$

Here the dimensionless pressure p and the coordinates r and φ are normalized correspondingly by ambient pressure p_a and dimensional values L_r and L_φ that characterize segment dimensions. Note that the critical parameter $\gamma = L_r/L_\varphi$ characterizing the elongation of region Ω in equation (1), here and throughout is put equal to 1 for simplification of calculations. The profile function h is normalized by h_{min} . The velocity vector $V_\varphi = (1, 0)$ is normalized by the magnitude of $|V_\varphi|$. The boundary conditions for equation (1) correspond to zero pressure on the boundary $\partial\Omega$ of region Ω

$$p|_{\partial\Omega} = 0 \tag{2}$$

Note that equation (1) is an equation for the excess pressure $p(r, \varphi)$ in the lubricant layer in region Ω . According to shown above normalization character, the lubricant layer profile function $h(r, \varphi)$ should satisfy the restriction

$$h \geq 1 \tag{3}$$

In line with the last inequality, h_{min} is selected. Its value, corresponding to equilibrium stationary mode of thrust bearing operation, is specified usually from technological considerations.

The aim is construction of the lubricant layer profile $h(r, \varphi)$ that provides maximum sector load capacity. Thereby the negative value of the lifting force of the lubricant layer, normalized by $L_r L_\varphi p_a$, can be used as a variational problem functional. The negative sign is chosen according to traditional rules of the variational calculus for searching a functional minimum

$$W = - \int_{\Omega} p d\Omega \tag{4}$$

Thus we can formulate the optimization problem in such a way: find among continuous in Ω functions p that satisfy the boundary value problem for Reynolds equation (1, 2) and among piecewise continuous functions h satisfying the condition (3) those that provide minimum to functional (4). Further, we follow the approaches developed in Refs. [3, 8].

Introduce an auxiliary function $v(r, \varphi)$ and switch from the constraints of inequality (3) to constraints of equality

$$\psi = h - 1 - v^2 = 0 \tag{5}$$

Write down equation (1) in the form of following system of equations

$$\operatorname{div} \mathbf{Q} = 0, \mathbf{Q} = h^3 \nabla p - h \mathbf{V} \text{ in } \Omega, \tag{6}$$

where \mathbf{Q} is the dimensionless volumetric flow vector, normalized by $h_{min}|V_\varphi|$. We satisfy the first of equations (6) by introducing continuous function $M(r, \varphi)$ in the following way:

$$\mathbf{Q} = \operatorname{rot}(M \mathbf{k}), \tag{7}$$

where \mathbf{k} is a unit vector of Z axis. We form auxiliary functional

$$J = \int_{\Omega} f(p, \nabla p, \mathbf{Q}, M, h, v) d\Omega \tag{8}$$

with augmented function f which includes the system of problem restrictions¹ (5-7)

$$f = -p + (\lambda_0, \mathbf{Q} - \operatorname{rot}(M \mathbf{k})) + (\lambda_1, \mathbf{Q} - h^3 \nabla p + h \mathbf{V}) + \lambda_2 \psi, \tag{9}$$

Here λ_0, λ_1 and λ_2 are the functional Lagrange multipliers, the first two being vectors.

In the articles mentioned above [3, 8] it is shown that in the case of a rectangular region Ω , the optimal function h has one line of discontinuity that starts at the extreme front points of the region and separates the front part of the region with $h > 1$ and back part with $h = 1$. In this case in the front part of the region ($h > 1$), pressure increases everywhere but at $h = 1$ it falls everywhere to an ambient value.

¹ Note, that the symbol (a, b) we define the scalar product of vectors.

Let us briefly discuss the numerical procedure for constructing profile h used in Refs. [3, 8]. First of all, note that at each step of the iterative procedure, in addition to the boundary value problem for Reynolds equation (1, 2), the boundary value problem for determining Lagrange multiplier λ , which is related to Lagrange multiplier λ_0 by $\lambda_0 = \text{grad } \lambda$, is also solved. Besides at each step the point value of the profile function is determined; at the points where $h > 1$ we have Euler-Lagrange equation:

$$3h^2 = (\nabla\lambda, \mathbf{V}) / (\nabla\lambda, \nabla p) \quad (10)$$

The discontinuity line position of function h is determined on the basis of Erdmann-Weierstrass conditions [2] from which, in particular, we find the equation for the line of discontinuity:

$$\left[-\frac{\partial\lambda}{\partial\tau} \frac{\partial M}{\partial n} + \frac{\partial\lambda}{\partial n} h^3 \frac{\partial p}{\partial n} \right]_{-}^{+} = 0, \quad (11)$$

where, $\left[\right]_{-}^{+}$ is value of difference to the right and left of the discontinuity line, \mathbf{n} and $\boldsymbol{\tau}$ normal and tangent vectors to function h . The equation (11) can be simplified – according to equation (6) one obtains $-\partial M / \partial n = Q_{\tau} = h^3 \partial p / \partial \tau - h V_{\tau}$ and final discontinuity line equation can be written in the following form:

$$\left[h^3 (\nabla\lambda, \nabla p) - h \frac{\partial\lambda}{\partial\tau} V_{\tau} \right]_{-}^{+} = 0 \quad (12)$$

Let us briefly consider the analysis of the system of necessary conditions. First of all, we point out that a correct analysis of this system presupposes knowledge of the solutions properties of partial differential equations of elliptic type [9], which include equations for Lagrange multiplier λ and Reynolds equation. Restricting ourselves to the final results, note that an analysis of the solutions properties of boundary value problems for pressure p and Lagrange multiplier λ allows do conclusions about the behavior of gradients ∇p and $\nabla\lambda$ on the domain boundary, under the additional assumption of the smoothness of the optimal solution everywhere except for the corner points of domain Ω . Taking into account the constancy of vector \mathbf{V} , we can conclude about the sign of scalar product $(\nabla\lambda, \mathbf{V})$. Together with Erdmann-Weierstrass conditions, it is possible to make an important conclusion about the existence of single discontinuity line γ for the profile function h in the region Ω that separates region $h = 1$ from region $h > 1$.

3. Optimization results for rectangular region statement

In this work the special case for rectangular region Ω with profile consisted of two parts: straight line and parabola (Fig. 4) was considered. Here, a and b are the geometrical parameters which define parabola curvature. The parameters are used as optimization variables during optimization procedure. Using special code IOSO, the optimization problem was solved. There are only one objective function and two variable parameters. As an objective function, the maximum of pressure integral over the lubricant layer surface was used. Parameters a and b are varied in the following range $a \in [0.03; 0.35]$, $b \in [0.5; 0.9]$. Global size of the rectangle is 1×1 .

To solve the optimization problem, the CFD mesh for investigated domain was generated and the hydrodynamics problem, using Navier–Stokes equations, was solved on the basis of numerical approach and commercial CFD code ANSYS/CFX. The numerical simulation of the problem was carried out using St. Petersburg Polytechnic Supercomputer Center. Totally about 70 iterations were done before the maximum of pressure integral was achieved. As a result, the optimal parameters a and b were found; they are 20.2 and 77.5 correspondingly. In Figure 5 the pressure distribution for the optimum profile is shown; in Figure 6 the dependence of the maximum pressure on a coordinate for section $y=0$ is demonstrated.

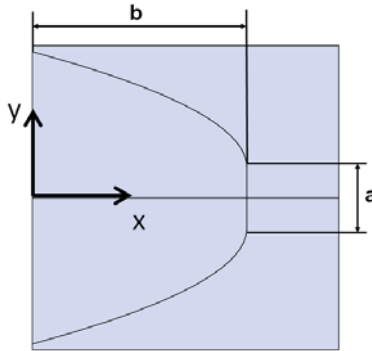


Fig. 4. Profile parameters for optimization procedure.

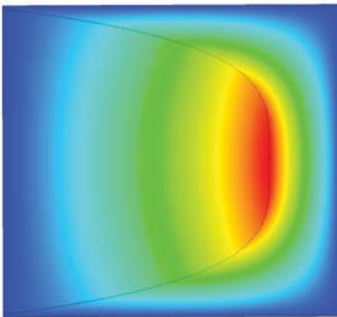


Fig. 5. Pressure distribution for the optimum profile.

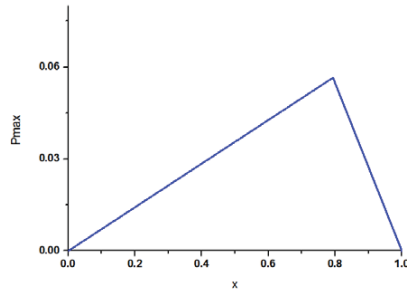


Fig. 6. Dependence of maximum pressure on a coordinate.

4. Conclusions

In this work the variational problem for hydrogenerator thrust bearing is considered. From problem statement above the important conclusion about the existence of a single discontinuity line of the profile function h in the region was made. This line separates the region $h = 1$ from the region $h > 1$. The optimization problem using commercial codes is solved for a rectangular region. Current results could be used in future investigations for a wide range of thrust bearing with different profile forms.

References

- [1] A.I. Abramov, A.V. Ivanov-Smolenski, *Analysis and Design of Hydrogenerators* (High school, Moscow, 1964) 259 p.
- [2] M.E. Podolsky. *Thrust Bearings: Theory and Design* (Mechanical engineering, Leningrad, 1981) 261 p.
- [3] Yu.Yu. Boldyrev, V.A. Troitski, One spatial variational problem of the theory of gas lubrication // *Tidings AS USSR MFG* **5** (1975) 34:
- [4] <http://www.michellbearings.com>
- [5] Lord Rayleigh, Notes on the theory of lubrication // *Phil. Mag.* **35(1)** (1918) 1.

- [6] C.J. Maday, A bounded variable approach to the optimum slider bearing // *Trans. ASME. Ser. F. J. Lubr. Technol.* **90(1)** (1968) 240.
- [7] Yu.Yu. Boldyrev, Yu.Yu. Borisov, Sector thrust bearing with gas lubrication, having the maximum bearing capacity // *Tidings AS USSR MFG* **6** (1990) 35.
- [8] Yu.Yu. Boldyrev, *Variational Calculus and Optimization Methods. Tutorial* (St. Petersburg Polytechnic University Publishing House, 2016) 240 p.
- [9] O. Ladyzhenskaya, N. Uraltseva, *Linear and Quasilinear Equations of Elliptic Type* (Science, Moscow, 1973) 576 p.

Submission of papers:

Manuscript should be submitted (**both MS Word and PDF**) by e-mail to: mpmjourn@spbstu.ru

After a confirmation of the paper acceptance, the authors should send the signed hard copy of the "Transfer of Copyright Agreement" form (available at <http://www.mpm.spbstu.ru> section "Authors") by regular post to "Materials Physics and Mechanics" editorial office:

Periodicals Editorial Office, Institute of Advanced Manufacturing Technologies, Peter the Great St. Petersburg Polytechnic University, Polytechnicheskaya, 29, St. Petersburg 195251, Russia.

The scanned copy of the signed "Transfer of Copyright Agreement" should be sent by e-mail to: mpmjourn@spbstu.ru.

Filetype:

Authors are invited to send their manuscripts **as MS Word file with PDF format copy.**

MS Word file should be prepared according to the general instructions below; we are kindly asking the authors to look through the detail instruction at: <http://www.mpm.spbstu.ru>.

Length:

Papers should be limited to 30 typewritten pages (including Tables and Figures placed in the proper positions in the text).

Structure of the manuscript:

PAPER TITLE: CENTERED, TIMES NEW ROMAN 14 BOLD, CAPITAL LETTERS

A.B. Firstauthor¹, C.D. Secondauthor^{2*} - Times New Roman 12, bold, centered

¹Affiliation, address, country - Times New Roman 10, centered

*e-mail: e-mail of the corresponding author - Times New Roman 10, centered

Abstract. Times New Roman 12 font, single line spacing. Abstract should not exceed 12 lines.

Keywords: please, specify paper keywords right after the abstract.

Paper organization. Use Times New Roman 12 font with single line spacing. Use *Italic* font in order to stress something; if possible, please, use **bold** for headlines only.

Page numbering. Please, do not use page numbering.

Tables, Figures, Equations. Please, see the sample file at <http://www.mpm.spbstu.ru> for more details.

References

References should be subsequently numbered by Arabic numerals in square brackets, e.g. [1,3,5-9], following the sample style below:

- [1] A.K. Mukherjee // *Materials Science and Engineering: A* 322 (2002) 1.
- [2] C.C. Koch, I.A. Ovid'ko, S.Seal, S. Veprek, *Structural Nanocrystalline Materials: Fundamentals and Applications* (Cambridge University Press, Cambridge, 2007).
- [3] A.E. Romanov, V.I. Vladimirov, In: *Dislocations in Solids*, ed. by F.R.N. Nabarro (North Holland, Amsterdam, 1992), Vol. 9, p.191.
- [4] C.K. Takemori, T.D. Müller, M.A. De Oliveira, *Numerical simulation of transient heat transfer during welding process*, In: *International Compressor Engineering Conference* (Purdue, USA 2010).
- [5] W. Pollak, M. Blecha, G. Specht // *US Patent 4572848*.
- [6] <http://www.mpm.spbstu.ru>

Правила подготовки статей:

Рукопись (**английский язык, MS Word и копия PDF**) должна быть направлена в редакцию журнала по электронной почте: mpmjjournal@spbstu.ru.

После подтверждения принятия статьи в печать, авторы должны отправить подписанные:

1. Соглашение о передаче авторских прав (<http://www.mpm.spbstu.ru>, раздел «Авторам»);
2. Экспертные заключения о том, что материалы статьи не содержат сведений, составляющих государственную тайну, и информацию, подлежащую экспортному контролю; по адресу: *Россия, 195251, Санкт-Петербург, Политехническая, д. 29, Санкт-Петербургский политехнический университет Петра Великого, Институт передовых производственных технологий, Редакция периодических изданий.*

Скан-копии подписанных документов просим направить по электронной почте: mpmjjournal@spbstu.ru

Тип файла:

Редакция принимает **файлы MS Word с копией в формате PDF**. Статья должна быть подготовлена в соответствии с настоящей инструкцией, мы просим авторов также следовать более подробным инструкциям на сайте журнала <http://www.mpm.spbstu.ru> в разделе «Авторам».

Длина статьи:

Статья не должна превышать 30 страниц формата А4, включая Таблицы и Рисунки, размещенные непосредственно в соответствующих местах.

Общие правила оформления статьи:

НАЗВАНИЕ СТАТЬИ: ВЫРОВНЯТЬ ПО ЦЕНТРУ, ШРИФТ, TIMES NEW ROMAN 14 BOLD, ЗАГЛАВНЫЕ БУКВЫ

Автор(ы): **А.Б. Первыйавтор¹, В.Г. Автор^{2*}**- шрифт Times New Roman 12, bold, по центру

¹Наименование организации, адрес, страна - шрифт Times New Roman 10, по центру

* e-mail автора, представившего статью - шрифт Times New Roman 10, по центру

Аннотация. Аннотация статьи составляет не более 12 строк. Используйте шрифт Times New Roman 12, одинарный межстрочный интервал.

Ключевые слова: укажите ключевые слова после аннотации.

Как организовать текст статьи. Используйте шрифт Times New Roman 12, одинарный межстрочный интервал. При необходимости выделить какую-либо информацию используйте *курсив*. Используйте **полужирный** шрифт только для заголовков и подзаголовков.

Номера страниц. Пожалуйста, не используйте нумерацию страниц

Таблицы, Рисунки, Уравнения. Подробные правила оформления данных элементов статьи приведены в инструкции на сайте журнала <http://www.mpm.spbstu.ru>

Литература

Ссылки приводятся в тексте в квадратных скобках [1,3,5-9]. Стиль оформления ссылок:

- [1] A.K. Mukherjee // *Materials Science and Engineering: A* 322 (2002) 1.
- [2] C.C. Koch, I.A. Ovid'ko, S.Seal, S. Veprek, *Structural Nanocrystalline Materials: Fundamentals and Applications* (Cambridge University Press, Cambridge, 2007).
- [3] A.E. Romanov, V.I. Vladimirov, In: *Dislocations in Solids*, ed. by F.R.N. Nabarro (North Holland, Amsterdam, 1992), Vol. 9, p.191.
- [4] C.K. Takemori, T.D. Müller, M.A. De Oliveira, *Numerical simulation of transient heat transfer during welding process*, In: *International Compressor Engineering Conference* (Purdue, USA 2010).
- [5] W. Pollak, M. Blecha, G. Specht // *US Patent 4572848*.
- [6] <http://www.mpm.spbstu.ru>

МЕХАНИКА И ФИЗИКА МАТЕРИАЛОВ

34 (1) 2017

Учредители: Санкт-Петербургский политехнический университет Петра Великого,

Институт проблем Машиноведения Российской Академии Наук

Издание зарегистрировано федеральной службой по надзору в сфере связи,
информационных технологий и массовых коммуникаций (РОСКОМНАДЗОР),

свидетельство ПИ №ФС77-69287 от 06.04.2017 г.

Редакция журнала

Профессор, д.т.н., академик РАН, А.И. Рудской – главный редактор

Профессор, д.ф.-м.н., член-корр. РАН, Д.А. Индейцев – главный редактор

Профессор, д.ф.-м.н. И.А. Овидько (1961 - 2017) – основатель и почетный редактор

Профессор, д.ф.-м.н. А.Л. Колесникова – ответственный редактор

Доцент, к.т.н. А.С. Немов – ответственный редактор

Е.О. Касяненко – выпускающий редактор

А.И. Хайрутдинова – редактор, корректор

Телефон редакции

+7 (812) 591-65-28

E-mail: mpmjourn@spbstu.ru

Компьютерная верстка А.В. Шимченко

Подписано в печать 29.12.2017 г. Формат 60x84/8. Печать цифровая
Усл. печ. л. 7. Тираж 100. Заказ ____.

Отпечатано с готового оригинал-макета, предоставленного автором
в Издательско-полиграфическом центре Политехнического университета Петра
Великого. 195251, Санкт-Петербург, Политехническая ул., 29.
Тел.: (812) 552-77-17; 550-40-14.

Unified approach to forming fullerenes and nanotubes.....	1-17
Alexander I. Melker and Maria A. Krupina	
Modeling growth of midi-fullerenes from C20 to C60.....	18-28
Alexander I. Melker and Maria A. Krupina	
Modeling growth of midi-fullerenes from C48 to C72.....	29-36
Alexander I. Melker and Maria A. Krupina	
Fullerenes of the $\Delta N=10$ series.....	37-45
Alexander I. Melker, Maria A. Krupina, Ruslan M. Zarafutdinov	
Fullerenes of the $\Delta N=12$ series.....	46-50
Alexander I. Melker, Maria A. Krupina, Ruslan M. Zarafutdinov	
Design and simulation of additive manufactured structures of three-component composite material	51-58
A.Yu. Zobacheva, A.S. Nemov, A.I. Borovkov, A.D. Novokshenov, M.V. Khovaiko, N.A. Ermolenko	
Validation of EuroNCAP frontal impact of frame off-road vehicle: road traffic accident simulation	59-69
S. Alekseev, A. Tarasov, A. Borovkov, M. Aleshin, O. Klyavin	
NVH analysis of offroad vehicle frame. Evaluation of mutual influence of body-frame system components.....	70-75
A. Patrikeev, A. Tarasov, A. Borovkov, M. Aleshin, O. Klyavin	
Integrated system as a tool for implementation of simulation- and optimization-based design methodology	76-81
Aleksei Novokshenov, Alexander Nemov, Dmitriy Mamchits, Aleksandra Zobacheva	
Vehicle dynamics prediction module.....	82-89
J. Leoro, S. Krutitskiy, A. Tarasov, A. Borovkov, M. Aleshin, O. Klyavin	
Applicability of polymer composite materials in the development of tractor falling-object protective structures (FOPS).....	90-96
Dmitrii Lebedev, Alexey Okunev, Mikhail Aleshin, Kirill Ivanov, Oleg Klyavin, Svetlana Nikulina, Oleg Rozhdestvenskiy, Alexey Borovkov	
Variational problem for hydrogenerator thrust bearing	97-102
O.V. Antonova, A.I. Borovkov, Yu.Ya. Boldyrev, I.B. Voynov	